

DESIGN OF A NEW TEST SYSTEM FOR EVALUATION AND
OPTIMIZATION OF OPERATING PARAMETERS AFFECTING PROTON
EXCHANGE MEMBRANE FUEL CELL PERFORMANCE



A THESIS SUBMITTED IN PARTIAL FULFILLMENT OF THE REQUIREMENT FOR
THE DEGREE OF MASTER OF ENGINEERING IN
AUTOMOTIVE AND ADVANCED TRANSPORTATION ENGINEERING
SCHOOL OF ENGINEERING
KING MONGKUT'S INSTITUTE OF TECHNOLOGY LADKRABANG
2024
KMITL-2024-EN-M-277-238

This material is reserved for educational use only, not allowed for commercial use.

Forbidden to modify the content, and cite the document when use.



COPYRIGHT 2024

SCHOOL OF ENGINEERING

KING MONGKUT'S INSTITUTE OF TECHNOLOGY LADKRABANG

This material is reserved for educational use only, not allowed for commercial use.

Forbidden to modify the content, and cite the document when use.

Thesis	Design of A New Test System for Evaluation and Optimization of Operating Parameters Affecting Proton Exchange Membrane Fuel Cell Performance
Student	Mr. Pham Dinh Thao
Student ID.	65016118
Degree	Master of Engineering
Program	Automotive and Advanced Transportation Engineering
Year	2024
Thesis Advisor	Asst. Prof. Dr. Mek Srilomsak
Co-Thesis Advisor	Dr. Visarn Lilavivat
Co-Thesis Advisor	Prof. Dr. Shuichiro Hirai

ABSTRACT

This research explores the influence of operating parameters (operating temperature (OT), relative humidity (RH), cathode operating pressure (COP), and air stoichiometry ratio (ASR)) and droplet purge processes on Proton Exchange Membrane Fuel Cell (PEMFC) performance. The goals are to determine the optimal operating conditions and enhance overall PEMFC power density.

A custom-designed test system was used to investigate the individual and combined effects of two parameters (OT and RH) and four parameters (OT, RH, COP, and ASR) through experimentation. The orthogonal test design method, range analysis, and standard deviation (STDEV) were employed to evaluate the impact of these parameters, identify optimal settings for maximum power density, and assess the stability of purge strategies.

The results demonstrate a proportional increase in cell performance with increasing COP and decreasing RH. Conversely, the impact of OT and ASR displayed a less direct relationship. The analysis confirms the effectiveness of the orthogonal method, revealing optimal conditions for maximum power density at OT 80°C, RH 50%, COP 22 psi, and ASR 2.4.

Furthermore, the proposed purge strategy (0.75 seconds duration and 10 seconds interval) demonstrates the potential to improve PEMFC power density by up

to 23.518%, with a corresponding increase in STDEV of 143.982% compared to the optimal condition achieved using the orthogonal test.

These findings highlight the varying influence of operating parameters based on current density, test objectives, and cell configurations. Additionally, the research emphasizes the trade-off between maximizing cell power density and maintaining stability when optimizing purge processes.

Keywords: PEMFC, Performance, Operating parameters, Orthogonal test, Droplet purge.



ACKNOWLEDGEMENT

My deepest gratitude goes to all who supported me on this incredible research adventure.

Special mention goes to Dr. Visarn Lilavivat, my advisor from the National Science and Technology Development Agency (NSTDA). His guidance, expertise, and unwavering support were instrumental in shaping this research and propelling me forward. I am incredibly fortunate to have had him as my advisor.

I would also like to express my sincere thanks to Asst. Prof. Dr. Mek Srilomsak, my supervisor from King Mongkut's Institute of Technology Ladkrabang (KMITL), and Prof. Dr. Shuichiro Hirai, my co-advisor from the Tokyo Institute of Technology. Their invaluable insights and collaborative spirit significantly enriched this research project.

My sincere appreciation extends to the Renewable Energy and Energy Efficiency Research Laboratory staff and members. Their constant support and collaborative environment fostered a valuable learning experience throughout this research journey.

Finally, I acknowledge the unwavering support and encouragement of my fellow classmates and my family. Their camaraderie and belief in me made this journey all the more fulfilling.

This research could not have been completed without the contributions of all these individuals. Their support, both professional and personal, has been truly invaluable.

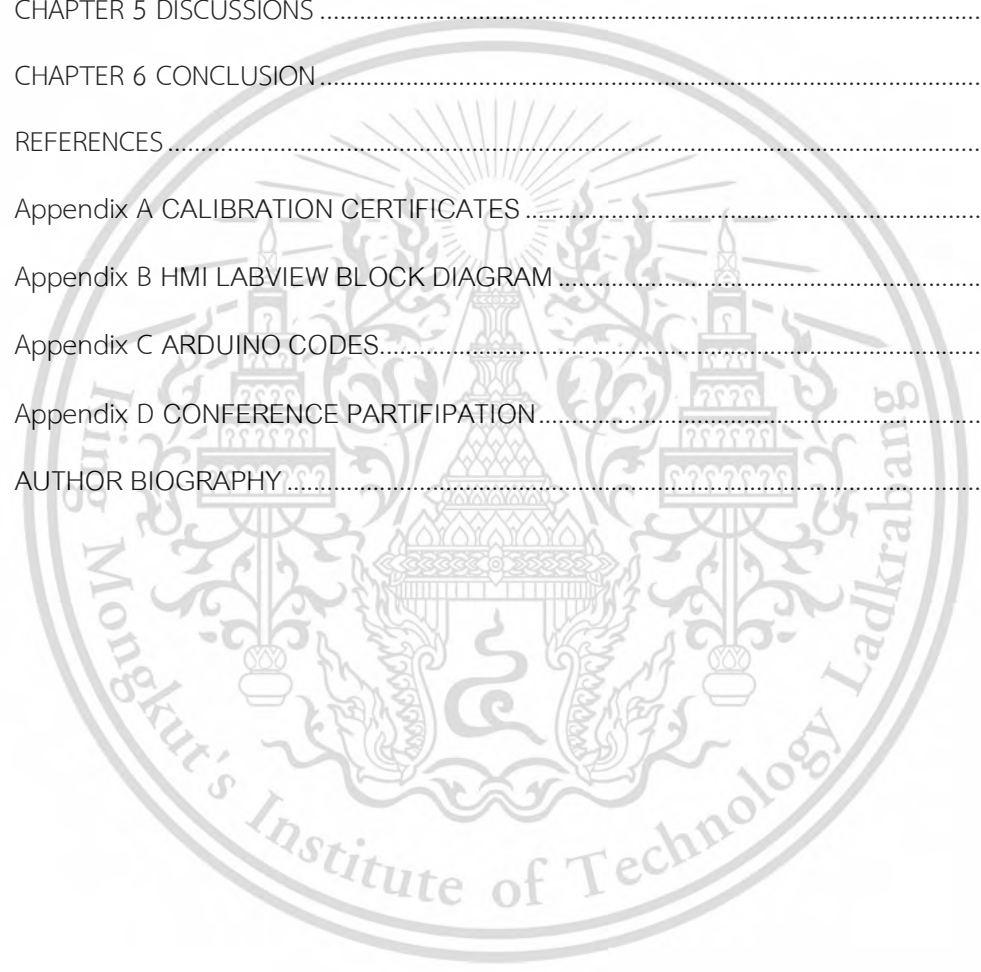
Pham Dinh Thao

TABLE OF CONTENTS

	Page
ABSTRACT IN ENGLISH.....	I
ACKNOWLEDGEMENT	III
TABLE OF CONTENTS	IV
LIST OF TABLES	VII
LIST OF FIGURES	VIII
LIST OF ABBREVIATIONS AND SYMBOLS.....	X
CHAPTER 1 INTRODUCTION	12
1.1 STATEMENT AND SIGNIFICANT OF THE PROBLEMS.....	12
1.2 GOAL AND OBJECTIVE OF THE STUDY.....	17
1.2.1 Goals	17
1.2.2 Objectives	17
1.3 SCOPE OF THE STUDY	17
1.4 PROCESS OF THE STUDY.....	18
1.5 ASSUMPTIONS	18
1.6 THEORETICAL FRAMEWORK.....	19
1.6.1 PEMFC fundamentals	19
1.6.2 PEMFC performance characteristics.....	21
1.6.3 Operating parameters of PEMFC.....	23
1.6.4 Purge process of a flow-through cathode PEMFC	26
CHAPTER 2 LITERATURE REVIEW.....	28
2.1.1 Design of PEMFC test systems.....	28
2.1.2 Influence of operating parameters on PEMFC performance.....	29
2.1.3 Optimization and innovative methods for PEMFC performance enhancement.....	30
CHAPTER 3 RESEARCH METHODOLOGY.....	33
3.1 RESEARCH METHODS.....	33
3.1.1 Systematic Literature Review (SLR).....	33
3.1.2 Experimental investigations.....	35

3.2 OPERATING PARAMETERS SELECTION.....	36
3.3 TOOLS AND TECHNIQUES.....	38
3.3.1 Tools for test system construction.....	38
3.3.2 Techniques	50
3.4 DATA COLLECTION PROCEDURES.....	52
3.4.1 Activation	52
3.4.2 Defining lower limits of the air flow rate and ASR.....	55
3.4.3 Setup procedure.....	56
3.4.4 Data collection at steady state	56
3.4.5 Purge process between load levels of each test case.....	56
3.5 DATA ANALYSIS METHODS.....	56
3.5.1 Range analysis.....	56
3.5.2 Standard deviation.....	57
CHAPTER 4 RESULTS	58
4.1 SELF-DESIGNED TEST SYSTEM	58
4.1.1 Configuration and operation.....	58
4.1.2 Human Machine Interface	60
4.1.3 Operating range and accuracy.....	61
4.2 TWO-PARAMETER TEST RESULTS	62
4.2.1 Effect of OT at RH 50%.....	62
4.2.2 Effect of OT at RH 60%.....	63
4.2.3 Effect of OT at RH 70%.....	65
4.2.4 Effect of RH at OT 60°C.....	66
4.2.5 Effect of RH at OT 70°C.....	67
4.2.6 Effect of RH at OT 80°C.....	68
4.2.7 Polarization and power density curves.....	69
4.2.8 Range analysis.....	71
4.3 FOUR-PARAMETER TEST RESULTS.....	72
4.3.1 Polarization curves.....	73
4.3.2 Power density curves	75
4.3.3 Influence Degree	77
4.3.4 Effect of OT	78

4.3.5 Effect of RH.....	80
4.3.6 Effect of COP at the cathode side.....	81
4.3.7 Effect of ASR.....	83
4.4 DROPLET PURGE	84
4.4.1 Normal operation	84
4.4.2 Various purge strategies	87
4.4.3 Effect of purge strategies on PEMFC power density	95
CHAPTER 5 DISCUSSIONS	97
CHAPTER 6 CONCLUSION.....	104
REFERENCES.....	106
Appendix A CALIBRATION CERTIFICATES	113
Appendix B HMI LABVIEW BLOCK DIAGRAM	115
Appendix C ARDUINO CODES.....	116
Appendix D CONFERENCE PARTIFIPATION.....	119
AUTHOR BIOGRAPHY.....	120



LIST OF TABLES

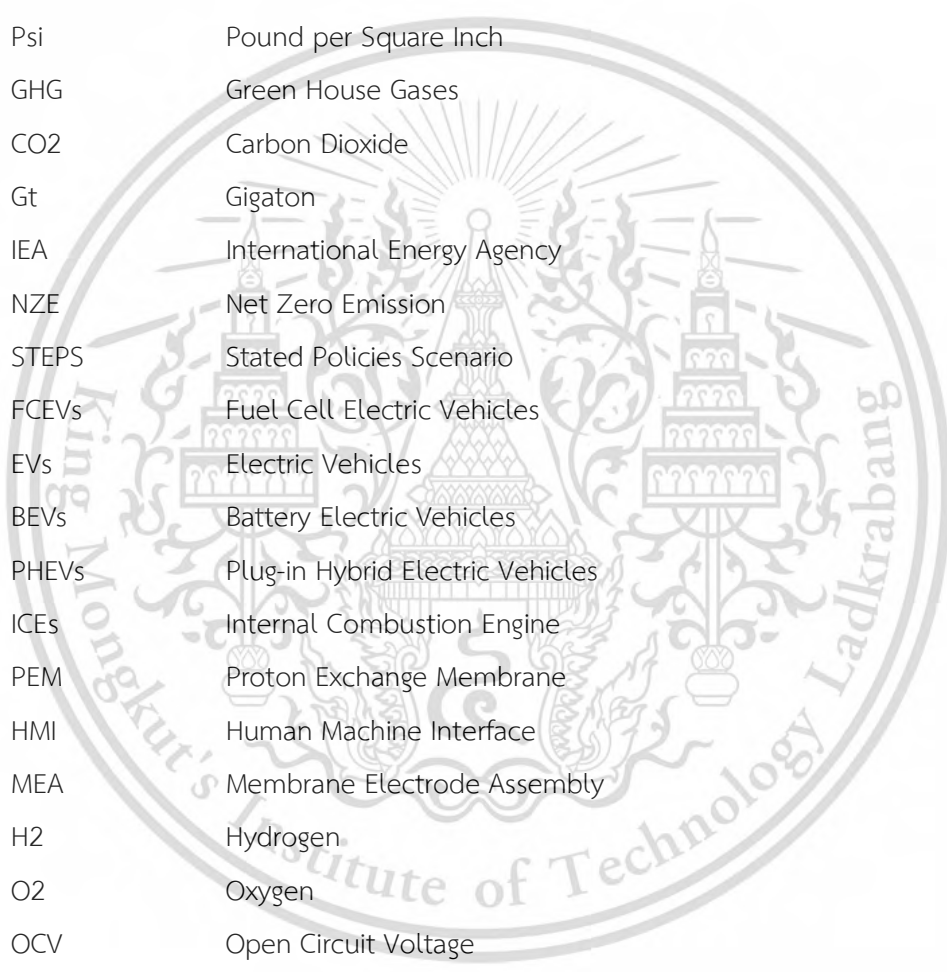
Table	Page
Table 3.1 Refining process of SLR.....	34
Table 3.2 Operating conditions of PEMFC in previous studies.....	36
Table 3.3 Four operating parameter values.....	38
Table 3.4 Specifications of the two MEAs.....	39
Table 3.5 Specifications of the Economy Series temperature controller [54].....	41
Table 3.6 Specifications of mass-flow controller [56].....	43
Table 3.7 Specifications of needle valve [57].....	45
Table 3.8 Specifications of pressor sensor [58].....	46
Table 3.9 Specifications of solenoid valve [59].....	47
Table 3.10 Specifications of electronic load [60].....	48
Table 3.11 Pressure range of pressure sensor.....	50
Table 4.1 Specifications of the self-designed PEMFC test system.....	61
Table 4.2 Nine test cases of two-parameters test.....	62
Table 4.3 Peaks and troughs of OT and RH influence degrees.....	72
Table 4.4 Nine test cases of four-parameter test.....	73
Table 4.5 Groups of orthogonal test results.....	75
Table 4.6 Minimum and maximum influence degrees of four operating parameters.....	78
Table 4.7 Droplets purge strategies.....	85
Table 4.8 Current and voltage characteristics under 10s purge interval operation.....	89
Table 4.9 Current and voltage characteristics under 20s purge interval operation.....	91
Table 4.10 Current and voltage characteristics under 30s purge interval operation.....	93
Table 4.11 Comparisons of purge strategies and the optimal condition from orthogonal tests (0.15939 W/cm ² , STDEV = 0.01380 W/cm ²).....	96

LIST OF FIGURES

Figure	Page
Figure 1.1 Global CO ₂ emissions 1970-2022 [1].....	12
Figure 1.2 The estimated share of CO ₂ emissions in the transportation sector worldwide in 2022 [4]	13
Figure 1.3 Emissions reductions and key milestones in transport in the NZE.....	14
Figure 1.4 Global share of electric vehicle sales by type and scenario,.....	15
Figure 1.5 (a) Main components of a PEMFC and (b) Typical MEA schematic [17].....	20
Figure 1.6 Typical polarization curve of PEMFC. [22] V* is caused by hydrogen crossover.	22
Figure 1.7 Describe the purge period	27
Figure 2.1 Liquid water dynamics in the gas channel in the base case: (a) 0.081 mL and (b) 0.243 mL in Stage 1 (interval), (c) 2.5 ms, (d) 5.0 ms, (e) 10.0 ms, (f) 15.0 ms, (g) 20.0 ms and (h) 25.0 ms in Stage 2 (purge) [37]	31
Figure 3.1 Steps of the SLR method [43].....	33
Figure 3.2 PEMFC components	39
Figure 3.3 Temperature control unit a) temperature controller from MiSUMi Economy, b) thermal couple type T, c) SSR, and d) heater.....	40
Figure 3.4 Humidification bottle from Fuel Cell Technologies. Inc.....	42
Figure 3.5 Outlet dew point over increasing gas flowrate [55]	42
Figure 3.6 Digital mass-flow controller from Aalborg® Instruments & Controls	43
Figure 3.7 Integral Bonnet Needle Valve NV Series from Hy-Lok Corporation	44
Figure 3.8 Compact Pressure Sensor from SMC Corporation	45
Figure 3.9 Solenoid Valve 4V200 Series from AirTAC.....	47
Figure 3.10 High Power DC Electronic Load from ITECH Electronics	48
Figure 3.11 Arduino Uno R3 board.....	49
Figure 3.12 Pressure sensor calibration data from SMC	50
Figure 3.13 Pressure sensor calibration setup	51
Figure 3.14 System calibration graph of the pressure sensor	51
Figure 3.15 Activation process	54
Figure 3.16 Initial PEMFC performance.....	54
Figure 4.1 Test system photograph	58

Figure 4.2 Test system schematic	59
Figure 4.3 LabVIEW HMI of the test system	60
Figure 4.4 Effect of OT at RH 50%.....	63
Figure 4.5 Effect of OT at RH 60%.....	64
Figure 4.6 Effect of OT at RH 70%.....	65
Figure 4.7 Effect of RH at OT 60°C	66
Figure 4.8 Effect of RH at OT 70°C	67
Figure 4.9 Effect of RH at OT 80°C	68
Figure 4.10 Polarization curves of two parameters test.....	69
Figure 4.11 Power density curves of two parameters test.....	70
Figure 4.12 Influence Degree of OT and RH.....	71
Figure 4.13 Polarization curves of four parameters test.....	74
Figure 4.14 Power density curves of four parameters test.....	76
Figure 4.15 Influence degree of four parameters	77
Figure 4.16 Effect of OT at RH 50%, OP 22psi, and ASR 2.4.....	79
Figure 4.17 Effect of RH at OT 80°C, COP 22psi, and ASR 2.4.....	80
Figure 4.18 Effect of COP at OT 80°C, RH 50%, and ASR 2.4.....	82
Figure 4.19 Effect of ASR at OT 80°C, RH 50%, and COP 22psi	83
Figure 4.20 The natural droplets pushing frequency of the PEM fuel cell	85
Figure 4.21 Diagram of flooding diagnosis under normal operation	86
Figure 4.22 Diagram of PEMFC outputs diagnosis under purge operation of purge interval 10s and purge duration 0.75s.....	87
Figure 4.23 Various purge durations at purge interval 10s.....	88
Figure 4.24 Various purge durations at purge interval 20s.....	90
Figure 4.25 Various purge durations at purge interval 30s.....	93
Figure 4.26 Power density and stability of various purge strategies	95

LIST OF ABBREVIATIONS AND SYMBOLS



OT	Operating Temperature
RH	Relative Humidity
COP	Cathode Operating Pressure
ASR	Air Stoichiometry Ratio
PEMFC	Proton Exchange Membrane Fuel Cell
STDEV	Standard Deviation
Psi	Pound per Square Inch
GHG	Green House Gases
CO ₂	Carbon Dioxide
Gt	Gigaton
IEA	International Energy Agency
NZE	Net Zero Emission
STEPS	Stated Policies Scenario
FCEVs	Fuel Cell Electric Vehicles
EVs	Electric Vehicles
BEVs	Battery Electric Vehicles
PHEVs	Plug-in Hybrid Electric Vehicles
ICEs	Internal Combustion Engine
PEM	Proton Exchange Membrane
HMI	Human Machine Interface
MEA	Membrane Electrode Assembly
H ₂	Hydrogen
O ₂	Oxygen
OCV	Open Circuit Voltage
Pt/C	Platinum on carbon
OP	Operating Pressure
PLC	Programmable Logic Control
PID	Proportional Integral Derivative
DOE	Design of Experiment
SLR	Systematic Literature Review
OTD	Orthogonal Test Design

HSR	Hydrogen Stoichiometry Ratio
GDL	Gas Diffusion Layer
SSR	Solid State Relay
MFC	Mass Flow Controller
Sccm	standard centimeter cubic per minute
Slm	standard liter per minute
USB	Universal serial bus
VISA	Virtual Instrumen
CC	Constant Current
DI water	Deionized water



CHAPTER 1

INTRODUCTION

1.1 STATEMENT AND SIGNIFICANT OF THE PROBLEMS

Our world faces a pressing challenge which is curbing greenhouse gas (GHG) emissions to combat climate change and global warming which is seriously affecting human life. Since the COVID-19 pandemic caused a temporary dip in emissions, levels have since rebounded as the mobility demand recovered from the pandemic [1, 2], demonstrated in **Figure 1.1**.

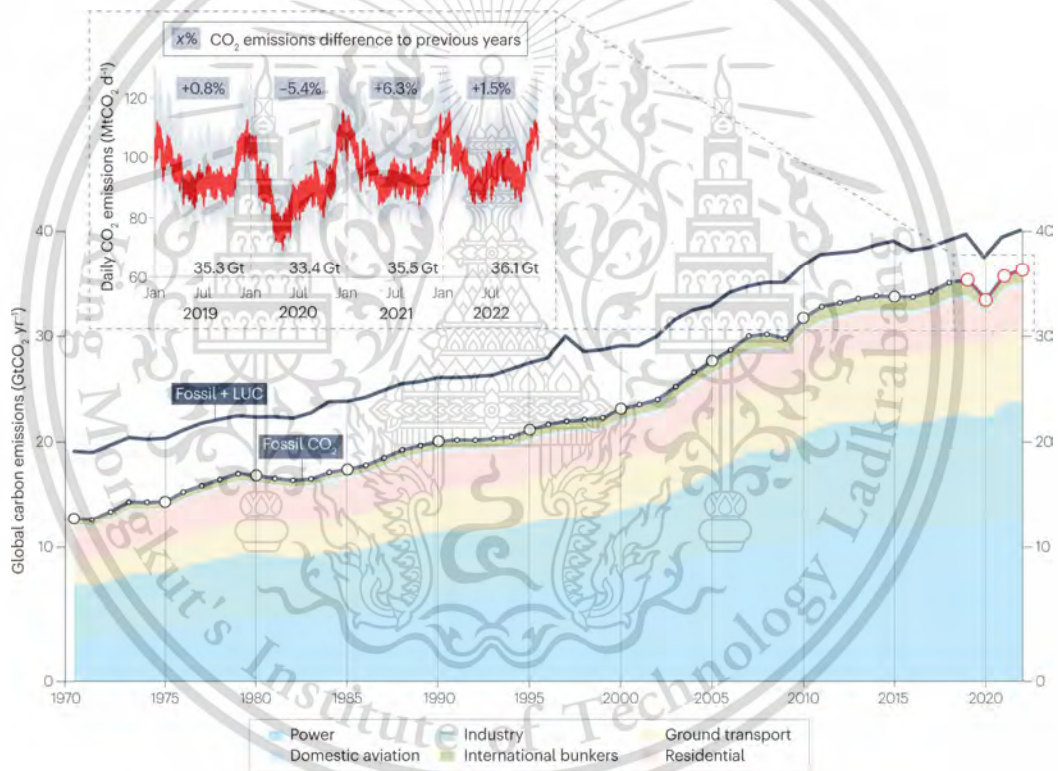


Figure 1.1 Global CO₂ emissions 1970-2022 [1]

There was a concerning rise in global CO₂ emissions in 2022, with a 1.5% increase compared to 2021. This follows previous growth trends, with emissions up 7.9% and 2.0% relative to 2020 and 2019 respectively. Total CO₂ emissions in 2022 reached 36.1 Gt CO₂ [1]. While there was a slight slowdown in emissions in 2023, with only a 0.1% increase compared to 2022, emissions still reached 35.8 Gt CO₂. Even with this slower growth, the remaining carbon budget for staying below 1.5°C warming is

still being eroded at an alarming rate [3]. The ground transportation sector is a major source of greenhouse gas emissions, responsible for 17.9% of the global total in 2022 [1]. In which, cars and vans are the primary culprits within this sector, generating almost half (48%) of global transport-related carbon dioxide emissions in 2022 based on an analysis by Statista using International Energy Agency (IEA) data [4], as illustrated in **Figure 1.2**.

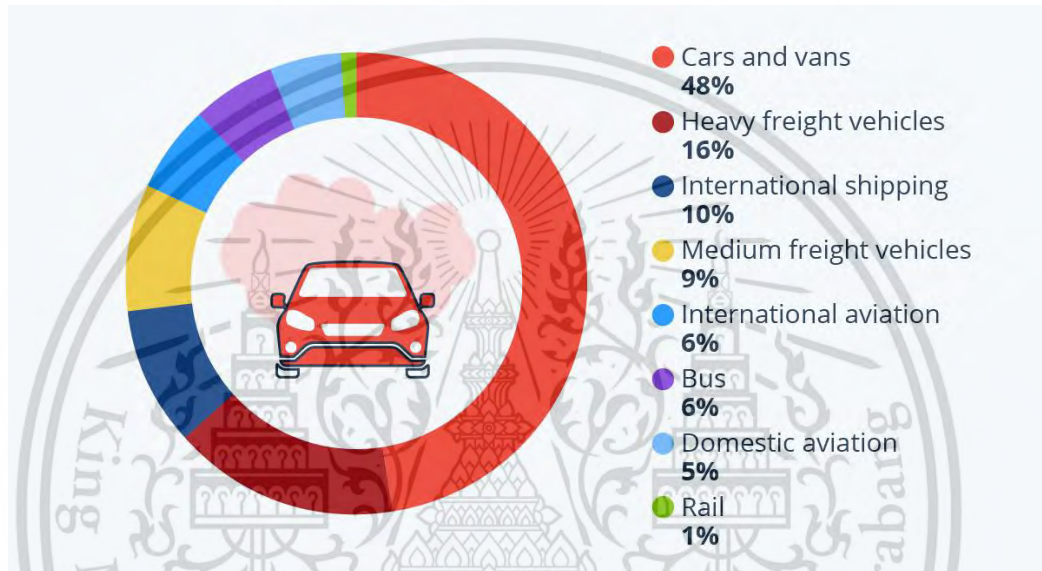


Figure 1.2 The estimated share of CO₂ emissions in the transportation sector worldwide in 2022 [4]

The urgency of addressing transportation emissions is underscored by international agreements like the Paris Agreement (2015). This landmark treaty, adopted by nearly all nations (196), aims to limit global warming to 1.5°C [5]. Achieving this ambitious target requires significant reductions in transport emissions, particularly in a net-zero emissions (NZE) scenario compared to a business-as-usual approach (stated policies scenario, STEPS). The World Energy Outlook 2022 proposes a pathway for decarbonizing the transport sector, as depicted in **Figure 1.3**. This NZE scenario hinges on two key strategies: (1) Electrification of transportation with a significant shift towards electric vehicles (EVs) and hydrogen fuel cell electric vehicles (FCEVs) in road transport, and (2) Using low-emission fuels as increased use of biofuels, hydrogen, and hydrogen-derived fuels, particularly for aviation and shipping, either blended with conventional fuels or directly [2].

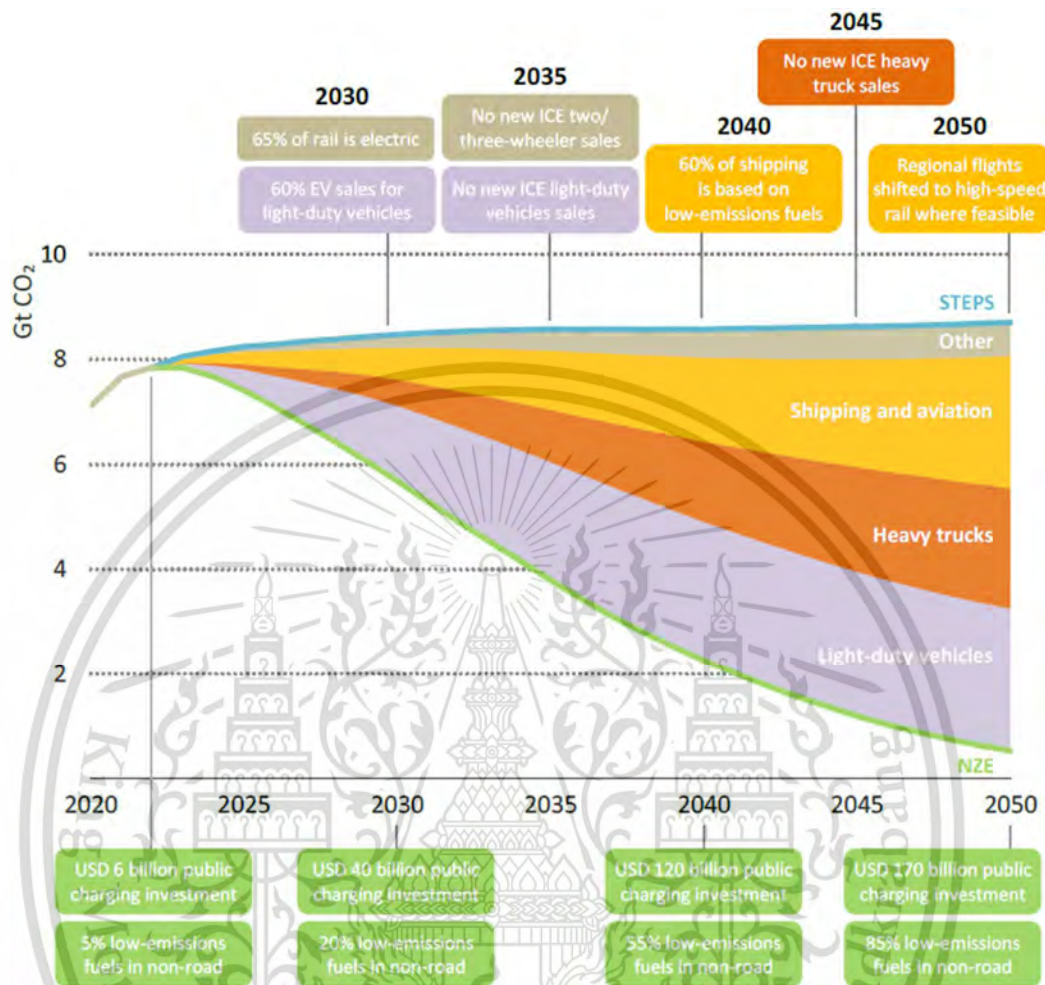


Figure 1.3 Emissions reductions and key milestones in transport in the NZE Scenario relative to the STEPS, 2020-2050 [2]

The development and widespread adoption of low-emission vehicles, particularly electric vehicles (EVs), are crucial elements in the decarbonization strategy. Many automakers are reflecting this urgency by setting ambitious goals, such as carbon neutrality by 2030 [6]. Electrification of road transport and rail offers a powerful solution for achieving rapid and significant reductions in emissions. This trend is evident in the surging sales of EVs and the global market share has more than tripled in just two years, reaching 14% in 2023. Projections indicate further record sales this year.

The World Energy Outlook 2022 underscores the potential of electrification in its NZE Scenario shown in **Figure 1.4**. This scenario envisions electric cars accounting for a dominant two-thirds of total vehicle sales by 2030.

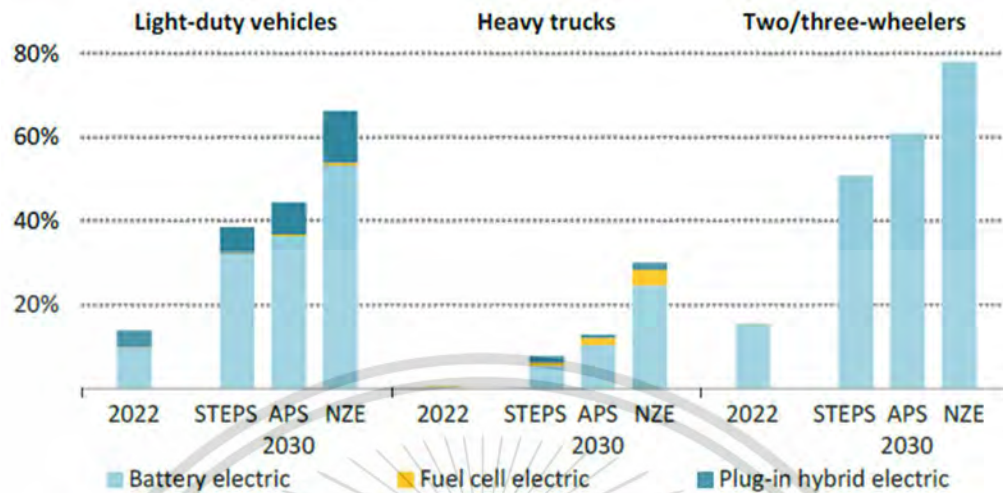


Figure 1.4 Global share of electric vehicle sales by type and scenario, 2022 and 2030 [7]

Among electric vehicles, FCEVs offer distinct advantages for specific applications. Compared to Battery Electric Vehicles (BEVs) or Plug-in Hybrid Electric Vehicles (PHEVs), FCEVs boast longer driving range, faster refueling times, and improved performance in cold weather conditions [8-10]. This makes them particularly attractive for heavy-duty transport, as illustrated by the rising share of FCEVs in this sector, illustrated in **Figure 1.4**. The core technology behind FCEVs is the PEMFCs. PEMFCs are favored for their versatility in power output, high energy conversion efficiency, and user-friendly operation [8, 10, 11]. They also offer a significant efficiency advantage over traditional Internal Combustion Engines (ICEs). PEMFCs typically achieve efficiencies between 40-50%, compared to the 20-35% range of ICEs [12].

The environmental benefits of FCEVs are particularly compelling when fueled by green hydrogen, produced through renewable energy sources like electrolysis, with zero greenhouse gas emissions. Furthermore, FCEVs operation themselves produces no tailpipe emissions [13]. This combination makes them a promising solution for achieving a sustainable transportation future.

Despite their advantages, the implementation of FCEVs faces significant challenges. These include the high cost of hydrogen fuel, limitations in PEMFC technology development, and a lack of widespread refueling infrastructure [13]. Research efforts are underway to address these challenges, such as exploring cost-

effective hydrogen production through renewable energy-powered electrolysis [14-16]. However, compared to BEVs and PHEVs, FCEVs have received less investment from automakers. Currently, only a few brands like Toyota and Hyundai offer commercial FCEVs.

Recognizing both the potential and the hurdles associated with FCEVs, research on PEMFC technology plays a crucial role. This research can contribute to:

- Promoting the use of FCEVs by demonstrating their real-world benefits.
- Strengthening the theoretical framework of PEMFC technology.
- Improving PEMFC performance to make them more competitive with other EVs.

This research focuses on experimental evaluation and optimization of operating parameters and droplet purge at the cathode side to enhance PEMFC performance, the core technology of FCEVs. By systematically investigating the effects of operating parameters and purge process to define the optimal working condition of PEMFC, we aim to enhance the competitiveness of FCEVs and accelerate their adoption as a sustainable transportation solution. Understanding and optimizing PEMFC performance through the analysis of operational parameters will ultimately contribute to a cleaner and greener world.

This thesis is structured as follows:

Chapter 2: Provides a comprehensive review of existing literature on PEMFC technology and their roles in improving PEMFC performance.

Chapter 3: Details the research methodology employed in this study, including the experimental design, data acquisition procedures, and analytical techniques used to evaluate PEMFC performance.

Chapter 4: Presents the findings of the research, analyzing the impact of operational parameters on PEMFC performance and discussing the implications for optimizing PEMFC power density.

Chapter 5: Discusses the broader significance of the research findings, their contribution to the advancement of PEMFC technology, and the potential impact on promoting FCEV adoption for sustainable transportation.

Chapter 6: Offers concluding remarks, summarizing the key takeaways of the research, and outlining potential avenues for future investigation.

1.2 GOAL AND OBJECTIVE OF THE STUDY

1.2.1 Goals

Based on the problems addressed in the introduction section, four main goals were set as follows.

- To investigate the effects of four operating parameters and their influence degree on PEMFC performance over current density ranges.
- To optimize operating conditions of the single 25cm² PEM fuel cell.
- To examine the effects of droplet purge strategies at the cathode side on PEMFC performance.
- To improve PEMFC's power density by 20% at its extended peak.

1.2.2 Objectives

Step-by-step objectives were listed below to achieve the goals of this research.

- Constructing a test system for two parameters (OT and RH) testing.
- Conducting two parameter experiments and data analysis.
- Upgrading test system for four parameters (OT, RH, COP, and ASR) testing.
- Designing a human-machine interface (HMI) for purge valve controlling and data acquisition.
- Selecting and designing test conditions based Orthogonal method.
- Conducting four parameter experiments and data analysis to find the optimal working condition for PEMFC.
- Proposing droplet purge strategies based on the optimal condition.
- Conducting droplet purge experiments and data analysis to find out the optimal purging strategy.

1.3 SCOPE OF THE STUDY

This research was structured into three main parts:

First, designing a new test system for a small single PEM fuel cell (active area is 25 cm²) which could be used to evaluate the effect and impact of four parameters (OT, RH, COP, and ASR) on PEMFC performance.

Second, experimentally evaluate the effect of operating parameters on PEMFC performance based on individual tests, orthogonal test design, and range analysis.

Finally, optimizing the cathode droplet purge strategy for the best power density and stability of PEMFC.

1.4 PROCESS OF THE STUDY

The research process commenced with a comprehensive literature review to ascertain existing theories and pinpoint research gaps. Subsequently, the study focused on investigating the impact of operating temperature and relative humidity on PEMFC performance as a primary step. The experimental setup was initially configured to accommodate the testing of two parameters. Analysis of the two-parameter test results yielded significant insights.

Building upon these findings, the experimental setup was enhanced to facilitate four-parameter tests, specifically addressing the back pressure control system and cathode outlet purging valve. Employing an orthogonal test design coupled with range analysis, the study explored the effects of these parameters comprehensively. Optimal conditions were identified and subsequently applied to devise droplet purging strategies.

Evaluation of the purging results ensued, leading to the formulation of additional findings. Finally, a thorough discussion encompassing all results was conducted, culminating in the formulation of conclusions and recommendations for future research endeavors.

1.5 ASSUMPTIONS

To streamline the research and calculations, several simplifying assumptions are made regarding temperature and water vapor content within the system:

- The temperature of the working gas is assumed to be identical to the cell temperature. This simplifies calculations by eliminating the need to model heat transfer between the gas and the cell walls.
- Nafion tubes with a 1-meter length are assumed to fully equilibrate the gas temperature with the humidifier temperature, which is set at the dew point. This assumption eliminates the need to model complex heat and mass transfer processes within the humidifier.
- Condensation within the inlet manifold is considered negligible due to the effectiveness of pre-heaters.

- The partial pressure of water vapor introduced by the humidifier is assumed to be small and has a negligible impact on the overall system performance.

These assumptions facilitate the construction of a more manageable test system and streamline the analysis of results, while still maintaining a reasonable level of accuracy for the purposes of this study.

1.6 THEORETICAL FRAMEWORK

1.6.1 PEMFC fundamentals

A PEM fuel cell consists of three key components: a fuel electrode (anode), an oxidant electrode (cathode), and an electrolyte placed between them, as depicted in **Figure 1.5**. These electrodes are made of a porous material coated with a catalyst layer, typically platinum in PEMFCs. **Figure 1.5 (b)** demonstrates the fundamental processes occurring in a standard PEMFC operation. Molecular hydrogen (H_2) from a gas-flow stream is introduced to the anode, where it undergoes electrochemical reaction. Here, hydrogen is oxidized, leading to the generation of hydrogen ions and electrons (as per **Equation 1.1**). Subsequently, hydrogen ions migrate through the acidic electrolyte while electrons flow through an external circuit to reach the cathode. At the cathode, electrons and hydrogen ions combine with oxygen from an external gas-flow stream, forming water (as expressed in **Equation 1.2**). The overall reaction within the fuel cell results in the production of water, heat, and electrical work, as indicated by **Equation 1.3**. Effective electric power generation necessitates continuous removal of heat and water by-products to maintain consistent isothermal operation. Consequently, water and thermal management are crucial aspects in the efficient design and functioning of fuel cells [11].

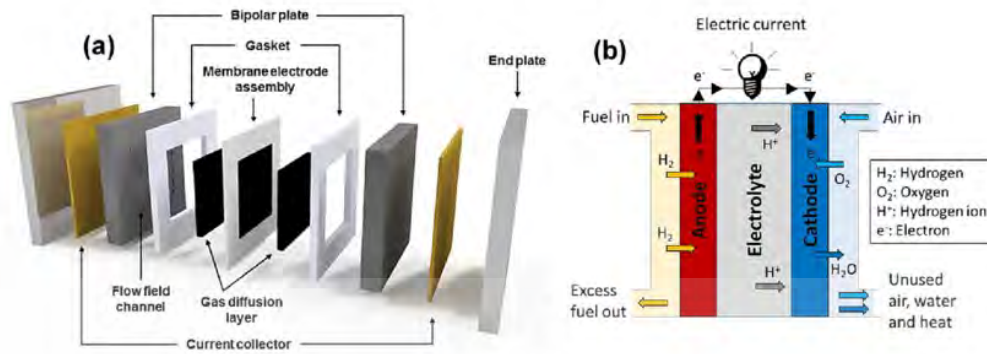
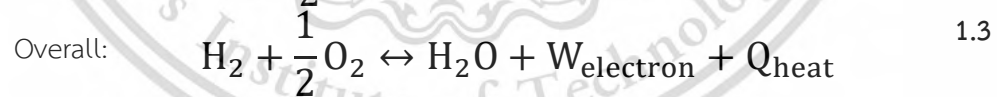
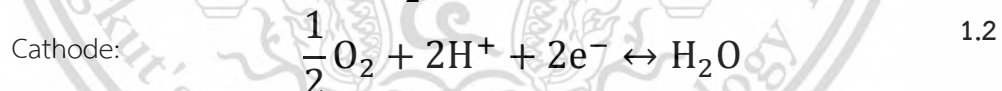


Figure 1.5 (a) Main components of a PEMFC and (b) Typical MEA schematic [17]

In **Figure 1.5 (a)**, a PEMFC is comprised of several essential components, including bipolar plates, diffusion layers, electrodes (both anode and cathode), and an electrolyte. At the heart of a PEMFC lies the membrane electrode assembly (MEA), which consists of a proton exchange membrane (PEM) positioned between two electrodes.

PEMFCs function by converting the chemical energy stored in hydrogen fuel into electrical energy through electrochemical reactions between hydrogen (H₂) and oxygen (O₂). These core reactions are represented by **Equations 1.1, 1.2, and 1.3**.



The two-directional arrows in the equations signify that these reactions, while not thermodynamically reversible due to limited reaction rates in both directions, can proceed in either direction under specific conditions. Assuming equilibrium is reached, the thermodynamic electrode potentials for the half-cell reactions **Equation 1.1 and 1.2** and the overall reaction **Equation 1.3** can be determined using the Nernst equations follows [18, 19].

$$V_{\text{cell}}^{\text{OCV}} = E_{\text{O}_2/\text{H}_2\text{O}}^r - E_{\text{H}_2/\text{H}^+}^r \quad 1.4$$

$$V_{\text{cell}}^{\text{OCV}} = E_{\text{O}_2/\text{H}_2\text{O}}^0 - E_{\text{H}_2/\text{H}^+}^0 + 2.303 \frac{RT}{2F} \log \left(\frac{a_{\text{H}_2} a_{\text{O}_2}^{\frac{1}{2}}}{a_{\text{H}_2\text{O}}} \right) \quad 1.5$$

With a standard potential difference $\left(E_{\text{O}_2/\text{H}_2\text{O}}^0 - E_{\text{H}_2/\text{H}^+}^0 \right)$ of 1.229 V.

Equation 1.5 allows for the theoretical cell voltage to be calculated under various conditions, provided the temperature T , and the activities of oxygen a_{O_2} , hydrogen a_{H_2} , and water $a_{\text{H}_2\text{O}}$ are known. As an approximation, for estimating theoretical electrode potentials and cell voltage, the activity values in **Equation 1.5** a_{O_2} , a_{H_2} , and $a_{\text{H}_2\text{O}}$ can be substituted with their corresponding partial pressures P_{O_2} , P_{H_2} , and $P_{\text{H}_2\text{O}}$ [18, 19].

The theoretical cell voltage often referred to as the open circuit voltage (OCV), represents the ideal voltage output of the fuel cell. However, practical measurements of OCV typically fall below the theoretical value predicted by Equation 1.5. This discrepancy arises from various factors influencing the OCV, including the mixed potential of Pt/PtO catalysts and hydrogen crossover, as illustrated in **Figure 1.6**.

1.6.2 PEMFC performance characteristics

Performance metrics encompass polarization, power density, and system efficiency graphs, which are used to evaluate the fuel cell system. It is achievable to refine the stack design by confining design variables within ranges corresponding to peak power density and/or system efficiency zones. Moreover, the power density curve offers insight into the stack's ability to generate varying output power levels. Typically, the polarization curve, when combined with the power density curve, aids in identifying optimal operational points concerning voltage, current, and power [9].

1.6.2.1 Polarization curve

One of the key performance measures of a fuel cell is the voltage output as a function of electrical current density drawn, or the polarization curve depicted in **Figure 1.6** [20]. Generally, three primary polarization losses can be distinguished: (a)

activation overpotentials, stemming from charge transfer and other reaction kinetics; (b) ohmic losses, originating from the electrical resistances of cell materials and interfaces; and (c) mass transport overpotentials, arising from limitations in mass transport. At low current densities, activation polarization predominantly shapes the curve, characterized by its logarithmic form. This polarization is crucial if the reaction rate on the electrode surface is hindered by sluggish electrode kinetics. Similar to a chemical reaction, electrochemical reactions encounter an activation barrier, typically influenced by the electrode material (electrocatalyst). When pure hydrogen is the fuel, anode activation losses are negligible due to the significantly higher rate of the hydrogen oxidation reaction compared to the cathode reaction. Therefore, the primary source of activation overpotential is the cathode, specifically the oxygen reduction reaction. As current density rises, the curve approximates linearity, reflecting the impact of ohmic losses. This is attributed to resistance from ion migration within the electrolyte and electron flow. Ohmic losses can be expressed as the product of cell current (I) and overall cell resistance (R), which includes electronic, ionic, and contact resistances. With further increases in current density, the curve begins to decline due to mass transport overpotentials, resulting from limitations in reactant availability at catalyst surfaces. Once again, the cathode side is the main source of losses due to the lower diffusivity of oxygen compared to hydrogen, attributed to the larger molecular size of oxygen [21].

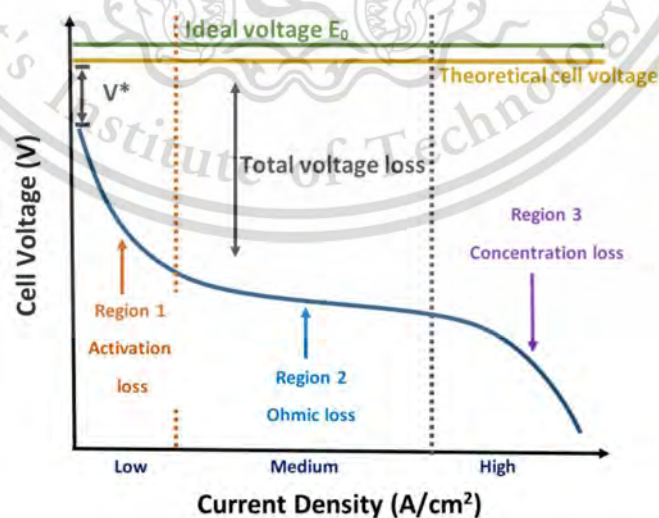


Figure 1.6 Typical polarization curve of PEMFC. [22] V^* is caused by hydrogen crossover.

1.6.2.2 Power density

Power density is the result of multiplying voltage and current density, reaching a maximum value at intermediate voltages (or current densities), as illustrated in the figure. Conversely, efficiency declines as overpotential increases, with its highest point observed at low current densities [22].

1.6.3 Operating parameters of PEMFC

1.6.3.1 Operating temperature

Temperature stands as a pivotal factor in operational considerations that directly affect the PEMFC performance as addressed in **Equation 1.5**. Typically, traditional PEM fuel cells operate within temperatures below 90°C. This practice stems from the fact that the proton conductivity of the Nafion membrane, commonly used in these cells, heavily relies on the membrane's moisture content. Once temperatures exceed 90°C, the membrane tends to dehydrate, resulting in diminished proton conductivity and consequently, a decline in fuel cell performance [23].

1.6.3.2 Relative humidity

The relative humidity (RH) serves as a critical parameter in the operation of a PEM fuel cell due to its direct influence on the proton conductivity of Nafion. This conductivity is directly linked to the moisture content of the membrane. Throughout the operation of the fuel cell, the reactant gases, hydrogen, and air traverse their designated humidifiers to augment their respective relative humidities before being supplied to the fuel cell. Typically, augmenting the RH level can enhance fuel cell efficiency. Nonetheless, this increase in RH may also lead to challenges in water management within the fuel cell, culminating in a phenomenon known as electrode "flooding" [23].

RH is a critical parameter in PEMFC operation. It represents the amount of water vapor present in the air compared to the maximum amount the air can hold at a specific temperature, typically expressed as a percentage. The RH at temperature T is defined as the ratio of the partial pressure and the saturated vapor pressure of water, and can be expressed as in **Equation 1.6** [18, 24].

$$RH = \frac{P_{H_2O}(T_{dp})}{P_{H_2O}^0(T_{ambient})} \times 100 \quad 1.6$$

Here, P_{H_2O} is the partial pressure of water at the temperature T_{dp} and $P_{H_2O}^0$ is the saturated vapor pressure above water at temperature $T_{ambient}$.

Determining the saturated vapor pressure can be achieved using the Arden Buck equations, a set of empirical correlations optimized for accuracy within the 0-100°C temperature range. These equations, based on modifications proposed by Buck (1996) to his earlier work (Buck, 1981), allow for the calculation of dew point temperature through Equations 1.7 and 1.8 [25, 26].

$$T_{dp} = \frac{c \times \ln \left[\frac{RH}{100} \times \frac{P_{s,m}(T)}{a} \right]}{b - \ln \left[\frac{RH}{100} \times \frac{P_{s,m}(T)}{a} \right]} \quad 1.7$$

$$T_{dp} = \frac{c \times \ln \left[\frac{RH}{100} \times e^{\left(\frac{b-T}{d} \right) \left(\frac{T}{c+T} \right)} \right]}{b - \ln \left[\frac{RH}{100} \times e^{\left(\frac{b-T}{d} \right) \left(\frac{T}{c+T} \right)} \right]} \quad 1.8$$

Where

$$a = 6.1121 \text{ (mBar)}$$

$$b = 18.564$$

$$c = 255.57 \text{ (°C)}$$

$$d = 254.4 \text{ (°C)}$$

1.6.3.3 Operating pressure

Another crucial operational parameter is pressure. PEM fuel cells exhibit versatility in operating pressures, spanning from ambient conditions up to 5 atmospheres. Typically, these fuel cells operate within the range of 1 to 3 atm (approx. 73.47 psi) [23]. Elevating the operational pressure has been shown to positively impact electrode kinetics and enhance mass transport processes, ultimately leading to improved fuel cell performance. Additionally, higher operating pressures tend to elevate the fuel cell's OCV. Nonetheless, it's important to note that heightened

pressures necessitate increased power to deliver reactant gases to the fuel cell, consequently leading to greater parasitic power losses [27].

PEMFCs experience a non-uniform distribution of reactant gases across the flow field, leading to a pressure (or concentration) gradient from inlet to outlet. This gradient manifests as a pressure drop (ΔP) across the flow field. Consequently, the inlet pressure (P_{inlet}) and outlet pressure ($P_{\text{back pressure}}$) within a PEMFC differ, with their relationship expressed by **Equation 1.9**. For accurate characterization of the operating pressure due to the pressure gradient, the average fuel cell pressure (OP) is a more convenient metric, expressed as in **Equation 1.10** [18].

$$\Delta P = P_{\text{inlet}} - P_{\text{back pressure}} \quad 1.9$$

$$OP = \frac{P_{\text{inlet}} + P_{\text{back pressure}}}{2} \quad 1.10$$

As established in Equation 1.5, both anode and cathode partial pressures directly impact PEMFC performance. However, increasing hydrogen partial pressure can lead to voltage losses due to crossover, where hydrogen diffuses directly from the anode to the cathode [11, 28]. To eliminate this variable during parameter evaluation, this research focuses solely on the operating pressure at the cathode side (COP).

1.6.3.4 Air stoichiometry ratio

Regulating gas flow rates and stoichiometric ratios are essential for optimal PEMFC performance. Precise control ensures a sufficient supply of both fuel (hydrogen) and oxidant (air) to the reaction sites, preventing starvation and potential catalyst layer degradation. Additionally, adjustments to these parameters allow for easier modulation of the anode and cathode stoichiometric ratios (ASR and HSR), which can influence factors like cell voltage and efficiency [18].

Faraday's Law provides a mathematical framework (**Equations 1.11 to 1.13**) [19] to determine the theoretical quantities of hydrogen (H_2) and oxygen (O_2) required for an H_2 /air PEMFC operating at a specific current density (I_{cell}). It's important to remember that 1 ampere (A) signifies the flow of 1 coulomb (C) of electric charge past a point per second. The calculation of ASR involves multiplying its value by the required air flow rate, which can then be controlled using mass flow controllers.

$$n_{\text{H}_2} = (1[A]) = \left(\frac{1 \left[\frac{\text{C}}{\text{sec}} \right]}{1[A]} \right) \times \left(\frac{1 [C]}{e \left[\frac{\text{amount of C}}{1 e^-} \right]} \right) \times \left(\frac{1}{N_A \left[\frac{\text{number of } e^-}{1 \text{ mol } e^-} \right]} \right) \times \left(\frac{1 \text{ mol H}_2}{2 \text{ mol } e^-} \right) \times \left(\frac{60 \text{ sec}}{1 \text{ min}} \right)$$

$$= X \left[\frac{\text{mol}}{\text{min}} \right]$$

1.11

$$\dot{m}_{\text{H}_2} = X \left[\frac{\text{mol}}{\text{min}} \right] M_{\text{H}_2} \left[\frac{\text{g}}{\text{mol}} \right] = X M_{\text{H}_2} \left[\frac{\text{g}}{\text{min}} \right]$$

1.12

$$\dot{m}_{\text{Air}} = \frac{\dot{m}_{\text{H}_2}}{2} \times \frac{100}{21} \left[\frac{\text{g}}{\text{min}} \right]$$

1.13

Avogadro's number: $N_A = 6.02214E + 23 \left[\frac{1}{\text{mol}} \right]$

Elementary charge: $e = 1.60218E - 19 [C]$

1.6.4 Purge process of a flow-through cathode PEMFC

At high current density, the cell generates more and more water in the form of droplets at the wall of bipolar plate channels. The droplets grow bigger over time due to the chemical reaction of PEMFC. Once they are big enough to block the channel, a flood takes place. Following that, the COP increases dramatically until it is enough to push the droplets out. In the meantime, the output voltage and current plunge sharply significantly. Once droplets are pushed out, the cell outputs soar rapidly to peaks that are higher than usual and then gradually fall back to normal values.

The approach to purging droplets in a proton exchange membrane fuel cell out must balance power density and output stability. Various purging strategies can be employed to maintain a consistent power density output. A unique technique was employed to refine the purging strategy. Initially, the focus is on ensuring the stability of cell outputs, followed by selecting a strategy that maximizes power density. Through this approach, an optimal purging strategy will be identified. This study offers insights for enhancing the purging strategy of single proton exchange membrane fuel cells.

This research introduces a novel approach for controlling the cathode operating pressure to facilitate droplet purge within the PEMFC. A solenoid valve, located at the cathode outlet manifold, enables rapid adjustments to COP based on its status, demonstrated in **Figure 1.7**.

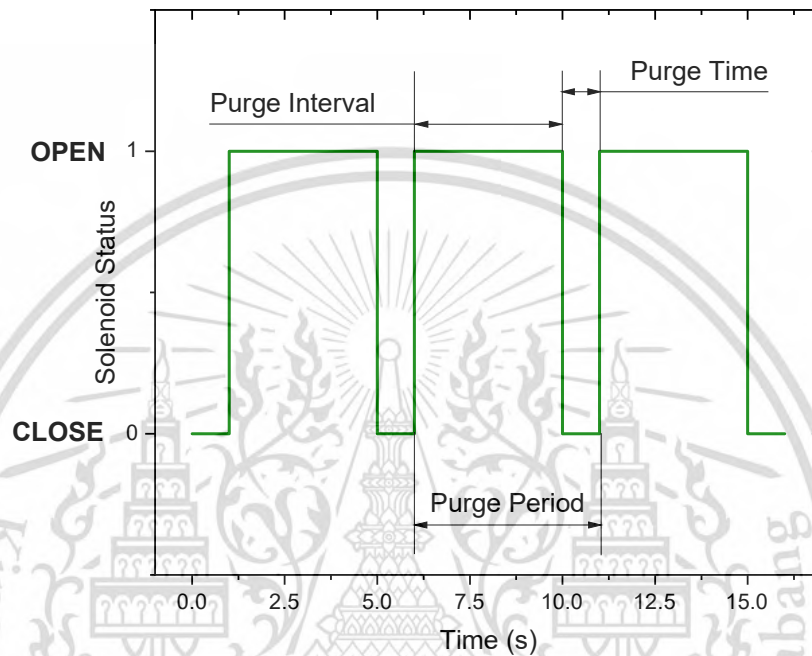


Figure 1.7 Describe the purge period

When the solenoid is controlled to close, the COP would increase due to the back pressure rise. Conversely, when opened, COP swiftly decreases, and accumulated droplets are expelled. This technique is similar to the typical operation of a cell since the droplets are formed naturally until it blocks the bipolar plate channels leading to COP increase up to a specific level, and the droplet is pushed out. Moreover, this technique can flexibly control the purge duration and purge interval time, which benefits the droplet purging strategies and PEMFC performance enhancement.

CHAPTER 2

LITERATURE REVIEW

This literature review synthesizes significant research findings related to the operation and optimization of PEMFCs, focusing on the effects of various operating parameters, test systems, and innovative methods for performance enhancement. These insights provide a comprehensive foundation for the three main parts of this thesis: designing a cost-effective PEMFC test system, evaluating the effects of operating parameters on PEMFC performance, and proposing a novel method for droplet purge to improve performance and stability.

2.1.1 Design of PEMFC test systems

A key focus of this thesis is the design of a cost-effective PEMFC test system. Yuzhen Xia et al. [29] designed a new test system for PEMFCs capable of monitoring and controlling inlet and outlet parameters and ensuring safety. Their system, utilizing Siemens S7-200 series PLC and PID technology, showed improved performance control, especially in terms of humidity, which was maintained with less than 0.7% error. This study highlights the importance of precise control over operating conditions to enhance PEMFC performance.

Amir Hossein Ahmadi et al. [30] and Ming Fang et al. [24] investigated bubble humidifiers for PEMFC systems, emphasizing the need for proper water management. Both studies found that optimal humidifier performance could be achieved by adjusting water temperature, water level, and inlet air flow. These findings underscore the necessity of incorporating efficient humidification methods in the test system design to maintain membrane hydration and improve fuel cell efficiency.

Moreover, from the viewpoint of FCEVs design, the large weight and size of the humidification system and heat dissipation are technical barriers that need to be resolved [31]. Additionally, RH has a greater impact on conductivity than OT, conductivity drops dramatically due to dehydration [29]. Efforts to eliminate the fuel cell subsystem as a humidification system are consequential to make the best FCEVs design [32].

In summary, achieving cost-effectiveness in PEMFC test systems requires balancing performance and component complexity. While existing systems, like Xia et

al.'s [29], demonstrate excellent control capabilities, their reliance on sophisticated PLCs might increase cost. This study aims to develop a cost-effective alternative that prioritizes essential functionalities while incorporating efficient humidification methods, as highlighted by Ahmaditaba et al. [30] and Fang et al. [24].

2.1.2 Influence of operating parameters on PEMFC performance

Evaluating the effects of operating parameters on PEMFC performance is crucial for optimizing fuel cell power density. Several studies applied orthogonal experimental design and range analysis to optimize the parameters of PEMFC under steady working conditions. Bohan Wang et al. [31], Dengcheng Liu et al. [33], and Shixiang Xia et al. [10] identified air stoichiometric ratio, operating temperature, and relative humidity as significant factors influencing PEMFC performance. Wang et al. [31] found air stoichiometric ratio to be the most critical parameter, followed by air relative humidity and operating temperature, with hydrogen relative humidity having minimal impact.

With the help of four factors (OT, gas inlet pressure, RH, and ASR) and three levels of the orthogonal table, Shixiang Xia et al. showed the results that the effects of ASR and gas inlet pressure on PEMFC performance are the largest under the conditions of medium-high and low current densities, respectively, while the OT and air RH have little impact on the performance of PEMFC [10]. Besides that, Dengcheng Liu et al. concluded the impact of ASR and OT on the output voltage of the stack was obviously higher than that of RH and backpressure regardless of the change of load conditions [33]. These studies performed the thought of full factorial. However, they showed the conflict's impact of OT on PEMFC performance. Part of the reason is that they neglected many cases owing to orthogonal experimental design, which helps to save time and effort in conducting experiments, so this method cannot achieve a comprehensive evaluation of parameter effects.

Yiming Xu et al. [34] and Huicui Chen et al. [35] explored the impact of relative humidity on PEMFC performance. Xu et al. [34] found that high anode relative humidity improved membrane hydration, while lower cathode relative humidity facilitated higher oxygen partial pressure, reducing water flooding at high current densities. Chen et al. [35] proposed a stepped load-shedding pattern to mitigate cathode flooding, suggesting that reducing load within a specific range can lower impedance and prevent water accumulation.

In conclusion, understanding the influence of operating parameters on PEMFC performance is essential for maximizing power density. While studies using orthogonal design methods like those by Xia et al. [10] and Liu et al. [33] highlight the importance of air stoichiometry ratio, operating temperature, and relative humidity, these methods may miss crucial nuances due to their limited scope. Further research, potentially involving full case designs, is needed to comprehensively understand the interplay between these parameters and optimize PEMFC performance. Additionally, studies by Xu et al. [34] and Chen et al. [35] emphasize the critical role of relative humidity management in mitigating water flooding, a key challenge for high current density operation. Future advancements in humidity control strategies will be crucial for achieving optimal FCEV designs.

2.1.3 Optimization and innovative methods for PEMFC performance enhancement

This thesis also aims to propose a novel method for droplet purging to enhance PEMFC performance. Several studies have explored gas purging strategies and water management techniques that can be adapted for this purpose. Kunyong Gong et al. [36] and Jun Shen et al. [32] investigated gas purging strategies for PEMFCs, highlighting the importance of purge intervals and durations in maintaining stable performance and preventing flooding. Gong et al. [36] found that an anode pressure of 60-70 kPa and a 4% purging ratio could achieve a balance between system efficiency and performance stability. Shen et al. [32] demonstrated that gas purging effectively removed water from PEMFCs, but excessive purging could lead to membrane dehydration and performance degradation.

Heng Shao et al. [37] and Qifei Jian et al. [38] provided insights into the dynamics of water droplet behavior and optimization of purge strategies in PEMFCs. **Figure 2.1** demonstrates water droplets are generated from the water inlets and gather together in the terminal phase. Subsequently, the majority of these droplets are eliminated from the gas passage through the corners during the purging phase. Shao et al. [37] used the volume of fluid method to simulate water accumulation and drainage, finding that larger water volumes and specific surface wettability improved purge efficiency. Jian et al. [38] emphasized the trade-off between hydrogen utilization and voltage stability, proposing an optimal purge strategy to balance these factors.

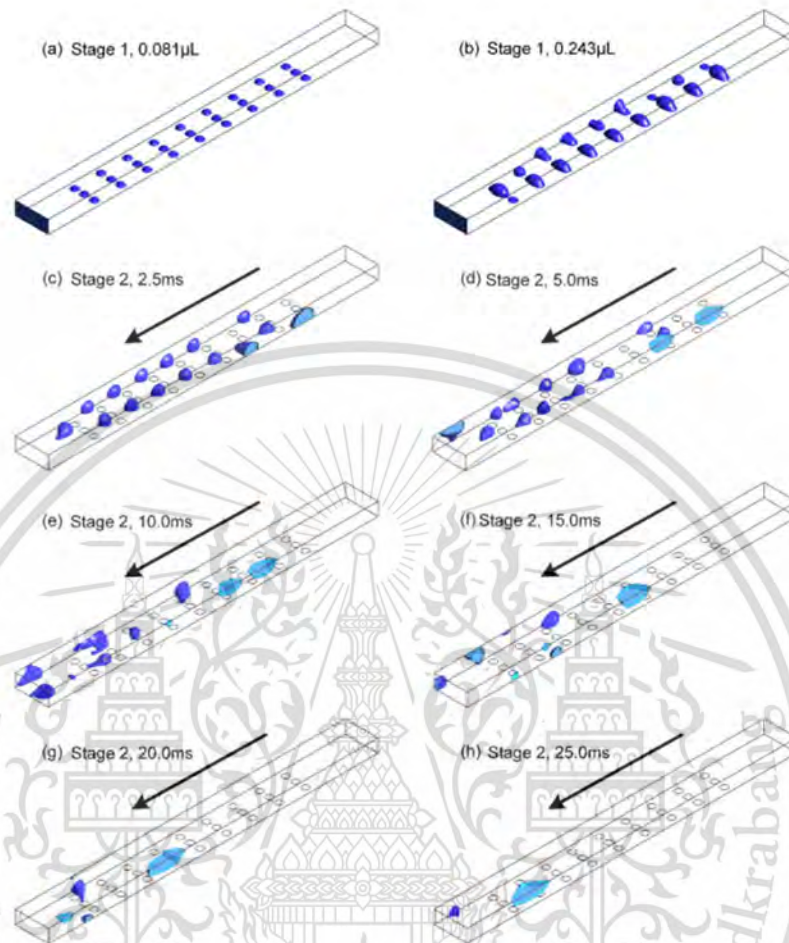


Figure 2.1 Liquid water dynamics in the gas channel in the base case: (a) 0.081 mL and (b) 0.243 mL in Stage 1 (interval), (c) 2.5 ms, (d) 5.0 ms, (e) 10.0 ms, (f) 15.0 ms, (g) 20.0 ms and (h) 25.0 ms in Stage 2 (purge) [37]

Research by Elif Eker Kahveci et al. [39], Yupeng Yang et al. [40], and Jing Yao et al. [41] provides valuable insights into the effects of operating parameters and water management in PEMFCs. Kahveci et al. [39] used the Design of Experiment (DoE) methodology to determine optimal operating conditions, showing that flow rates and temperature significantly affect performance. Yang et al. [40] investigated the effects of cathode humidity, air stoichiometry, hydrogen pressure, and current density on PEMFCs with a dead-ended anode, highlighting the importance of managing water accumulation to prevent performance decline. Yao et al. [41] developed a 3D transient

model to study the internal species transport and optimize purge strategies based on uneven distributions of field variables.

Overall, existing research on gas purging strategies and water management in PEMFCs provides a valuable foundation for developing a novel droplet purging method. Studies by Gong et al. [36] and Shen et al. [32] emphasize the importance of purge parameters like pressure, duration, and balancing efficiency with performance. Insights from Shao et al. [37] and Jian et al. [38] on water droplet behavior and purge optimization strategies further inform the design of this novel method. Additionally, understanding the influence of operating parameters and water management techniques, as explored by Kahveci et al. [39], Yang et al. [40], and Yao et al. [41], is crucial for tailoring the purging approach to specific PEMFC configurations. This thesis proposes a novel droplet purging method that leverages these combined learnings to enhance PEMFC performance by effectively removing water droplets while minimizing negative impacts on power density and stability. The effectiveness of this method will be evaluated through experimentation and compared to existing optimizing techniques.

The reviewed studies collectively underscore the complexity and interdependence of operating parameters in optimizing PEMFC performance. The orthogonal test method has proven effective in identifying key parameters and their optimal levels, but it may neglect certain interactions due to its reduced experimental design. This thesis aims to address this limitation by re-evaluating the identified optimal conditions through single-parameter variation tests. Moreover, the novel method of droplet purge via operating pressure management, as proposed in this research, builds upon the insights gained from gas purging and water management studies. By using a solenoid valve to control cathode back pressure, this method aims to purge droplets efficiently, preventing flooding and enhancing performance stability.

This literature review provides a comprehensive foundation for the three main parts of the thesis. The insights gained from the reviewed studies will guide the design of a cost-effective PEMFC test system, the evaluation of operating parameters, and the development of a novel droplet purge method. By integrating these findings, this thesis aims to contribute to the optimization and practical application of PEMFCs in various industries.

CHAPTER 3

RESEARCH METHODOLOGY

This chapter introduces the thought process and preliminary computations opted for as the basis of our design decisions.

3.1 RESEARCH METHODS

3.1.1 Systematic Literature Review (SLR)

Initially, a systematic literature review was conducted to gather existing knowledge and understand the theories and principles of Proton Exchange Membrane Fuel Cells (PEMFC). This method aids in the compilation of all pertinent publications and documents that meet our predetermined inclusion criteria for addressing a specific research inquiry. It employs clear and systematic procedures to minimize bias during the search, identification, evaluation, synthesis, analysis, and summarization of studies. When executed correctly and with minimal errors, this approach yields reliable findings and conclusions, which can inform decision-makers and scientific practitioners [42]. This involved the following steps shown in **Figure 3.1**.

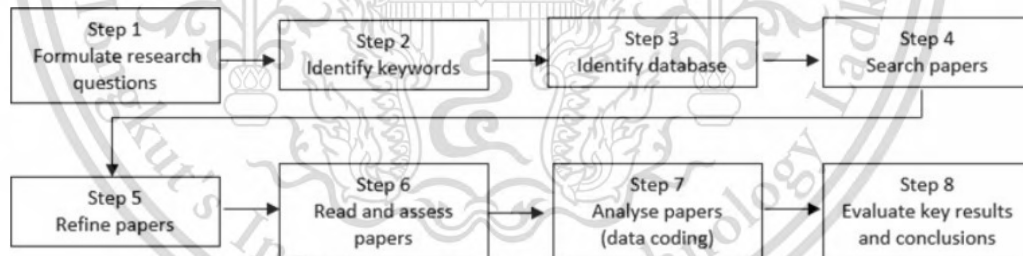


Figure 3.1 Steps of the SLR method [43]

To capture operating parameters' effect on PEMFC performance over 5 years from 2019 to 2023, the 'title/abstract/keyword' was used to have a comprehensive search through a powerful Scopus engine. The search protocol was initiated with a full syntax as follows:

'TITLE-ABS-KEY ((PEMFC OR PEFC) AND (performance) AND ("operating parameter") AND NOT (model))'. Further details regarding the search and article refinement process are provided in **Table 3.1**.

Table 3.1 Refining process of SLR

Search stage	Field	Keyword string	Number of results
1	Parameters	(TITLE-ABS-KEY (pemfc) AND TITLE-ABS-KEY (performance) AND TITLE-ABS-KEY ("operating parameters") AND TITLE-ABS-KEY (experimental))	141
	Purge	(TITLE-ABS-KEY (pemfc) AND TITLE-ABS-KEY (performance) AND TITLE-ABS-KEY (purge) AND NOT TITLE-ABS-KEY (model))	132
2	Parameters	Limiting the search to English Journal	95
	Purge	Articles	88
3	Parameters	Excluding irrelevant subject areas such as	46
	Purge	Physics and Astronomy, Chemistry, Mathematics, Computer Science, Social Sciences, Multidisciplinary, Agricultural and Biological, Sciences.	21
4	Parameters	Limiting to ten-year studies only (from 2014 to 2024)	32
	Purge		19
5	Parameters	Reading through the titles and abstracts and	24
	Purge	details of the articles	17

The initial result of the search process using the 'title/abstract/keyword' has provided 273 articles from listed journals. After that, the search process continued with only collecting English Journal Articles and therefore, 183 articles remained. Next, irrelevant subject areas needed to be excluded such as Chemical Engineering; Physics and Astronomy; Biochemistry, Genetics and Molecular Biology; Environmental Science;

etc. At the end of this step, 67 articles were chosen accordingly. Following that, the search was limited to only recent articles in 10 years, and this refined the literature search to 51 articles. After a skim and scan of the titles received in the database, the results received, articles related to “high-temperature PEMFC, 2D/3D-dimensional, etc.” were neglected. Then the selected literature was thoroughly read and analyzed to gain insights into the fundamental principles, recent advancements, and challenges in PEMFC technology. Finally, 41 articles were relevant and would be used for references.

3.1.2 Experimental investigations

3.1.2.1 Construction of test system

Experimental studies were conducted to explore the impact of different operating parameters on the performance of PEMFC and to optimize them for enhanced output power density. The experimental procedure comprised the construction of a test system, a bespoke test system was developed to facilitate experimental investigation into the operational parameters of PEMFC. The construction of the test system involved:

- Design Considerations: Careful consideration was given to the design parameters of the test system to ensure its suitability for investigating various operational aspects of PEMFC.
- Component Selection: The selection of appropriate components, including tools for the four-parameter control system, mass flow controller, pressure sensors, purge valve, and data acquisition system, was carried out to meet the experimental requirements.
- Assembly and Calibration: The test system was assembled and calibrated to ensure accuracy and reliability in measuring and controlling the operating parameters of PEMFC.

3.1.2.2 Orthogonal test design

This research utilized the orthogonal test design (OTD) methodology to investigate the influence of operating parameters on PEMFC performance. OTD is a DOE technique proven effective in optimizing complex systems with multiple factors and levels [44, 45]. It achieves this by strategically selecting a reduced set of

representative test cases that offer statistically significant data compared to a full factorial design requiring numerous experiments [46, 47]. This approach significantly reduces testing time and resources while enabling rapid identification of optimal parameter combinations [47].

OTD offers several advantages for PEMFC optimization. Similar to Yuan et al.'s application in direct methanol fuel cells [48], this method allows us to efficiently assess the dominant factors impacting PEMFC performance. By following Xia et al.'s approach of employing OTD for PEMFC parameter optimization [10], we can achieve efficient exploration of the design space and identify key factors influencing performance.

The core concept of OTD lies in leveraging orthogonal arrays to select representative experiments. These arrays ensure minimal interaction between factors, allowing for independent analysis of their effects. This approach significantly reduces the number of required experiments compared to a full factorial design [33]. While a full factorial design of a 4-factor, 3-level experiment would demand 81 ($3 \times 3 \times 3 \times 3$) experiments, OTD strategically selects a smaller subset (only 9 experiments) that provides sufficient information for robust analysis. This selection ensures the chosen experiments effectively cover the entire parameter space, enabling us to draw meaningful conclusions despite the reduced number of tests.

In summary, this research leverages OTD as a powerful tool to optimize PEMFC performance. This method allows for efficient exploration of the design space, identification of key influencing factors, and ultimately, the determination of optimal operating parameters for our PEMFC system.

3.2 OPERATING PARAMETERS SELECTION

Typical values of operating parameters in previous studies are listed in **Table 3.2**.

Table 3.2 Operating conditions of PEMFC in previous studies

Ref	Active area (cm ²)	OT (°C)	RH (%)	ASR	HSR	Pressure
[49]	50 (Single)	70, 80, 90 ^a	(C) 0, 50, 100	2.5	1.5	(C) 0, 50, 100 (kPa) ^d

[10]	250 (Single)	60, 70, 80 ^a	40, 50, 60	1.8, 2.0, 2.5	2.0	(C) 70, 80, 90 (kPa) ^c
[34]	25 (single)	(A), (C): 90 ^c	(A), (C): 50, 70, 90.	900 mL/min	300 mL/min	(A), (C): 1.5 (atm) ^c
[31]	285 (single)	65, 70, 75, 80 ^a	(A), (C): 30, 50, 70, 90	1.6, 1.9, 2.2, 2.5	1.5	ambient ^d
[33]	50 (5 cells)	65, 70, 75 ^a	40, 50, 60	1.5, 2.0, 2.5	1.5	0.6, 0.8, 1.0 (bar) ^d
[50]	2.25	80 ^a	70 ^b	40 mL/min	80 mL/min	0.15 (Mpa) ^d
[51]	25	40 to 70	(A) ^b : 40 to 80, (C) ^b : 40 to 70	250 sccm to 400 sccm	250 sccm to 350 sccm	1–3 (bar) ^a , 0–3 (bar) ^d
[52]	250 (12 cells)	348 (K)	(A), (C) ^b : 333 (K)	2.0	1.5	(A) ^d 0.5 (bar), (C) ^d 0.4 (bar)
[53]	5 (single)	70	(A), (C): 100	5.71 (800cm ³ / min)	2.55 (150cm ³ / min)	(A) ^d : 0, 0.3, 0.6, 1.5, and 2.1 (bar); (C) ^d : 0, 0.5, 1.0, 2.0, and 3.0 (bar)

Where:

^a Operating Temperature/Pressure

^b Humidifier/Gas-feed Temperature

^c Inlet Pressure/Gas

^d Back/Outlet Pressure

Based on the theoretical operating ranges of parameters and previous experimental studies' conditions, the operating parameters in this research were chosen in **Table 3.3**.

Table 3.3 Four operating parameter values

Level	Factor			
	OT (°C)	RH (%)	COP (psi)	ASR
1	60	50	8	1.8
2	70	60	15	2.4
3	80	70	22	3.0

3.3 TOOLS AND TECHNIQUES

3.3.1 Tools for test system construction

3.3.1.1 PEMFC

In a single PEM fuel cell, several components work in tandem to facilitate its operation. These include the MEA, Gas Diffusion Layer (GDL), gaskets, flow fields, current collectors, and end plates, illustrated in **Figure 3.2**. The flow field is structured with a triple serpentine channel (3S), allowing gases to flow in a co-directional manner. Current collectors, fabricated from copper coated with gold, are utilized along with end plates coated with aluminum and gold. Furthermore, the fuel management system of the PEMFC operates in a flow-through mode, whereby fuel and air are directly released into the ambient environment.

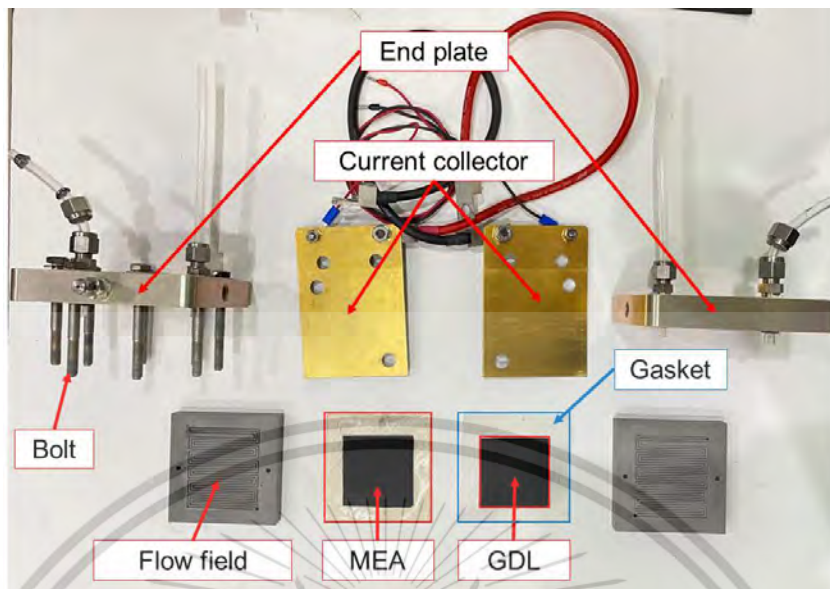


Figure 3.2 PEMFC components

This research used two types of MEA including Nafion 112 and PFSA S30-R ePTFE Reinforced PEM for the two-parameter test and four-parameter test, respectively. Their specifications are illustrated in Table 3.4.

Table 3.4 Specifications of the two MEAs

Type	Nafion 112	PFSA S30-R ePTFE Reinforced PEM
Test	Two parameters (OT and RH)	Four parameters
Active area (cm ²)	25	25
Anode Pt loading (mg/cm ²)	0.3	0.1
Cathode Pt loading (mg/cm ²)	0.3	0.32
Thickness (μm)	50	30

3.3.1.2 Temperature controller

Five sets comprising temperature controllers, Type T thermocouples, solid-state relays (SSRs), and heaters were employed for the manual control and monitoring

of temperature across two humidification bottles, the PEM fuel cell, and two pre-heaters demonstrated in **Figure 3.3**.

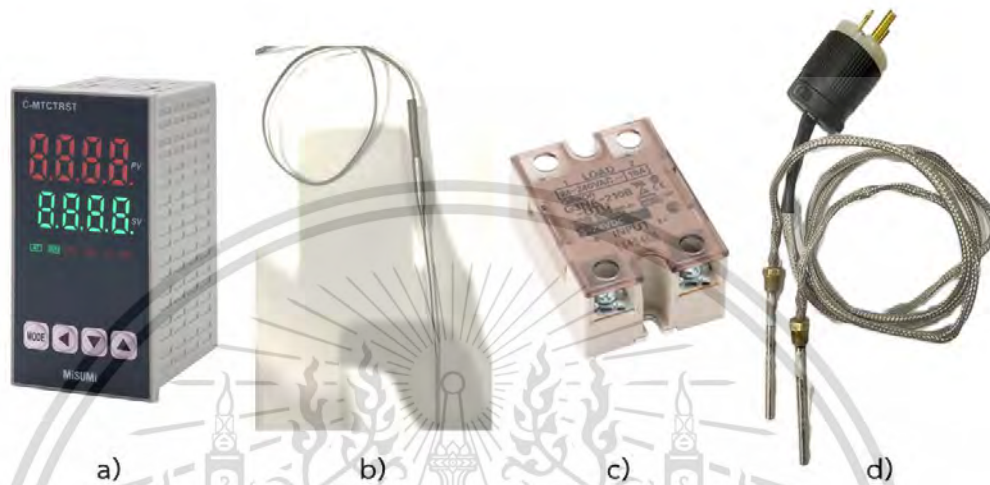


Figure 3.3 Temperature control unit a) temperature controller from MiSUMi Economy, b) thermal couple type T, c) SSR, and d) heater

The Economy Series Temperature Controllers offer ease of operation and quick learning at a budget-friendly price point. They exhibit superior temperature drift and stability compared to other instruments within the same category, resulting in notable energy-saving benefits. Specifically engineered for applications requiring temperature regulation within the range of 0.1-999.9 °C, such as light industrial machinery and environmental heating/cooling systems, these controllers boast simplicity in selection, setup, and operation. Detail of the temperature controller specifications is shown in **Table 3.5**. With comprehensive functionality and robust performance, they are well-suited for temperature control within PEMFC systems, making them an optimal and cost-effective solution.

Table 3.5 Specifications of the Economy Series temperature controller [54]

Model	C-MTCTRST
Input	Thermal couple type T
Power Supply Voltage	100V-240VAC, 50Hz
Relay output	Relay Contact Output (AC220V/DC30V, 5A)
Logic level output	When ON: DC12V; When OFF: DC0.5V or less; Maximum current: 30mA, load resistance $\geq 1K$
Control Method	ON-OFF Control / PID Control with Self-Tuning / PID Control with Self-Tuning / PI Control / PD Control / P Control / Thermostats
Failure Detecting Function	Heater Breakage
Communication	RS485
Resolution	0.1°C
Measurement Accuracy	$\pm 0.5\%$ FS
Working environment	Ambient temperature: 0°C-50°C Relative humidity: 35%-85% RH (with no condensation)

3.3.1.3 Humidification bottle

Figure 3.4 illustrates humidity bottles crafted from type 316 stainless steel, featuring Swagelok fittings for gas inputs and outputs seamlessly integrated through welding. Coiled within the bottle is Nafion tubing, designed to maintain the desired dew-point humidity level for gases traversing through it. To regulate temperature, the bottle is both insulated and heated using a silicone rubber flex-pad.



Figure 3.4 Humidification bottle from Fuel Cell Technologies, Inc.

The impact of gas flow rate on the outlet bottle dew point was evaluated by Fuel Cell Technologies, Inc. employing 1 meter of Nafion tubing. The humidity bottle controller was set to 80 °C and allowed to stabilize under gas inlet conditions. Subsequently, the outlet dew point (DP) °C of the humidity bottle was recorded, as depicted in Figure 3.5.

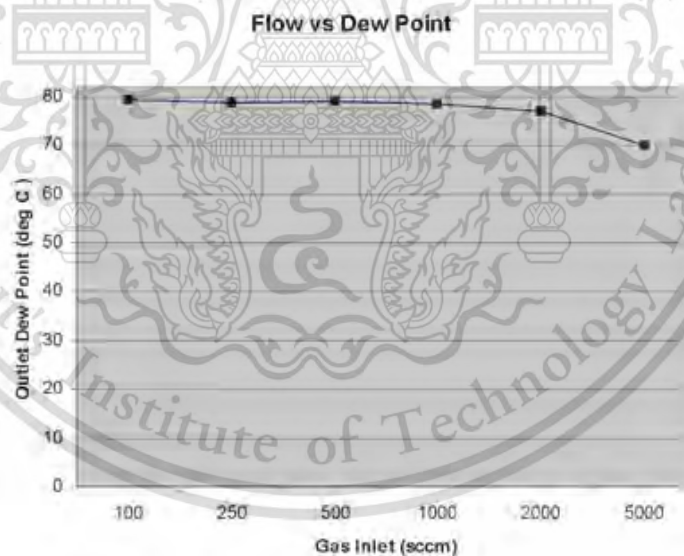


Figure 3.5 Outlet dew point over increasing gas flowrate [55]

The results revealed that the outlet dew point of the humidification bottle decreases with escalating flows, particularly noticeable at higher rates. Through flow calculations conducted in this study, it was determined that gas flow rates not

exceeding 650 sccm exhibit minimal influence on the dew point, with deviations of only around 1-2 °C.

3.3.1.4 Mass-flow controller

This research employed a mass flow controller (MFC) DPM series from the Aalborg Instruments & Controls as seen in **Figure 3.6**.



Figure 3.6 Digital mass-flow controller from Aalborg® Instruments & Controls

These MFCs utilize a differential pressure sensor to precisely measure the pressure drop across a specifically designed restriction flow element (RFE). The RFE geometry ensures laminar flow within the operating range from 0 to 133% FS, enabling an accurate correlation between the differential pressure and volumetric flow rate according to established fluid dynamics principles. Specifications of MFC are illustrated in **Table 3.6**. Additionally, the MFC incorporates high-precision absolute pressure and temperature sensors. These combined measurements are employed to calculate the mass flow rate using the ideal gas law [56]. Moreover, they are also used to calculate the COP by observing the inlet gas pressure.

Table 3.6 Specifications of mass-flow controller [56]

Model	DPC17
Fluid (operating flow range)	Hydrogen (0-500 sccm), Air (0-20,000 sccm)
Maximum Input pressure	120 psi (8.3 bar)
Ingress Protection	IP40
Flow accuracy	$\pm(0.5\% \text{ RD} + 0.2\% \text{ FS})$ at calibration conditions
Repeatability	$\pm 0.2\%$ of full scale

Typical flow response time	150 ms
Operating temperature	-10 to 60 °C

RD: Reading “Closeness to the actual value expressed as a percentage of the actual value.” With Reading, the accuracy is the percentage of what is being read. The percentage stays the same, no matter where the flow is in the flow range. If it is 1% at 200 ln/min it would be 1% at 100 ln/min.

FS: Full scale “Closeness to the actual value expressed as a percentage of the maximum scale value.” With Full Scale, the error remains the same but the percentage changes as the flow goes up and down the flow range. If the accuracy is calibrated 1% of 200 ln/min then the error is $0.01 \times 200 \text{ ln/min} = 2 \text{ ln/min}$.

The selected MFC offers multi-gas functionality. This feature allows users to choose the specific gas being measured through either the local display interface or a digital communication interface [2]. This versatility simplifies the configuration process and streamlines operation for various gas compositions. In this research, hydrogen and air were utilized for PEMFC, the MFC calibration certificates for these gases are shown in Appendix A.

3.3.1.5 Needle valve and pressure sensor

A manually operated needle valve was employed to regulate the back pressure at the outlet of the PEMFC stack as shown in Figure 3.7. This valve is constructed from stainless steel, ensuring durability and corrosion resistance in the PEMFC environment. It features a positive leak-tight shut-off design, guaranteeing a complete seal when fully closed.



Figure 3.7 Integral Bonnet Needle Valve NV Series from Hy-Lok Corporation

The inlet and outlet connections of the needle valve utilize ¼ inch tube fittings for compatibility with standard tubing sizes in this PEMFC system. The valve design allows for up to 9 handle turns, enabling smooth and precise adjustment of the back pressure experienced by the PEMFC. The detailed specifications of this needle valve are provided in **Table 3.7**.

Table 3.7 Specifications of needle valve [57]

Model	NV2H-4T-S316
Material	Stainless steel/ SS316
Pressure -Temperature rating	200 F (93 °C) – 5160 psi (355 kPa)
Stem	Up to 450 F (232 °C)
End connections	Fractional Hy-lok tube fittings 1/4”

Together with the needle valve, a pressure sensor from SMC Corporation with a 1-5V analog output was incorporated into the system to collect back pressure data from the PEMFC outlet as shown in **Figure 3.8**. This voltage range is well-suited for direct reading by the Arduino microcontroller employed in the data acquisition system.



Figure 3.8 Compact Pressure Sensor from SMC Corporation

One critical consideration in selecting this sensor was its ability to operate reliably in the humid conditions typically encountered at the cathode outlet of the PEMFC. To address this requirement, the sensor is capable of withstanding humidity levels of up to 85% RH in the gas environment. Furthermore, the pressure sensor has a measurement range spanning from 0 to 1 MPa, with an impressive accuracy of $\pm 1\%$ Full Scale (F.S.). Detailed specifications outlining its performance characteristics are provided in **Table 3.8**, which is sufficient for capturing the pressure data required for this research.

Table 3.8 Specifications of pressor sensor [58]

Model	PSE540A-01
Rated Pressure range	0 to 1 MPa
Applicable fluid	Air, inert gases, and incombustible gases
Power supply voltage	12 to 24 VDC $\pm 10\%$
Analog output specification	1 to 5 VDC
Accuracy (at 25°C)	$\pm 1\%$ F.S. (rated pressure range)
Linearity	$\pm 0.7\%$ F.S.
Repeatability	$\pm 0.2\%$ F.S.
Enclosure	IP40
Operation temperature	Operation: 0 to 50°C
Operation RH	35 to 85% RH
Withstand voltage	1000 VAC or more (50/60 Hz), 1 minute
Insulation resistance	50 M Ω or more at 500 VDC

3.3.1.6 Solenoid valve

To remove water droplets from the cathode side, a high-speed solenoid valve from Airtac was implemented at the outlet demonstrated in **Figure 3.9**.

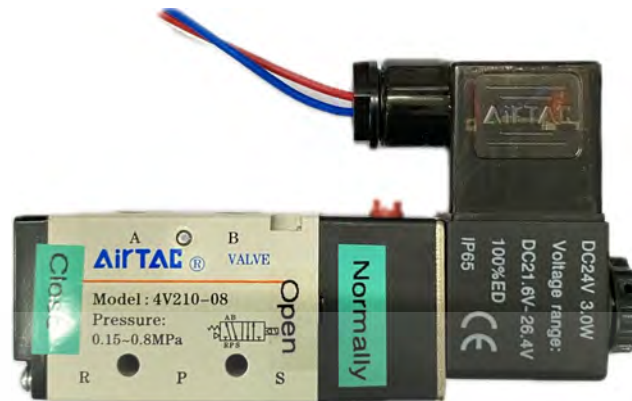


Figure 3.9 Solenoid Valve 4V200 Series from AirTAC

This valve selection was based on its ability to operate at high frequencies (up to 5 cycles per second) and its rapid activation time of fewer than 0.05 seconds shown in **Table 3.9**. These characteristics ensure the proper operations of various purging strategies in this research.

Table 3.9 Specifications of solenoid valve [59]

Model	4V210-8-B
Fluid	Air
Port size	In=Out=1/4", Exhaust=1/8"
Orifice size	Cv = 1.0
Valve type	5 ports 2 positions
Operating pressure	0.15-0.8 MPa (21-114 psi)
Temperature	-20 to 70 °C
Material	Aluminum alloy
Max frequency	5 cycle/ sec
Coil voltage	DC24V ±10%
Protection	IP65 (DIN40050)
Activating time	≤ 0.05 sec

3.3.1.7 Electronic load

A high-power DC electronic load (model IT8811) from ITECH Electronics was employed to simulate the load experienced by the single PEM fuel cell shown in

Figure 3.10. This electronic load offers a maximum power capacity of 150W, suitable for testing small PEMFCs.



Figure 3.10 High Power DC Electronic Load from ITECH Electronics

As described in **Table 3.10**, the IT8811 model features high-speed voltage and current measurement capabilities of up to 25 kHz, with a resolution of 0.1 mV and 0.01 mA, respectively. This enables precise characterization of the PEMFC's output. Additionally, the adjustable measurement current rising speed (0.001 A/ μ s to 2.5 A/ μ s) allows for dynamic load testing, simulating realistic operating conditions for the PEMFC.

Table 3.10 Specifications of electronic load [60]

Model	IT8811
Power	150W (or 120V/30A)
Mode	CV/CC/CR/CW
Measurement resolution	0.1mV, 0.01mA
Dynamic mode	up to 25kHz
Communication interface	RS232/USB
Accuracy	Readback voltage: $\pm (0.025\% + 0.025\%FS)$
	Readback Current: $\pm (0.05\% + 0.05\%FS)$
	Readback Power: $\pm (0.1\% + 0.1\%FS)$

Additionally, it comes equipped with a built-in RS232 and USB interface, facilitating communication with a computer for control and data acquisition. LabVIEW drivers are readily available for this model, enabling seamless integration into the testing environment.

The IT8811's combination of high power capacity, fast and precise measurement capabilities, dynamic load control, and straightforward communication interface make it a suitable choice for testing small PEMFC stacks in this research.

3.3.1.8 Arduino

Arduino is an open-source electronics platform renowned for its user-friendly hardware and software. Arduino boards are capable of receiving inputs from various sources, such as sensors or buttons, and translating them into desired outputs, such as activating motors or electronic valves. This functionality is achieved through programming the microcontroller on the Arduino board using the Arduino programming language, which is based on Wiring. The Arduino Software (IDE), based on Processing, serves as the interface for programming Arduino boards. Additionally, Arduino projects can operate independently or communicate with software applications running on a computer, such as Flash, Processing, or MaxMSP. Notably, Arduino can establish a connection with LabVIEW via USB, expanding its versatility in interfacing with other software tools.



Figure 3.11 Arduino Uno R3 board

Figure 3.11 shows an Arduino board which is used for controlling the solenoid valve in the droplet purge experiment.

3.3.2 Techniques

3.3.2.1 - Pressure sensor calibration

Pressure sensors are typically designed for a linear response to working pressure as seen in **Figure 3.12** and **Table 3.11**. However, installation within a system can affect their signal, causing an offset from calibration data. To address this, system calibration is necessary to determine the offset value and corrective equation.

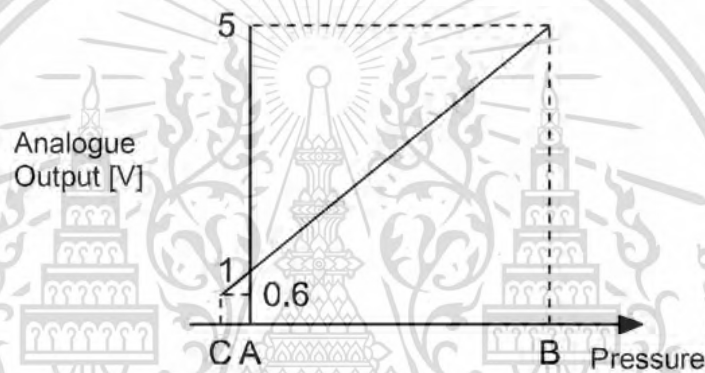


Figure 3.12 Pressure sensor calibration data from SMC

Table 3.11 Pressure range of pressure sensor

Range	Rated pressure range	A	B	C
For vacuum	0.0 to -101 kPa	0	-101 kPa	10.1 kPa
For compound	-100 to 100 kPa	-100 kPa	100 kPa	-
For positive pressure	-0 to 1 MPa	0	1 MPa	-0.1 MPa

In this particular setup, the pressure sensor was set up with a nitrogen gas feed. A regulator adjusted the gas pressure, which was monitored by a pressure gauge demonstrated in **Figure 3.13**.

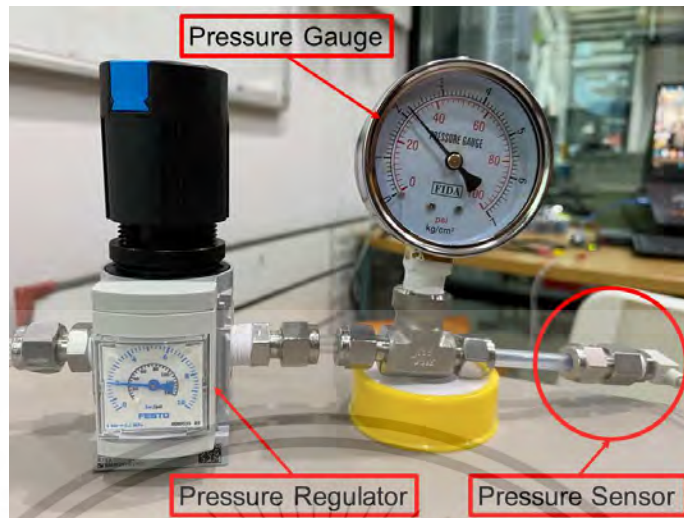


Figure 3.13 Pressure sensor calibration setup

By varying the pressure level and recording the sensor's analog signal, the calibration equation was established. This equation includes an offset value of 195.31 and a slope of 80.052, as shown in Figure 3.14.

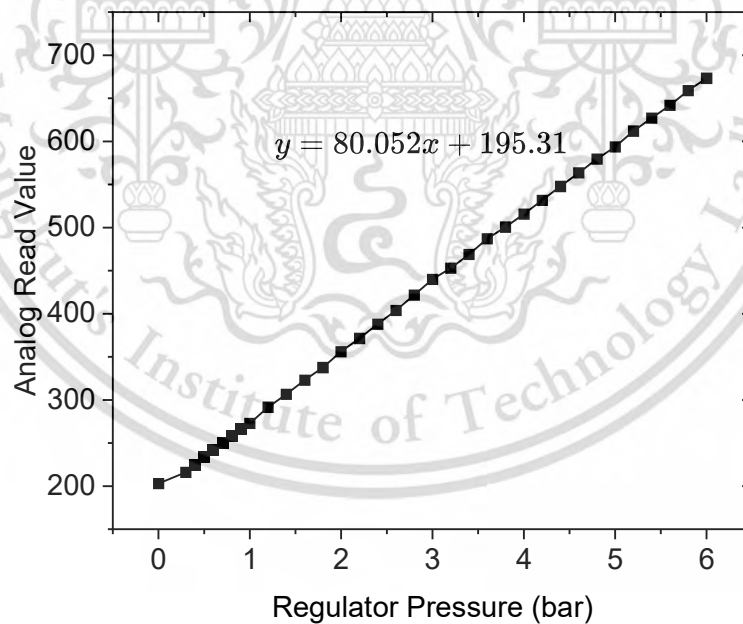


Figure 3.14 System calibration graph of the pressure sensor

It's important to note that the sensor's analog signal represents the average of one minute's data acquisition. The detailed Arduino code for this process can be found in **Appendix C**.

3.3.2.2 - LabVIEW – Arduino communication

LabVIEW (Laboratory Virtual Instrument Engineering Workbench) is a visual programming language crafted by National Instruments. LabVIEW is particularly valuable for its versatility in data acquisition, instrument control, and industrial automation tasks, aligning perfectly with the objectives of our study.

LabVIEW offers several advantages for HMI development in this research. First, its graphical programming language simplifies the creation of user interfaces compared to traditional text-based programming [1]. Second, LabVIEW integrates seamlessly with National Instruments hardware, offering pre-built functions for data acquisition and instrument control. However, the primary advantage of this work is the ability to communicate with external devices through standard protocols like VISA (Virtual Instrument Software Architecture) [1]. This flexibility allowed the use of a cost-effective alternative to National Instruments hardware for data acquisition. While LabVIEW offers robust integration with National Instruments hardware, its cost can be a limiting factor for some projects. To address this limitation, this research utilized an Arduino microcontroller for data acquisition. LabVIEW's built-in VISA capabilities facilitated communication with the Arduino via USB, enabling the use of a more cost-effective platform for sensor data acquisition while leveraging LabVIEW's powerful HMI development environment.

3.4 DATA COLLECTION PROCEDURES

3.4.1 Activation

A freshly manufactured polymer electrolyte membrane (PEM) fuel cell typically undergoes a designated break-in or conditioning period to become operational and achieve optimal performance [1]. This period serves to test and condition the membrane electrode assemblies (MEAs) and other assembled components, ensuring that the fuel cell stack operates within specified parameters before full system assembly. Typically, during this break-in period, cell performance gradually improves

until it reaches a stable level, without further increase. Several theories have been proposed to explain the conditioning process:

(i) Activation of the fuel cell may have beneficial effects on the catalyst, such as removing impurities introduced during manufacturing, activating inactive catalysts, and establishing efficient reactant transfer pathways to the catalyst [8].

(ii) Newly assembled fuel cell stacks often require an incubation phase to optimize the membrane performance. This could be due to catalyst residue or initial membrane dryness, which may hinder performance until hydration occurs during the incubation period [9].

(iii) Over time, advancements in electrode structures, from PTFE-bonded [10] electrodes to Nafion-impregnated PTFE-bonded [11] electrodes and Nafion-bonded [12] electrodes, have improved PEM fuel cell performance. The introduction of Nafion electrolyte extends the electrode reaction zone, enhances ionic conductivity, and boosts catalyst utilization. However, the initial performance of MEAs with Nafion-bonded electrodes typically improves over time as the electrodes require hydration for effective hydrogen ion transport. These theories highlight controlling water content as a critical requirement for successful fuel cell stack activation.

In this study, a 11-hour traditional MEA conditioning procedure was conducted, involving open-circuit operation with nitrogen for impurity purging and cell wet-up in two hours followed by gas exposure for controlling current density for specified durations to achieve optimal conditioning. The operating conditions set for the activation process are OT 80°C, RH 100%, COP 14.5 psi, and the flow rate at the anode and cathode are 200 sccm and 500 sccm, respectively. During the activation process, the cell potential was monitored and recorded at various current densities (with 10 seconds sampling rate) as a function of time shown in **Figure 3.15**.

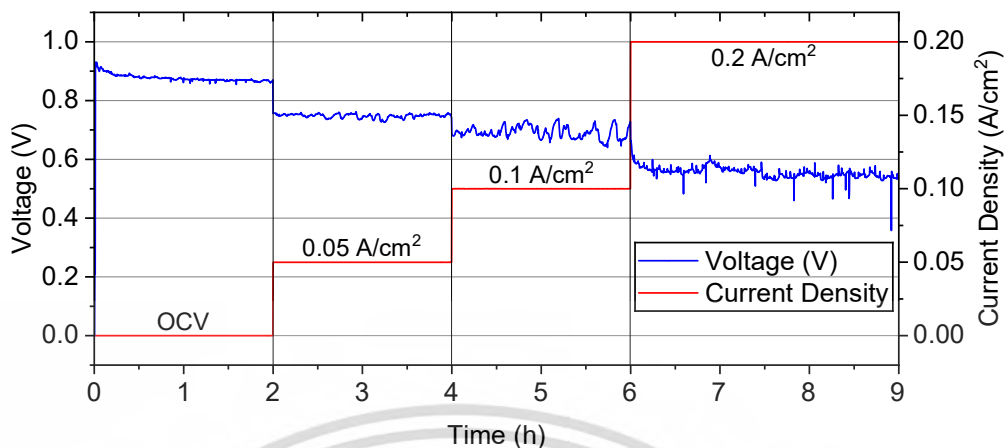


Figure 3.15 Activation process

It can be observed from **Figure 3.15** that the cell potential started to stabilize after 7.5 hours being conditioned with CC mode. The output voltage seems no more increase and droplets have been pushed out frequently since then. After break-in completion, the cell polarization curve was drawn as the initial characteristic of the cell, which is demonstrated in **Figure 3.16**.

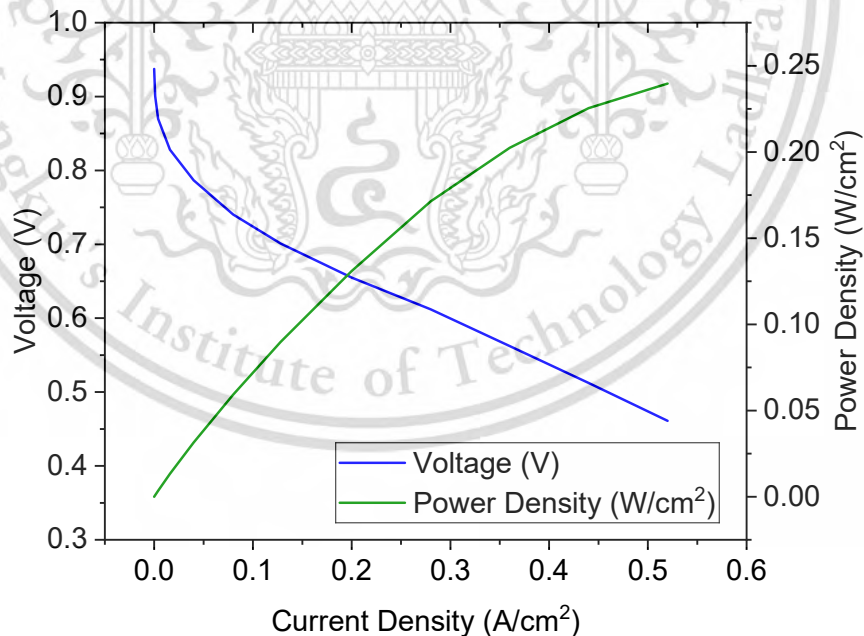


Figure 3.16 Initial PEMFC performance

Figure 3.16 shows the very first state of the MEA used in this study, which is operated at the activation conditions. Therefore, the cell could reach approximately 0.94 V of OCV and supply up to 0.5 A/cm² of current density.

3.4.2 Defining lower limits of the air flow rate and ASR

Following the activation process, the MEA is deemed adequately hydrated and prepared for testing. However, considering the diverse test conditions ranging from minimal to substantial loads in this study, and with air mass-flow controllers boasting an accuracy of 0.2% within the rated range and 0.5% at full scale, setting the flow rate too low may introduce inaccuracies. Additionally, to ensure comprehensive reaction coverage across the catalyst surface, the cell's flow field necessitates effective air diffusion throughout. Given these considerations, establishing the lower limits of air flow rate and ASR becomes paramount.

It's worth noting that hydrogen was set to a current of 15A, representing a notably high flow rate, consequently, the anode flow rate was not factored into the analysis.

3.4.2.1 Lower limit of the air flow rate

To ensure accurate outcomes, the process of establishing the lower limit of air flow rate was systematically carried out across all test conditions. For each condition, the cell operated with a consistent hydrogen flow rate of 172.4 ml/min and zero load. Subsequently, the air flow rate was gradually incremented by 0.01 l/min, commencing from zero until the OCV ceased to increase. Across the nine test scenarios, the lower limit of air flow rate was determined to be 0.05 l/min, corresponding to an OCV of approximately 0.92 V. In light of this discovery, the calculation for the required air flow rate was adjusted by incorporating the value of 0.05 l/min.

3.4.2.2 Lower limit of the ASR

Since not all ASRs are suitable for testing across a broad range of conditions, as exemplified by the nine test cases in this study, a targeted current density range of up to 0.5 A/cm² was chosen. Consequently, the selection of ASR values considered both established practices from prior research and experimental findings. While previous studies often employed ASR values of 1.5, 1.8, and 2.0, these proved

inadequate to provide sufficient air supply for all test conditions within this experiment. Therefore, the ASR range was adjusted for this study, utilizing a set of 1.8, 2.4, and 3.0.

3.4.3 Setup procedure

For each test scenario, the cell underwent an initial phase of Nitrogen gas infusion for 15 minutes to humidify the MEA and eliminate impurities, before transitioning to hydrogen gas and air. Subsequently, the setup procedure commenced by establishing the OT control value and awaiting the attainment of all designated temperature set points, ensuring the RH was also adjusted accordingly. Following this, the COP was fine-tuned by adjusting needle valves in alignment with the specific test parameters. Once the COP met the specified requirement, the load was applied, leading to an initial decline in COP due to the reaction's consumption to sustain the applied load. Consequently, the COP was readjusted to the appropriate value, and stability was awaited for data acquisition.

3.4.4 Data collection at steady state

Once the setup is finalized and the cell voltage stabilizes, data acquisition commences. The system records data points for five minutes at an adjustable sampling rate. Following data collection, a droplet purge is performed to refresh the cell's condition, ensuring a consistent starting point for each subsequent measurement.

Next, the applied load current (A) is adjusted according to the planned test conditions. The entire setup procedure is then repeated for each new test case.

3.4.5 Purge process between load levels of each test case

Begin by adjusting the load to 0 A, then switch from humid gases to dry gases. Proceed to gradually close the back pressure valve until its value reaches 1 bar, then open it to allow droplets to flow out. Repeat this process three times to ensure thorough purging of any remaining droplets.

3.5 DATA ANALYSIS METHODS

3.5.1 Range analysis

Range analysis is a statistical technique employed to assess the sensitivity of parameters within an orthogonal experiment. It achieves this by analyzing the range,

which is defined as the difference between the maximum and minimum values observed in the data for each parameter. A larger range signifies a greater impact of the parameter on the experimental outcome [61, 62]. The specific calculation process for determining the range will be outlined in **Equations 3.1 to 3.4**.

Difference between the average value of experimental results which contain factor X with m levels ($\overline{I_{Xm}}$) and the average value of all results (\overline{Y}):

$$\delta_{Xm} = \overline{I_{Xm}} - \overline{Y} \quad 3.1$$

The influence degree of the factor X:

$$T_X = R_{Xmax} - R_{Xmin} \quad 3.2$$

Where

$$R_{Xmax} = \max(\delta_{X1}, \delta_{X2}, \dots, \delta_{Xm}) \quad 3.3$$

$$R_{Xmin} = \min(\delta_{X1}, \delta_{X2}, \dots, \delta_{Xm}) \quad 3.4$$

3.5.2 Standard deviation

Standard Deviation (STDEV) describes the non-uniformity of variables or how spread out the data points are from the mean (average) of that specific population [41], demonstrated in **Equations 3.5 and 3.6**. A larger standard deviation indicates the data points are further from the mean, showing a greater spread or worse outputs' balance [33, 63].

$$STDEV = \sqrt{\frac{\sum_{i=1}^n (X_i - \overline{X})^2}{n}} \quad 3.5$$

$$\overline{X} = \frac{\sum_{i=1}^n X_i}{n} \quad 3.6$$

Where n is the test size of each condition, X_i is the cell outputs that vary over time, \overline{X} is the average values of cell outputs at each test condition.

CHAPTER 4

RESULTS

4.1 SELF-DESIGNED TEST SYSTEM

4.1.1 Configuration and operation

The self-design test system consists of seven main parts which are PEM single cell, human-machine interface, electronic load, temperature controllers, Humidification system, back pressure control system, and mass-flow controllers as shown in **Figure 4.1**.

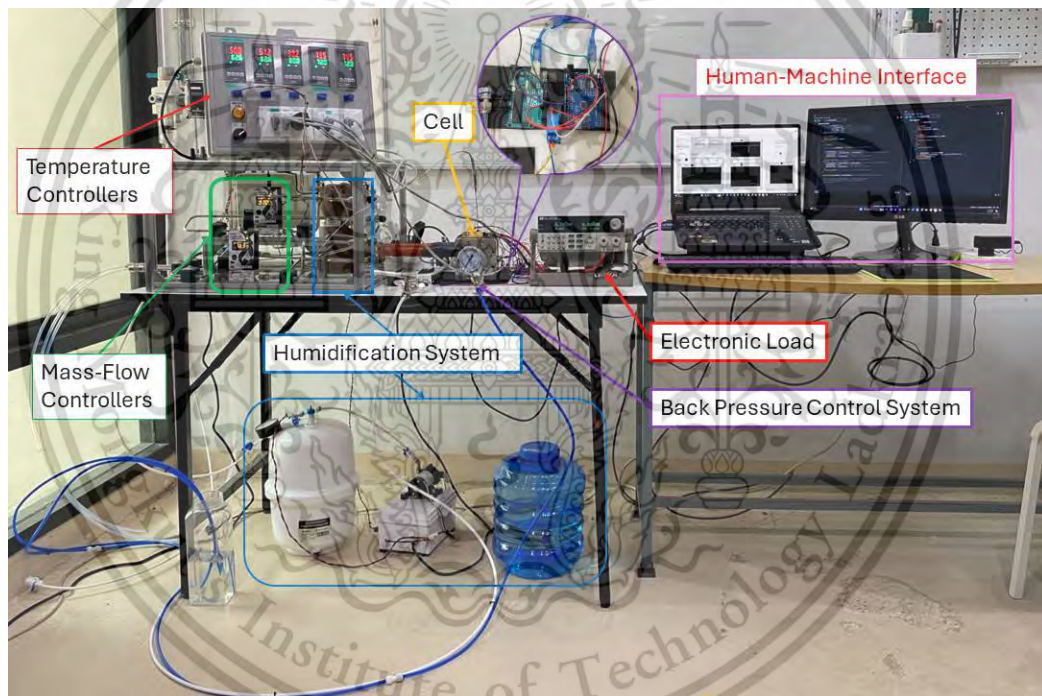


Figure 4.1 Test system photograph

In accordance with that, the test system can conduct the PEMFC performance tests with not only four operating parameters (OT, RH, COP, and ASR) but also various cell configurations (MEA, GDL, and bipolar plate). Moreover, the cathode outlet is equipped with the droplet purge system that enables to perform the purge strategy test. The four operating parameters, usually fixed during a test condition, are controlled and collected manually detailed in **Figure 4.2**. While the variables that often change

(load, purging time, interval time, plotting time, sampling rate) are controlled automatically via LabVIEW. Besides that, data such as voltage, current, back pressure, solenoid status, and real-time testing are acquired automatically through USB or Arduino to LabVIEW.

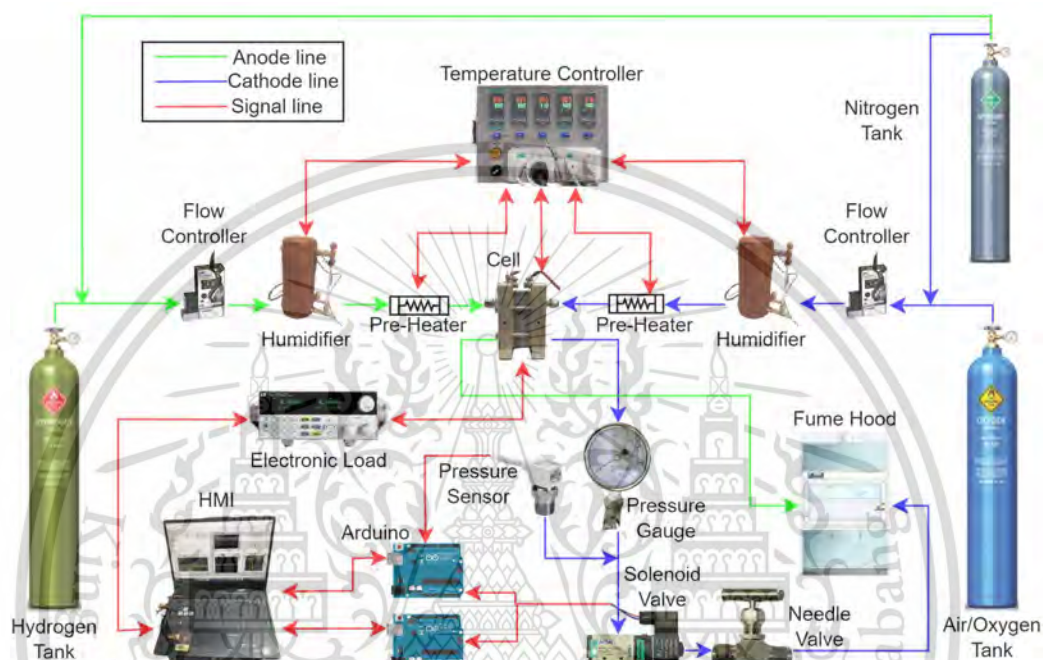


Figure 4.2 Test system schematic

As seen from the **Figure 4.2** that the test system is constructed of three main lines, anode line, cathode line, and signal line corresponding to the green line, blue line, and red line. It is worth noting that the system used the Swagelok tube and fittings to connect the gas line of all devices. This study used compressed gases from stored tanks with hydrogen (99.999%) as a reducer, air as an oxidant, and nitrogen as an inert gas for the start-up process.

Compressed gases are regulated to 44 psi and 29 psi for reactant gases and inert gas, respectively before coming into the mass flow controllers. Next, the flow rate is controlled at a specific value by mass flow controllers according to operating conditions. After that, gases are humidified with deionized (DI) water by humidifiers and then flow into the cell. Pre-heaters are installed at the cell inlet tubes to prevent humidified gases from condensing at the tube wall before flowing into the cell. The

OT is controlled by the temperature controllers through two heaters installed in the bipolar plates of the PEM cell.

The anode outlet connects to a tube leading to the fume hood for safety. While the cathode outlet is measured and monitored by a pressure sensor and pressure gauge then connected to solenoid and needle valves before heading to the fume hood. At the cathode side, COP is controlled by controlling the needle valve (controlling back pressure) together with monitoring the inlet and outlet/back pressure from the mass flow controller and pressure gauge, respectively. Additionally, the cathode purge valve is controlled and logged data together with the back pressure through Arduino-LabVIEW. The outputs of the cell are connected to an electronic load which is controlled and logged data through USB-LabVIEW. The other variables that are unchanged during a test condition are recorded manually through monitors of temperature controllers and mass flow controllers.

4.1.2 Human Machine Interface

HMI was designed for easily monitoring variables changing during a test condition and saving data including back pressure, solenoid status, cell output current, and voltage with adjustable plotting time and sampling rate illustrated in **Figure 4.3**. Additionally, the electronic load is connected with LabVIEW through a USB port allowing users to control the load of fuel cell through HMI, detailed LabVIEW code in **Appendix B**.



Figure 4.3 LabVIEW HMI of the test system

4.1.3 Operating range and accuracy

The test system was constructed of many components whose capabilities limit the operating ranges of the test system as shown in **Table 4.1**. Due to the operating range of parameters discussed in Section 3.2.1, the operating ranges of OT, RH, cathode flow rate, and electronic load are not the limitations for PEMFC tests. However, the operating ranges of the COP, anode flow rate, and purge duration are determined by the pressure sensor, hydrogen mass flow controller, and solenoid valve, respectively. The maximum pressure of the sensor is 1 MPa and the pressure drop through the cell is 0.1 MPa, which means the maximum COP is 5.5 MPa.

Table 4.1 Specifications of the self-designed PEMFC test system

Parameter	Rated range	Resolution	Accuracy /Response time
OT	0 - 400 °C	0.1 °C	±0.5 %FS
RH	0 - 100 %	0.3 % (due to temp controller resolution)	N/A
COP	0 - 80 psi (5.5 bar)	0.001 psi	±1% F.S
Anode flow rate	0 - 500 sccm	0.001 sccm /150 ms	± (0.5%RD ± 0.2%FS)
Cathode flow rate	0 - 20,000 sccm	0.01 sccm /150 ms	± (0.5%RD ± 0.2%FS)
Electronic load	Constant Voltage: 120V	0.0001 V	Readback Voltage: ± (0.025% + 0.025%FS)
	Constant Current: 30A	0.0001 A	Readback Current: ± (0.05% + 0.05%FS)
	Constant Power: 150W	0.0001 W	Readback Power: ± (0.1% + 0.1%FS)
Purge duration at cathode side	≥ 200 ms	200 ms	≤ 50 ms

4.2 TWO-PARAMETER TEST RESULTS

This research began by exploring the effect of two operating parameters, OT and RH on PEMFC performance [64], see **Appendix D**. Nine experimental test cases were conducted as detailed in **Table 4.2**. The analysis considered both the individual and combined effects of these parameters.

Table 4.2 Nine test cases of two-parameters test

Test number	Operating Temperature (°C)	Relative Humidity (%)
1	60	50
2	60	60
3	60	70
4	70	50
5	70	60
6	70	70
7	80	50
8	80	60
9	80	70

To better understand the impact of OT and RH, the current density was categorized into three distinct ranges: low (0-0.05 A/cm²), medium (0.05-0.3 A/cm²), and high (0.3-0.4 A/cm²). This allowed for a more granular examination of how these parameters affect PEMFC performance at different operating current levels.

4.2.1 Effect of OT at RH 50%

The effect of operating temperature on PEMFC performance under a low RH of 50% was illustrated through polarization and power curves, as depicted in **Figure 4.4**. It was evident that OT had minimal effect on PEMFC performance at low current density, whereas its influence became more pronounced at medium current density and particularly dramatic at high current density.

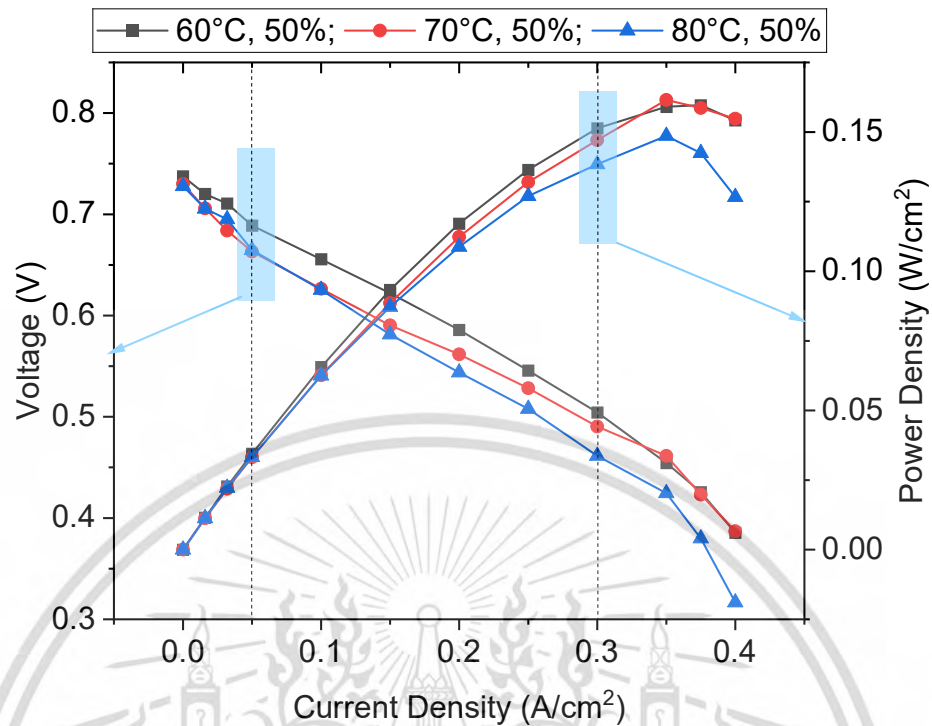


Figure 4.4 Effect of OT at RH 50%

Within the low and medium current density ranges, 60°C delivers superior performance compared to 70°C and 80°C. This is reflected in higher cell output voltages. However, at high current density, 70°C notably improved PEMFC performance, with both 60°C and 70°C yielding superior outputs compared to 80°C. Specifically, the peak power density was achieved at 70°C, recording 0.16153 W/cm² and 0.4615 V. Conversely, at 0.4 A/cm², the higher OT of 80°C resulted in the poorest PEMFC performance with 0.12668 A/cm² at 0.3167 V.

Overall, at low RH 50%, increasing OTs negatively impacted cell performance under low RH of 50%, especially high OT 80°C led to a significant decline in cell potential at high current density.

4.2.2 Effect of OT at RH 60%

Figure 4.5 shows the effect of OT on PEMFC performance at medium RH 60% using polarization and power curves. The results reveal a distinct variation in performance across the current density range.

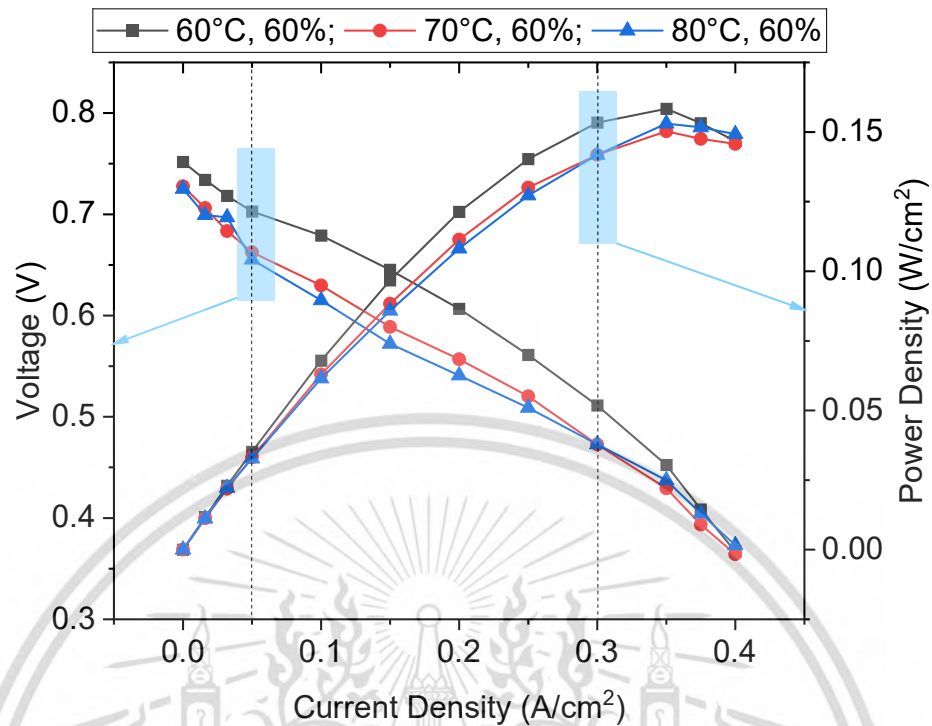


Figure 4.5 Effect of OT at RH 60%

It became apparent that varying OTs had a significant impact on PEMFC performance across low and medium current density ranges. However, the effect of OT became less distinct at high current density, resulting in the convergence of cell potentials.

Throughout the low and medium current density ranges, an increase in OT resulted in decreased PEMFC outputs, with 60°C demonstrating superior performance compared to 70°C and 80°C.

Conversely, at high current density, while 80°C appeared to slightly enhance PEMFC performance, 60°C continued to yield superior outputs, with its peak power density recorded at 0.35 A/cm² reaching 0.15834 W/cm² and 0.4524 V. Notably, at 0.4 A/cm², the impact of OT on PEMFC performance was minimal, resulting in similar performance across different temperatures.

Overall, raising OT from (60°C to 70°C or 80°C) at RH 60% led to a significant drop of cell performance. While high OT 80°C performed the worst cell potential across low and medium current density ranges, its trendline showed improvement at high current density.

4.2.3 Effect of OT at RH 70%

The effects of various OTs on PEMFC performance at a high RH of 70% are depicted in **Figure 4.6**.

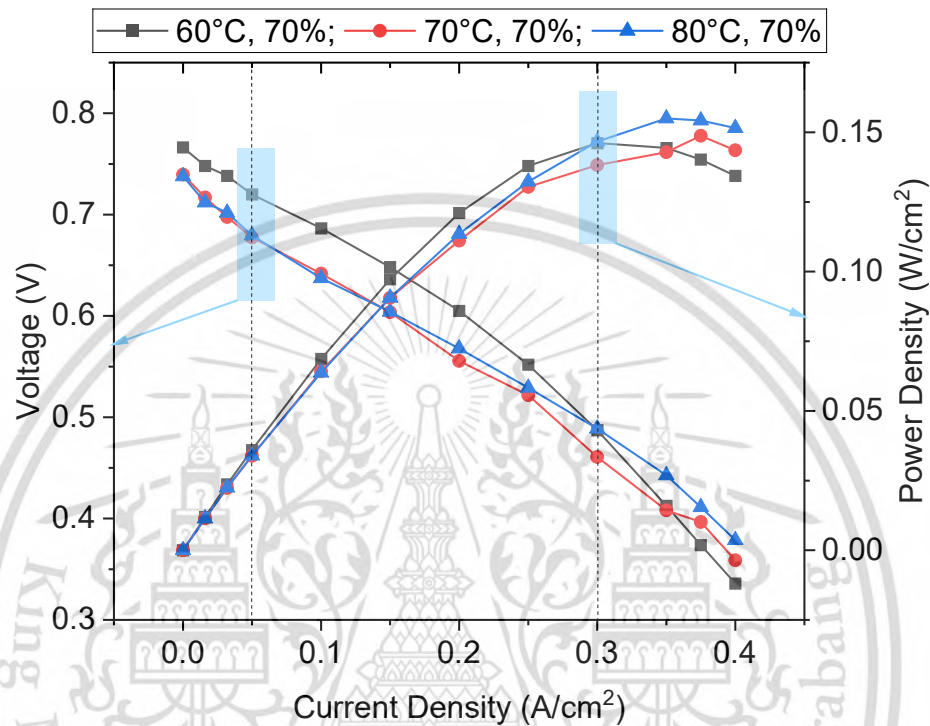


Figure 4.6 Effect of OT at RH 70%

Across low and medium current density ranges, the PEM fuel cell exhibited its optimal and poorest performances at 60°C and 70°C, respectively, with 60°C consistently outperforming the other temperatures. However, at high current density ranges, the performance of the cell at 60°C deteriorated significantly, leading to a notable decrease in cell outputs, with the lowest point recorded at 0.4 A/cm², achieving 0.13436 W/cm² and 0.3359 V.

In contrast, at 80°C, the cell initially exhibited poor performance at low current density, followed by a gradual improvement at medium current density, and a significant enhancement at high current density. The peak power density was recorded at 0.35 A/cm², reaching 0.15495 W/cm² and 0.4427 V.

Overall, at high RH of 70%, increasing OT resulted in cell outputs drop under low and medium current density ranges. However, at high current density, it led to an

increase of PEMFC performance. Especially, 80°C showed favorable conditions at this range.

4.2.4 Effect of RH at OT 60°C

The impact of varying RHs of 50%, 60%, and 70% on PEMFC performance under a constant OT of 60°C is illustrated in **Figure 4.7**. An elevation in RH resulted in an increase and decrease in PEMFC performance at low and high current densities, respectively.

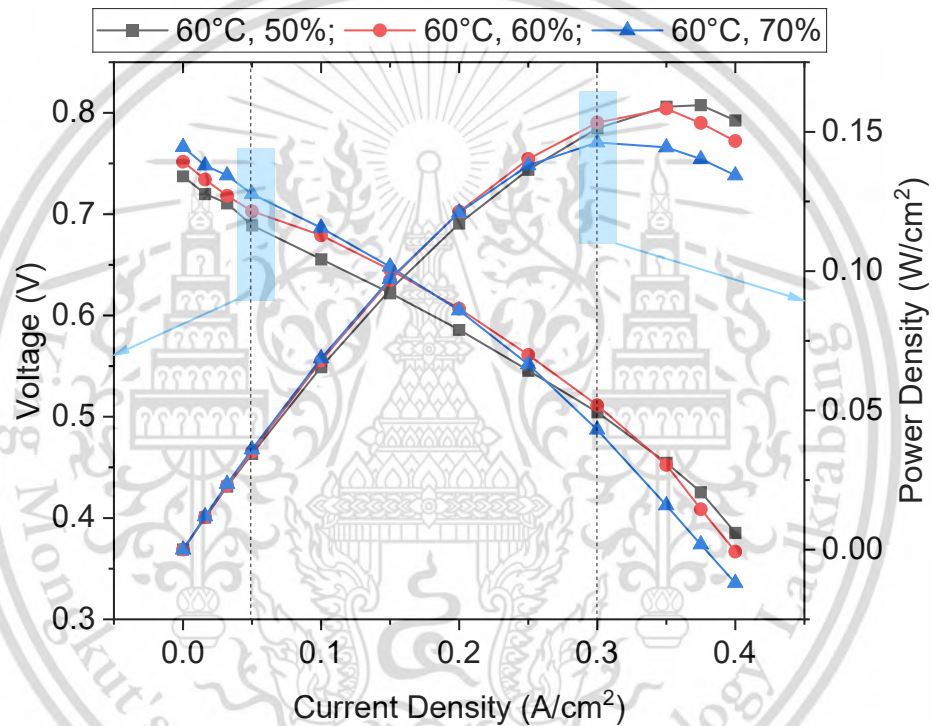


Figure 4.7 Effect of RH at OT 60°C

At RH 50% and 60%, the cell exhibited favorable outputs at low current density, followed by a decline at medium current density and the poorest performance at high current density. The lowest point of the cell's outputs was observed at RH 70% and high current density of 0.4 A/cm², registering 0.13436 W/cm² and 0.3359 V.

Contrariwise, RH 50% exhibited the poorest PEMFC performance at low and medium current densities. However, its outputs significantly increased at high current density ranges, with the peak power density reached at 0.375 A/cm², recording 0.15964 W/cm² and 0.4257 V.

Overall, under low OT of 60°C, increasing RH had positive and negative impacts on PEMFC performance at low-medium current density and high current density range, respectively. Remarkably, the low RH 50% was preferable at high current density.

4.2.5 Effect of RH at OT 70°C

Figure 4.8 illustrates the impact of RH on PEMFC performance at a medium OT of 70°C. The results revealed minimal effects of varying RH on PEMFC performance under low and medium current densities, with their influence becoming more pronounced at high current density.

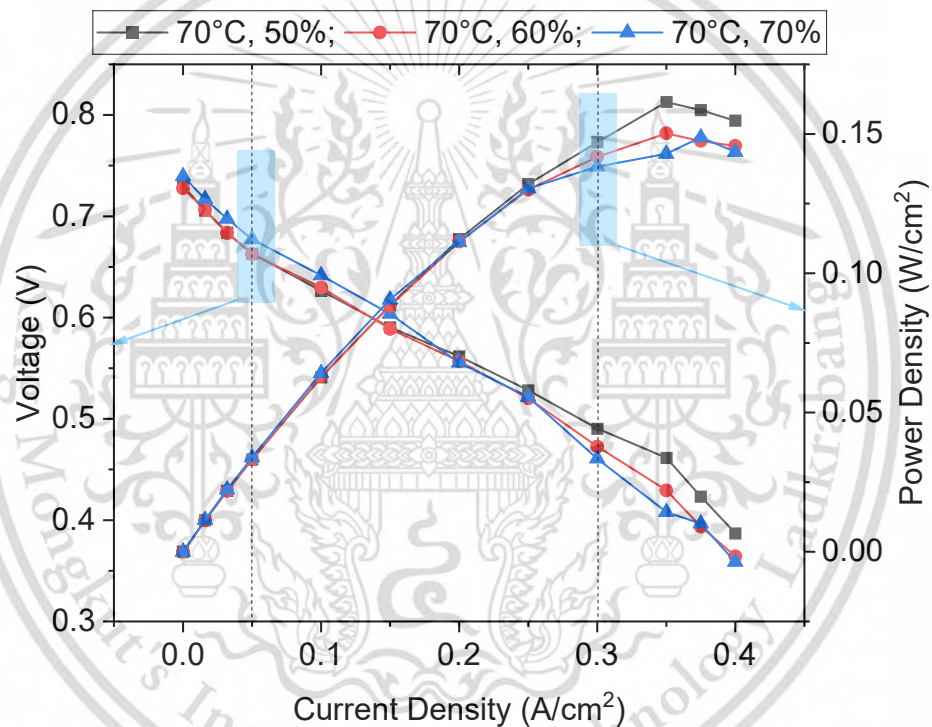


Figure 4.8 Effect of RH at OT 70°C

Under medium OT 70°C, an increase in RH led to improvements and declines in PEMFC performance at low and high current densities, respectively. However, their effects were less discernible at low and medium current densities. High RH appeared to be optimal at low current density but detrimental at high current density. Opposite, low RH of 50% exhibited similar performance to RH 60% at low current density and performed poorly. However, at medium current density, RH 50% showcased an improvement over RH 60%, ultimately demonstrating optimal performance at high

current density, with the peak power density achieved at 0.35 A/cm^2 , registering 0.16153 W/cm^2 and 0.4615 V .

In summary, at an OT of 70°C , the influence of RH is negligible at low and medium current densities. However, an increase in RH resulted in a decrease in PEMFC performance at high current density ranges.

4.2.6 Effect of RH at OT 80°C

Figure 4.9 illustrates the impact of RH on PEMFC performance at a high OT of 80°C . The results indicated that the effects of varying OTs at 80°C were relatively consistent.

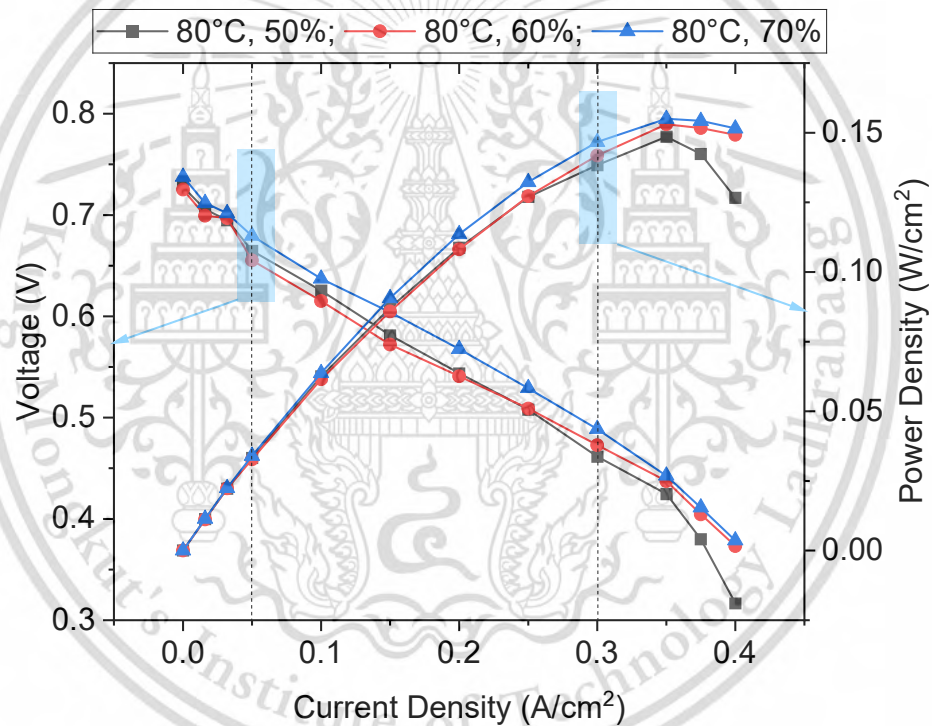


Figure 4.9 Effect of RH at OT 80°C

It is evident that an increase in RH at high current density resulted in enhanced cell outputs. Specifically, high RH of 70% exhibited favorable conditions at OT 80°C , reaching its peak at 0.35 A/cm^2 with 0.15495 W/cm^2 and 0.4427 V .

During low and medium current density operations, RH of 60% yielded subpar PEMFC outputs, but showed improvement at higher ranges, while RH of 50%

significantly compromised cell performance, reaching its lowest point of power density at 0.4 A/cm^2 with 0.12668 W/cm^2 and 0.3167 V .

Overall, at a high OT of 80°C , higher RH proved beneficial for PEMFC performance, particularly at high current density ranges. Among the different RH levels tested, a RH of 70% emerged as the optimal condition for this scenario.

4.2.7 Polarization and power density curves

Taking all individual tests into account, nine polarization curves and power density curves were illustrated in Figure 4.10 and Figure 4.11, respectively.

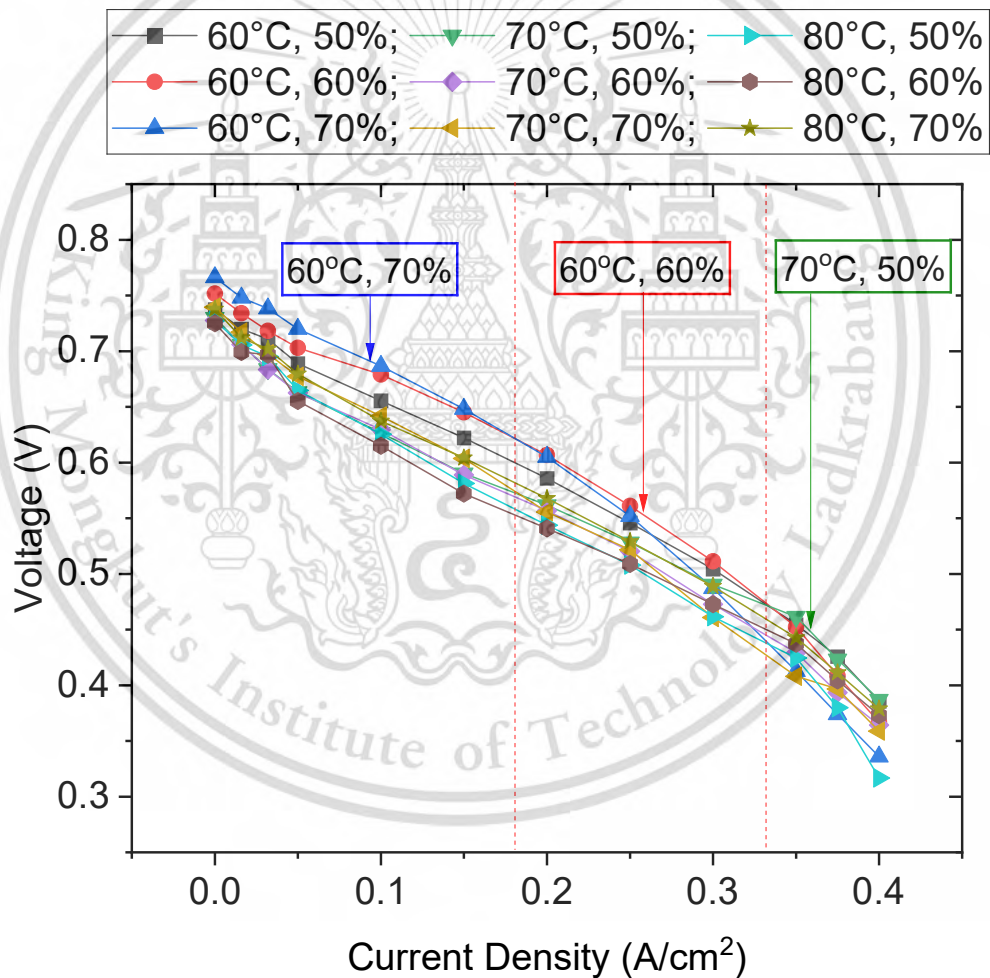


Figure 4.10 Polarization curves of two parameters test

Figure 4.10 demonstrates that cell voltage performance depends on OT, RH, and current density. At low and medium current densities ($0\text{-}0.18 \text{ A/cm}^2$), the

combination of OT 60°C and RH 70% yielded the highest output voltage. This trend shifted to OT 60°C and RH 60% at medium to high current densities (0.18-0.33 A/cm²). Interestingly, OT 70°C and RH 50% achieved the highest voltage at the highest current density range (0.33-0.4 A/cm²). This suggests that reducing RH from 70% to 50% improves voltage output as current density increases from 0 to 0.4 A/cm². Additionally, OT 60°C appears favorable for low and medium current densities, while OT 70°C becomes more optimal at high current densities. Notably, the combinations of OT 60°C and RH 70%, and OT 80°C and RH 50% resulted in significant voltage drops at high current densities, indicating these conditions are unfavorable for cell performance.

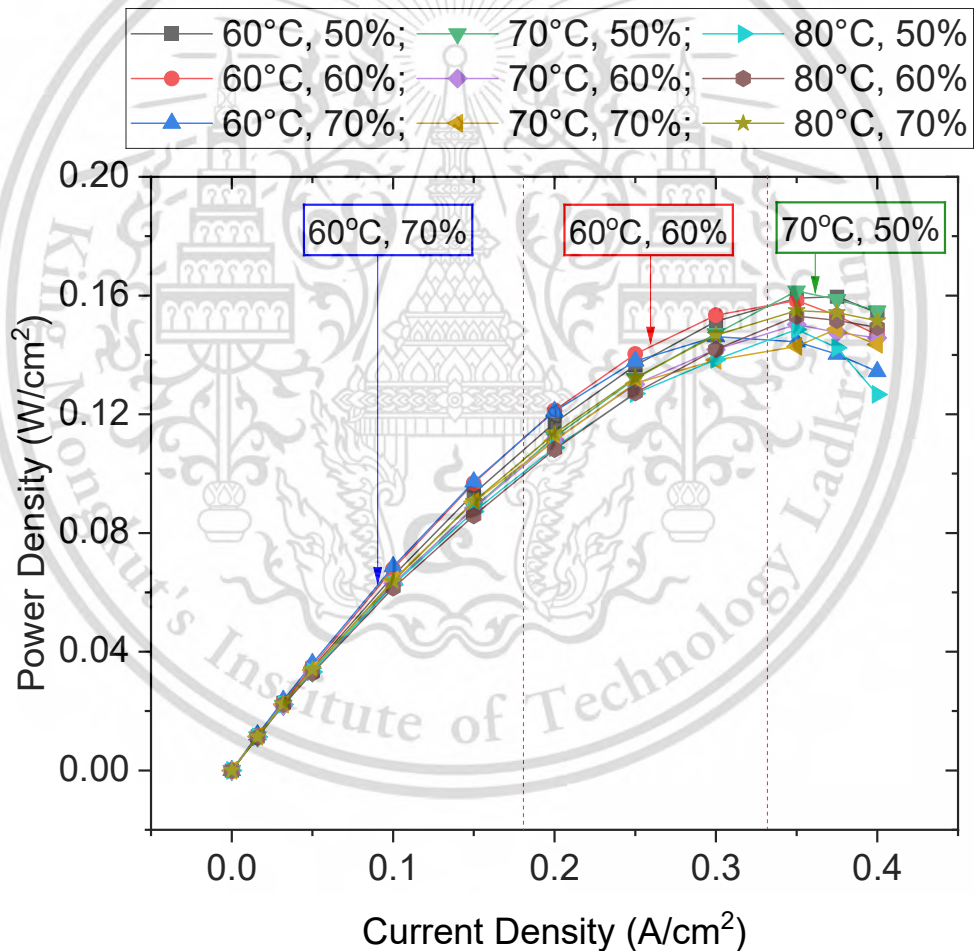


Figure 4.11 Power density curves of two parameters test

While power densities were low at low current densities and showed minimal variations across test conditions, they became more pronounced at medium current densities and significant at high current densities, as demonstrated in **Figure 4.11**. The peak power densities were generally observed around 0.35-0.375 A/cm². Aligning with the voltage trends, the maximum power densities were recorded at OT 60°C and RH 70% (0-0.18 A/cm²), OT 60°C and RH 60% (0.18-0.33 A/cm²), and OT 70°C and RH 50% (0.33-0.4 A/cm²) based on the polarization curves. Furthermore, the combinations of OT 60°C and RH 70%, and OT 80°C and RH 50% resulted in the lowest overall power densities, likely due to the detrimental effects of excessively high OT or RH on PEMFC performance.

4.2.8 Range analysis

The experiments were conducted across a range of current densities to assess the influence of OT and RH on overall PEMFC performance. Utilizing the range analysis method, the impact of OT and RH on PEMFC power was quantified under varying current densities, as illustrated in **Figure 4.12** and **Table 4.3**.

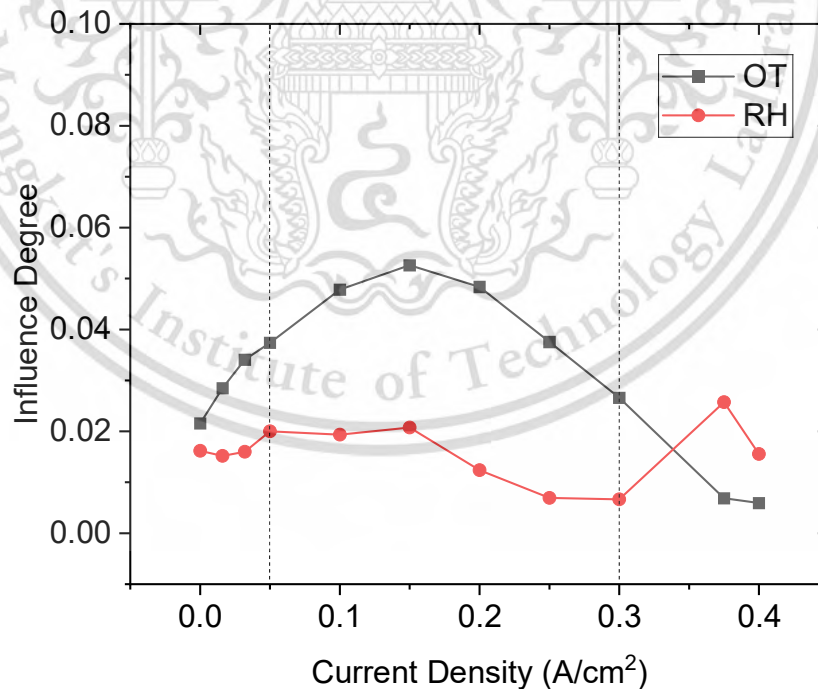


Figure 4.12 Influence Degree of OT and RH

Table 4.3. illustrated the peaks and troughs impact of OT and RH on PEMFC performance.

Table 4.3 Peaks and troughs of OT and RH influence degrees

Parameter	OT		RH	
	Peak	Trough	Peak	Trough
Influence Degree	0.0688	0.0037	0.0866	0.0143
Current Density (A/cm ²)	0.04	0.35	0.25	0.3

At low and medium current densities (up to 0.3 A/cm²), OT has a significantly stronger influence on PEMFC performance compared to RH. This is evident in the 2-2.5 times greater influence degree of OT observed in these ranges. Furthermore, the influence of OT reaches a peak at 0.15 A/cm² shown in **Table 4.3**, highlighting its dominant role at medium current densities. Conversely, RH has a minimal impact on performance at these lower current densities.

However, this trend shifts as the current density approaches the peak power output (around 0.35 A/cm²). Here, the contributions of OT and RH become more balanced. While an increase in OT still proportionally improves cell performance at this stage, the influence of RH becomes more prominent. Beyond this point (high current densities exceeding 0.35 A/cm²), the roles of OT and RH appear to reverse. The influence degree of OT drops dramatically, while the impact of RH triples. This surge in RH's influence likely leads to flooding within the cell at high current densities, as evidenced by the significant power density drop observed in **Figure 4.11** around the 0.375-0.4 A/cm² range.

4.3 FOUR-PARAMETER TEST RESULTS

According to the Orthogonal method, nine test cases were designed to investigate the effects of four operating parameters on PEMFC performance as shown in **Table 4.4**.

Table 4.4 Nine test cases of four-parameter test

Test number	OT (°C)	RH (%)	COP (psi)	ASR
1	60	50	8	1.8
2	60	60	15	2.4
3	60	70	22	3
4	70	50	15	3
5	70	60	22	1.8
6	70	70	8	2.4
7	80	50	22	2.4
8	80	60	8	3
9	80	70	15	1.8

In the four-parameter test set, current density was divided into three ranges including low current density (0-0.05 A/cm²), medium current density (0.05-0.3 A/cm²), and high current density (0.3-0.45 A/cm²) to observe the different impacts of four operating parameters on PEMFC performance.

4.3.1 Polarization curves

Figure 4.13 showcases the diverse polarization curves resulting from various operating conditions. The test results were categorized into three groups based on their similarities as shown in **Table 4.5**: group 1 (tests 1, 5, and 7), group 2 (tests 2, 3, and 4), and group 3 (tests 6, 8, and 9).

Overall, group 1 exhibited the highest cell output voltages across the entire current density range, followed by group 2 and then group 3. Specifically, the highest voltages were recorded at test 5 from 0-0.25 A/cm², test 1 from 0.25-0.37 A/cm², and test 7 from 0.37-0.45 A/cm². Interestingly, group 2 initially resembled group 1 at low current densities, but diverged at medium densities, eventually converging with group 3 at high densities.

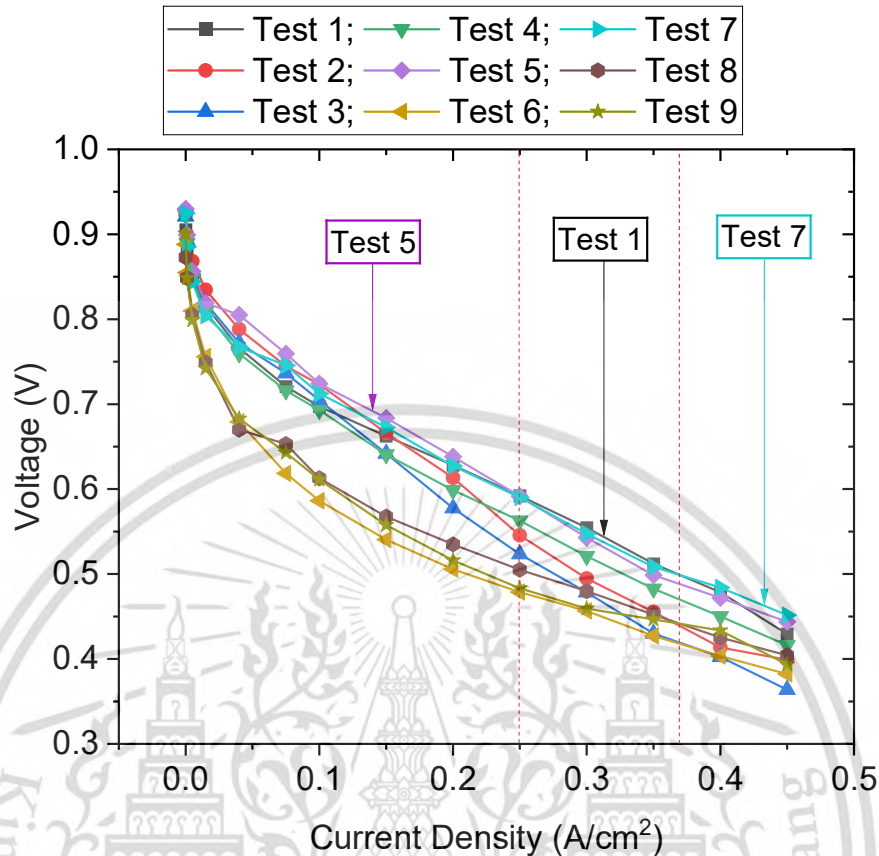


Figure 4.13 Polarization curves of four parameters test

At low current densities, both group 1 and group 2 displayed minimal polarization losses, evident by their similar, shallow slopes in the polarization curves compared to group 3. This suggests better activation behavior in these groups.

At medium current density, the trendlines of group 2 exhibited an incremental increase in slopes, indicating higher Ohmic losses. Particularly, the visible reduction in voltages at 0.3 A/cm² varies from test 1 (0.5546 V) to test 7 (0.5474 V), test 5 (0.5428 V), test 4 (0.5211 V), test 2 (0.4948 V), test 8 (0.4798 V), test 3 (0.4786 V), test 9 (0.4592 V), and test 6 (0.4565 V).

Moving to high current density ranges, Group 1 consistently achieved superior output voltages compared to Groups 2 and 3. At the highest current density (0.45 A/cm²), the mean cell output voltage decreased sequentially across tests starting from test 7 (0.4516 V) to test 5 (0.4438 V), test 1 (0.4293 V), test 4 (0.4160 V), test 8 (0.4042 V), test 2 (0.3991 V), test 9 (0.3936 V), test 6 (0.3821 V), and then test 3 (0.3637 V) recording the lowest voltage.

Table 4.5 Groups of orthogonal test results

Group	Test number	OT (°C)	RH (%)	COP (psi)	ASR
1	1	60	50	8	1.8
	5	70	60	22	1.8
	7	80	50	22	2.4
2	2	60	60	15	2.4
	3	60	70	22	3
	4	70	50	15	3
3	6	70	70	8	2.4
	8	80	60	8	3
	9	80	70	15	1.8

In summary, Group 1 exhibited favorable working conditions with higher output voltages than Groups 2 and 3, with Test 7 identified as the optimal operating condition due to its superior peak voltage at the highest current density compared to other tests.

4.3.2 Power density curves

The nine power density curves corresponding to nine test cases were drawn and shown in **Figure 4.14**. As divided in **Table 4.5**, the power density trendlines of group 1 performed superior output voltages to group 3. In accordance with the favorable voltages defined in **Figure 4.13**, the highest power densities were recorded at test 5 from 0-0.25 A/cm², test 1 from 0.25-0.37 A/cm², and test 7 from 0.37-0.45 A/cm². Group 2 trendlines seem like group 1 at low current density range, then they diverge from group 1 at medium current density and converge with group 3 at high current density.

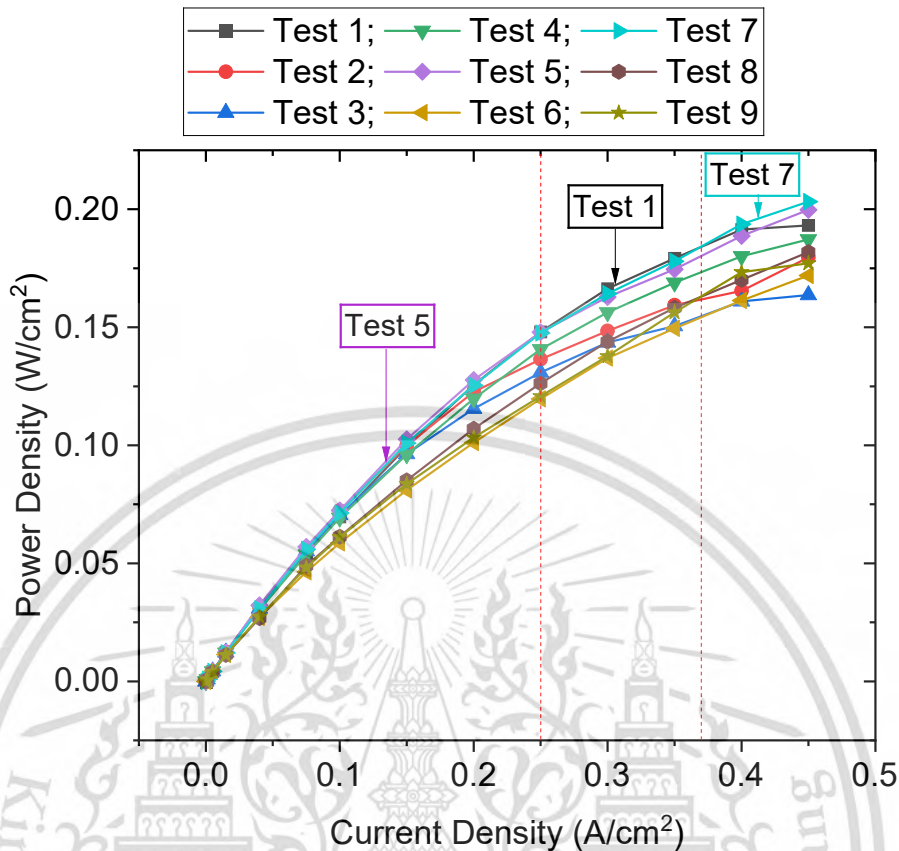


Figure 4.14 Power density curves of four parameters test

In the medium range of current density, group 2 exhibits a gradual decrease in trendlines, albeit still maintaining higher values compared to group 3. There is a discernible reduction in power density across various tests within this range. For instance, at 0.3 A/cm^2 the observed power densities vary from test 1 (0.1664 W/cm^2) to test 7 (0.1642 W/cm^2), test 5 (0.1629 W/cm^2), test 4 (0.1564 W/cm^2), test 2 (0.1484 W/cm^2), test 8 (0.1440 W/cm^2), test 3 (0.1436 W/cm^2), test 9 (0.1378 W/cm^2), and test 6 (0.1370 W/cm^2).

Conversely, at higher current density levels, Group 1 consistently demonstrates superior performance in terms of current densities compared to groups 2 and 3. This discrepancy becomes particularly evident at 0.45 W/cm^2 , the mean cell current density decreases sequentially from test 7 (0.2032 W/cm^2) to test 5 (0.1997 W/cm^2), test 1 (0.1932 W/cm^2), test 4 (0.1872 W/cm^2), test 8 (0.1819 W/cm^2), test 2 (0.1796 W/cm^2), test 9 (0.1771 W/cm^2), test 6 (0.1720 W/cm^2), and test 3 (0.1637 W/cm^2).

Overall, group 1 exhibits consistently higher current densities compared to group 2 and group 3, indicating more favorable operating conditions. Remarkably, test 7 within group 1 stands out as the optimal operating point due to its superior peak power output.

4.3.3 Influence Degree

Figure 4.15 illustrates how the influence of four operating parameters on PEMFC performance changes with increasing current density.

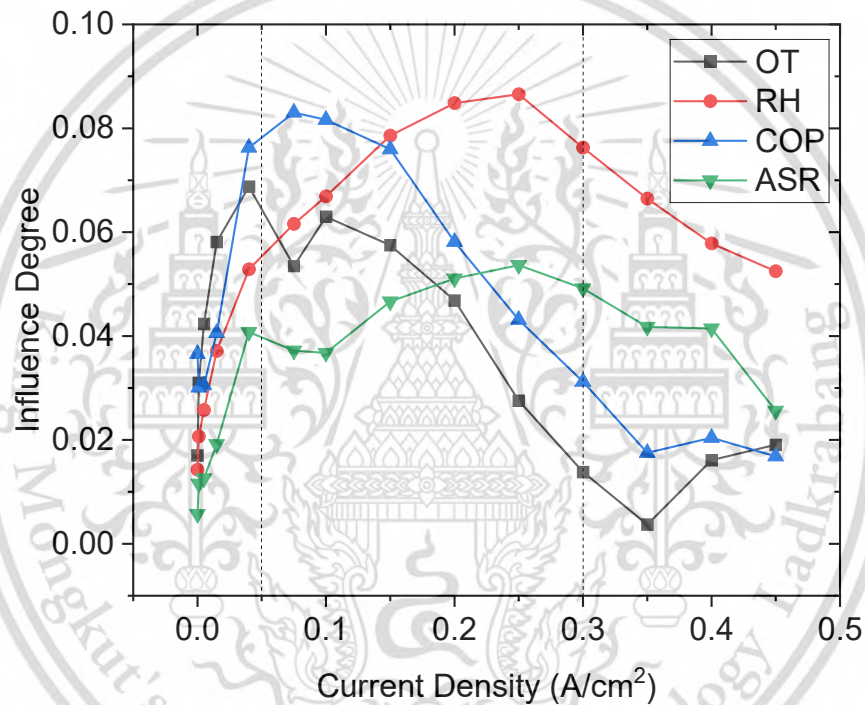


Figure 4.15 Influence degree of four parameters

At low current densities (0-0.05 A/cm²), OT and COP have the most significant impact on performance, while RH and ASR play a lesser role. This trend shifts at medium current densities (0.05-0.3 A/cm²), where COP and RH become the dominant factors affecting performance. Finally, at high current densities (0.3-0.45 A/cm²), RH and ASR exert the greatest influence.

Table 4.6 quantifies these observations. It shows that OT has the most significant impact at very low current densities (0-0.04 A/cm²), followed by COP (0.04-0.15 A/cm²) and then RH (0.15-0.45 A/cm²). Conversely, ASR has the least influence

across the entire low to medium current density range (0-0.2 A/cm²), with OT's impact diminishing at higher current densities (0.2-0.45 A/cm²).

Table 4.6 Minimum and maximum influence degrees of four operating parameters

Parameter	OT		RH		COP		ASR	
	Peak	Trough	Peak	Trough	Peak	Trough	Peak	Trough
Influence Degree	0.0688	0.0037	0.0866	0.0143	0.0830	0.0168	0.0537	0.0057
Current Density (A/cm ²)	0.04	0.35	0.25	0	0.075	0.45	0.25	0

At the peak power density of 0.45 A/cm², the influence degree of operating parameters follows the order: RH (0.05248) > ASR (0.02561) > OT (0.01906) > COP (0.01682). This translates to RH having roughly 2.01 times the impact of ASR, 2.75 times the impact of OT, and 3.12 times the impact of COP. This emphasizes the critical role of RH in PEMFC performance at high power densities. Here, water accumulation within the cell leads to flooding, where water covers the catalyst reaction surface, particularly on the cathode side. Consequently, purging droplets at the cathode becomes crucial to prevent flooding and maintain performance at high current densities.

4.3.4 Effect of OT

The effect of OT was again investigated by changing its value of the optimal condition (test 7) achieved from orthogonal tests. **Figure 4.16** reveals a non-proportional relationship between OT and the cell's output voltage and power density.

The cell exhibited distinct voltage outputs across the three OT levels tested (60 °C, 70 °C, and 80 °C). The highest voltage occurred at 80 °C, with a drop followed by a rise when increasing OT from 60 °C to 70 °C and 80 °C, respectively.

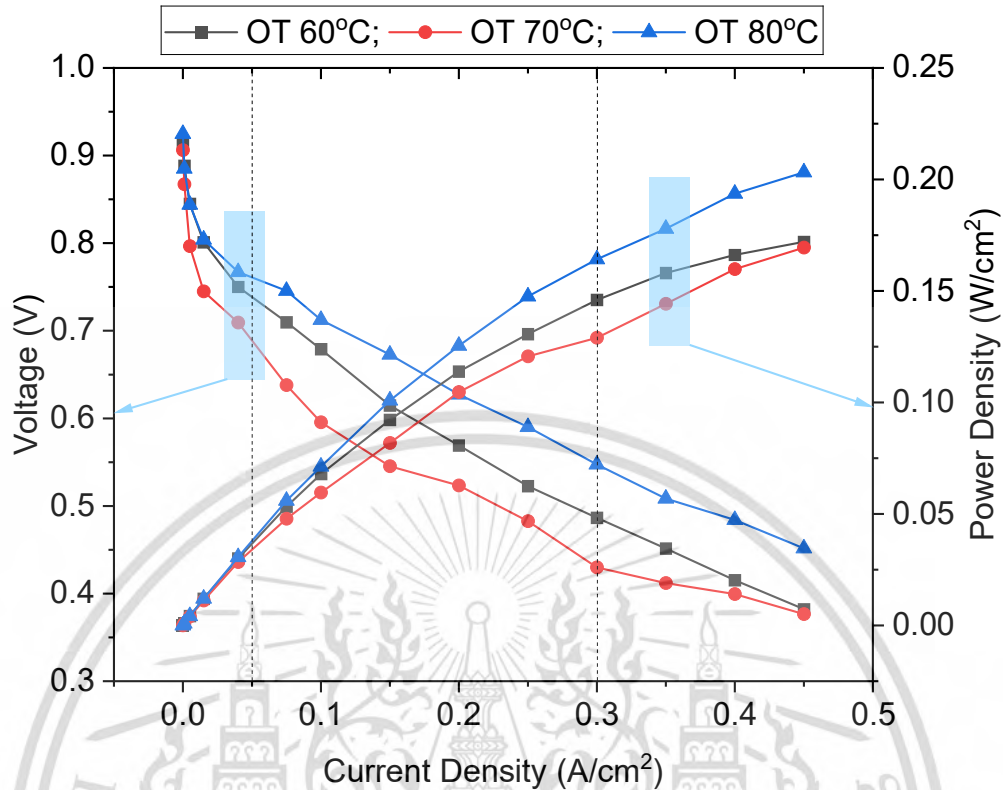


Figure 4.16 Effect of OT at RH 50%, OP 22psi, and ASR 2.4

At low and medium current densities, the cell's performance at 70 °C appeared intermediate between the results at 60 °C and 80 °C. However, at high current densities, 80 °C emerged as the optimal operating temperature, leading to significantly higher voltage and power density compared to 60 °C and 70 °C. Additionally, the output trendline at 70 °C appears to converge with the trendline at 60 °C as current density increases.

Quantitatively, at a medium current density of 0.3 A/cm², the cell's outputs at 80 °C (0.16421 W/cm² and 0.54735 V) were 12.53% and 27.31% higher than those at 60 °C (0.14592 W/cm² and 0.48639 V) and 70 °C (0.12898 W/cm² and 0.42994 V), respectively.

Similarly, at the highest current density of 0.45 A/cm², an OT of 80°C resulted in the peak cell outputs of 0.20322 W/cm² achieved at 0.45159 V of cell potential. These values were 18.15% and 19.93% higher than those recorded at 60°C (0.1720 W/cm² with 0.38222 V) and 70°C (0.16944 W/cm² with 0.37653 V), respectively. Which

indicates that the cell outputs at 60 °C and 70 °C show minimal difference at this highest current density.

Overall, the results of the orthogonal test align with the individual evaluation of OT's effect on PEMFC performance, confirming that the optimal OT remains at 80°C.

4.3.5 Effect of RH

This investigation examined the influence of RH on PEMFC performance at the optimal operating condition identified through orthogonal testing (OT 80 °C, COP 22 psi, and ASR 2.4). The RH was varied between 50%, 60%, and 70%, as shown in **Figure 4.17**.

The cell exhibited a clear dependence on RH, achieving the highest voltage and power density at 50% RH. Increasing RH to 60% and 70% resulted in a significant drop in both voltage and power density.

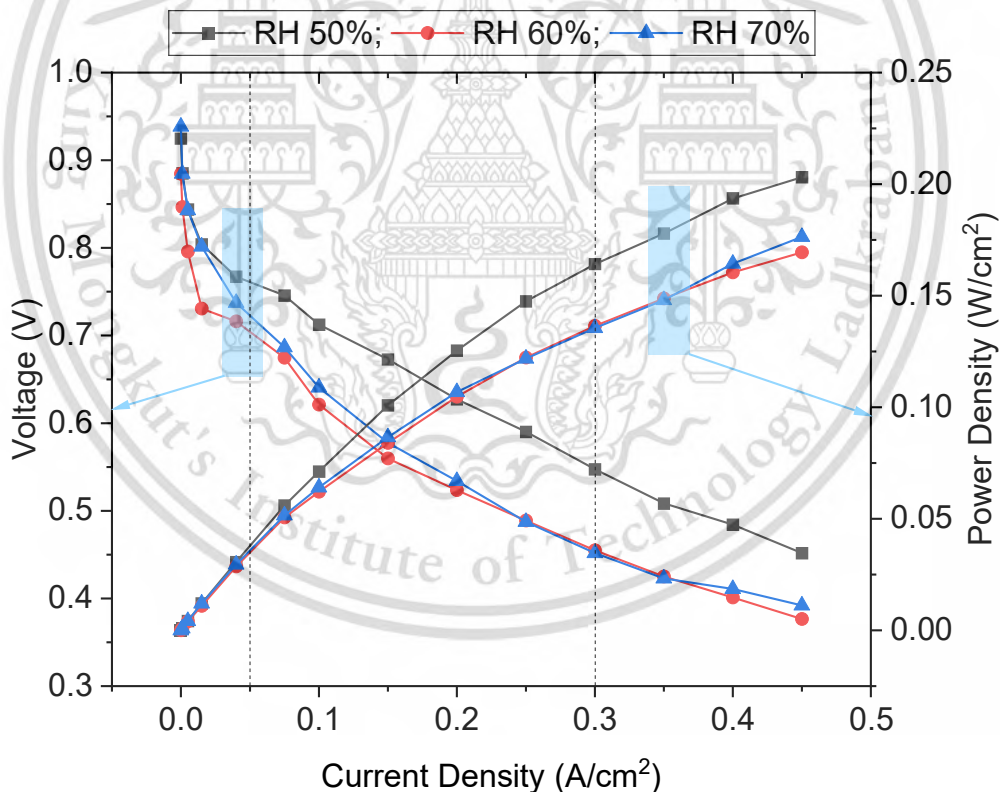


Figure 4.17 Effect of RH at OT 80°C, COP 22psi, and ASR 2.4

At low current densities, the cell's outputs at 50% and 70% RH appeared similar and considerably higher than the output at 60% RH. This trend continued at medium

and high current densities, with 50% RH offering the most favorable operating condition due to its significantly superior voltage and power density compared to 60% and 70% RH. Interestingly, minimal differences were observed between the cell's outputs at 60% and 70% RH within these medium and high current density ranges.

At a medium current density of 0.3 A/cm^2 , the cell outputs at RH 50% (0.16421 W/cm^2 and 0.54735 V) were 20.33% and 21.17% higher than at 60% (0.13646 W/cm^2 and 0.45486 V) and 70% (0.13551 W/cm^2 0.45172 V), respectively.

Following the trend, at the peak current density of 0.45 A/cm^2 , 50% RH yielded the highest cell outputs: 0.20322 W/cm^2 achieved at a cell potential of 0.45159 V . These values are 15.20% and 19.95% greater than those obtained at 70% RH (0.1764 W/cm^2 with 0.392 V) and 60% RH (0.16942 W/cm^2 with 0.37649 V), respectively.

General, the individual evaluation of RH's effect on PEMFC performance aligns with the findings from the orthogonal test. Both analyses demonstrate that 50% RH remains the optimal operating condition for this cell.

4.3.6 Effect of COP at the cathode side

By varying the COP value (8 psi, 15 psi, and 22 psi) at the optimal condition derived from the orthogonal test, the individual effect of COP on PEMFC performance was assessed and depicted in **Figure 4.18**.

The cell exhibited distinct output voltages at three COP levels, with the highest voltage recorded at 22 psi and the lowest at 8 psi. Notably, as COP increased from 8 psi to 22 psi, both cell potential and power density significantly improved across all current density ranges.

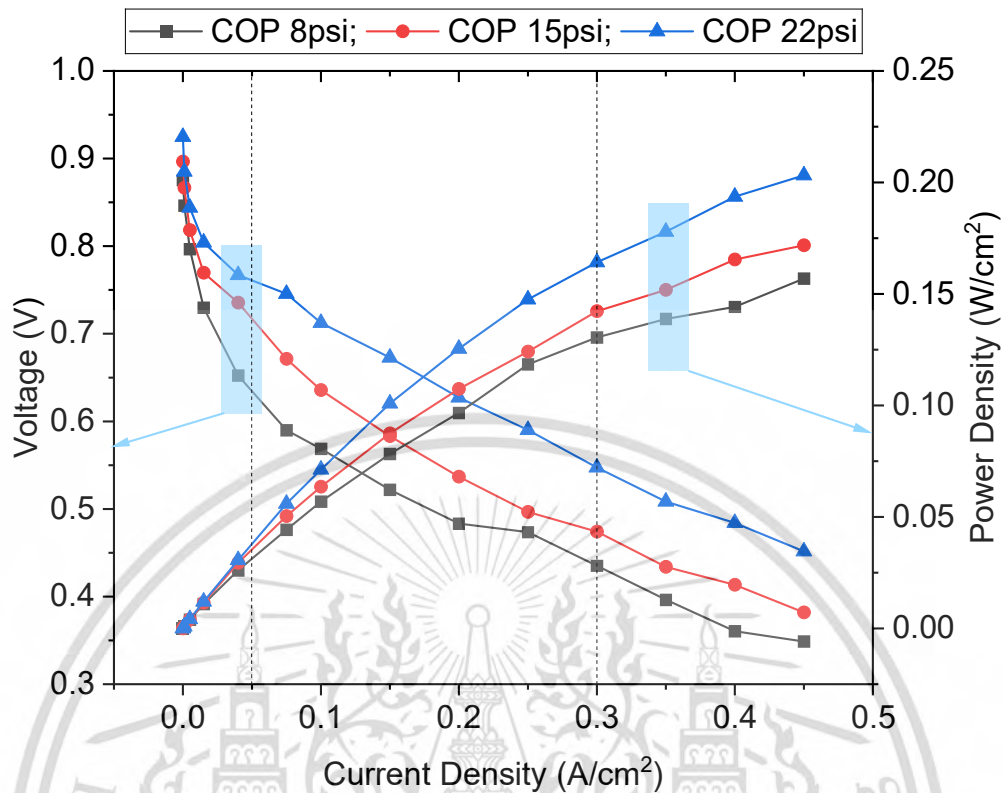


Figure 4.18 Effect of COP at OT 80°C, RH 50%, and ASR 2.4

Within the low current density ranges, the cell outputs at 15 psi appeared to approximate the average of those at 8 psi and 22 psi. However, at medium and high current density ranges, COP of 22 psi gradually emerged as the superior operating pressure, resulting in significantly higher voltage and power density compared to 8 psi and 15 psi. Moreover, output trendlines at 15 psi exhibited a convergence towards those at 8 psi.

At a medium current density of 0.3 A/cm², the cell outputs at COP 22 psi (0.16421 W/cm² and 0.54735 V) were 15.46% and 25.80% higher than those at 15 psi (0.14221 W/cm² and 0.47405 V) and 8 psi (0.13053 W/cm² and 0.43511 V), respectively.

Similarly, at the highest current density of 0.45 A/cm², a COP of 22 psi yielded peak cell outputs of 0.20322 W/cm² achieved at 0.45159 V of cell potential. These values were 18.27% and 29.53% higher than those recorded at 15 psi (0.17182 W/cm² with 0.38182 V) and 8 psi (0.15688 W/cm² with 0.34863 V), respectively.

In conclusion, similar to the observation from the orthogonal test, the individual evaluation of COP's effect on PEMFC performance confirms that 22 psi remains the optimal operating pressure for this cell.

4.3.7 Effect of ASR

The individual effect of ASR was examined by altering its value at the optimal condition obtained from the orthogonal test, as illustrated in **Figure 4.19**.

The cell performed varying output voltages at three ASR levels with the highest voltage recorded at ASR 2.4 and the lowest at ASR 1.8. When the ASR increased from 1.8 to 2.4 and then to 3.0, the cell potential initially rose before declining at ASR 3.0.

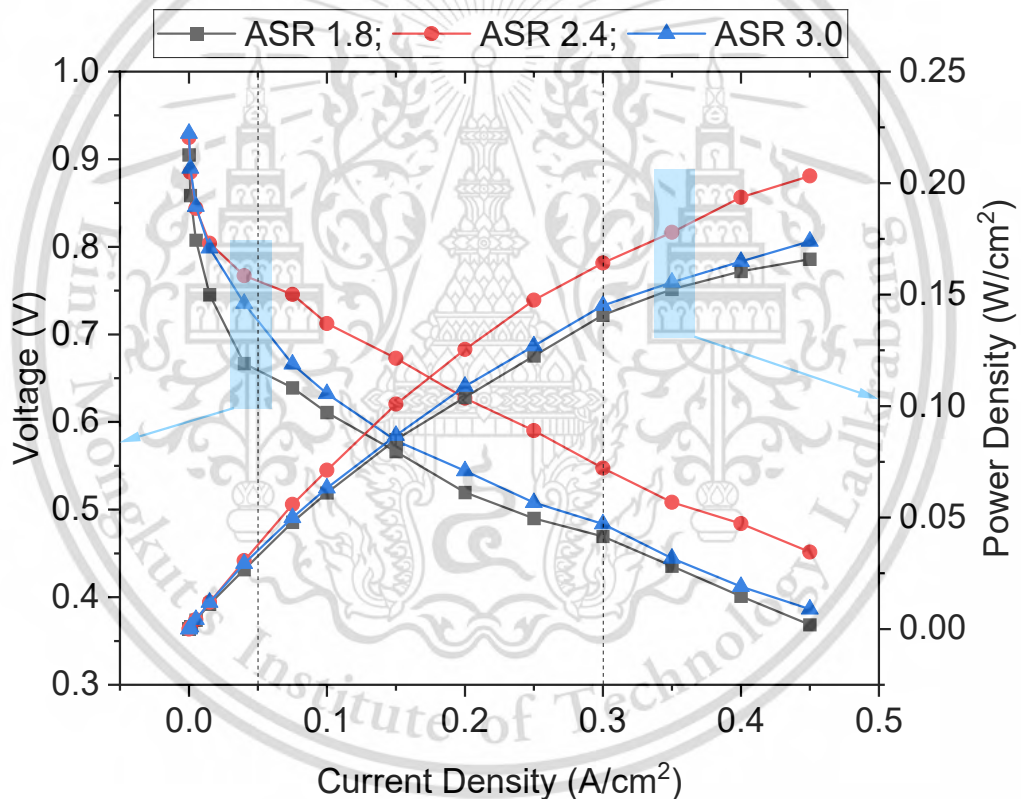


Figure 4.19 Effect of ASR at OT 80°C, RH 50%, and COP 22psi

At the low current density range, the cell outputs at ASR 2.4 and 3.0 appeared similar and notably higher than those at ASR 1.8. However, at medium and high current density, ASR 2.4 provided the optimal working condition, resulting in significantly higher voltage and power density compared to ASR 1.8 and 3.0. Additionally, the cell outputs at ASR 3.0 did not exhibit a significant increase compared to ASR 1.8.

At 0.3 A/cm^2 , the cell outputs at ASR 2.4 (0.16421 W/cm^2 and 0.54735 V) were 13.17% and 16.60% higher than those at ASR 3.0 (0.1451 W/cm^2 and 0.48365 V) and ASR 1.8 (0.14083 W/cm^2 0.46943 V), respectively.

Similarly, at the highest current density of 0.45 A/cm^2 , an ASR of 2.4 yielded peak cell outputs of 0.20322 W/cm^2 achieved at 0.45159 V of cell potential. Which are 16.87% and 22.51% higher than those recorded at ASR 3.0 (0.17388 W/cm^2 with 0.38640 V) and ASR 1.8 (0.16588 W/cm^2 with 0.36862 V), respectively.

In summary, the individual evaluation of ASR's effect on PEMFC performance aligns with the orthogonal test results, confirming that the optimal ASR remains at 2.4.

4.4 DROPLET PURGE

In light of the Orthogonal test results, test number 7 (OT 80°C , RH 50%, COP 22psi, and ASR 2.4) is considered the optimal operating condition due to its highest power density peak at $0.45 \text{ (A/cm}^2\text{)}$ current density or 11.25 (A) load. However, the cell could not supply a higher current density than $0.45 \text{ (A/cm}^2\text{)}$ of current density due to a flood taking place at the cathode side. Therefore, purging droplets out is essential to settle this problem and improve cell performance. This study used a solenoid valve to purge droplets out, called the purge valve.

4.4.1 Normal operation

The cell was run at the test 7 condition and applied 12.5 (A) load in 30 minutes to observe the natural droplets' pushing frequency. Meanwhile, the back pressure, current, voltage, and solenoid status were recorded at a sampling rate of 0.25 (s) as shown in **Figure 4.20**. The solenoid status is open and closed when its status is equal to 1 and 0, respectively.

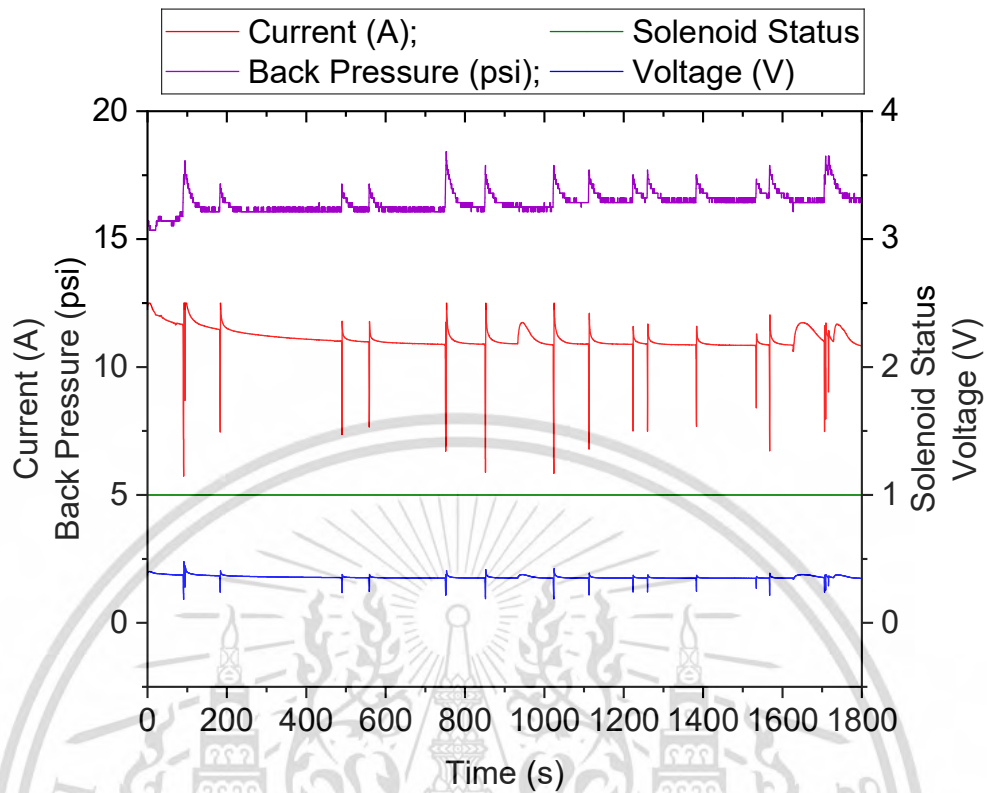


Figure 4.20 The natural droplets pushing frequency of the PEM fuel cell

It is obvious that the natural droplets pushing is unclean resulting in slightly increasing back pressure over time while trendlines of current and voltage are moderately decreasing. The mean power density is 0.15939 W/cm^2 and STDEV is 0.01380 W/cm^2 , which are used as the reference for comparisons of purge strategies. The purge interval varies from 35 (s) to 310 (s) while the purge duration takes place very fast within 1 (s). Hence, two value sets of purge interval and purge duration (s), which were chosen to optimize the purge process, are (10, 20, 30) and (0.25, 0.50, 0.75), respectively. Following that, nine test cases were designed as illustrated in the Table 4.7.

Table 4.7 Droplets purge strategies

Test number	Interval time (s)	Purging time (s)
1	10	0.25
2	10	0.50
3	10	0.75

4	20	0.25
5	20	0.50
6	20	0.75
7	30	0.25
8	30	0.50
9	30	0.75

Taking a natural droplet pushing from seconds 178 to 198 in the **Figure 4.20** and zoom in to get the details of flooding, demonstrated in **Figure 4.21**.

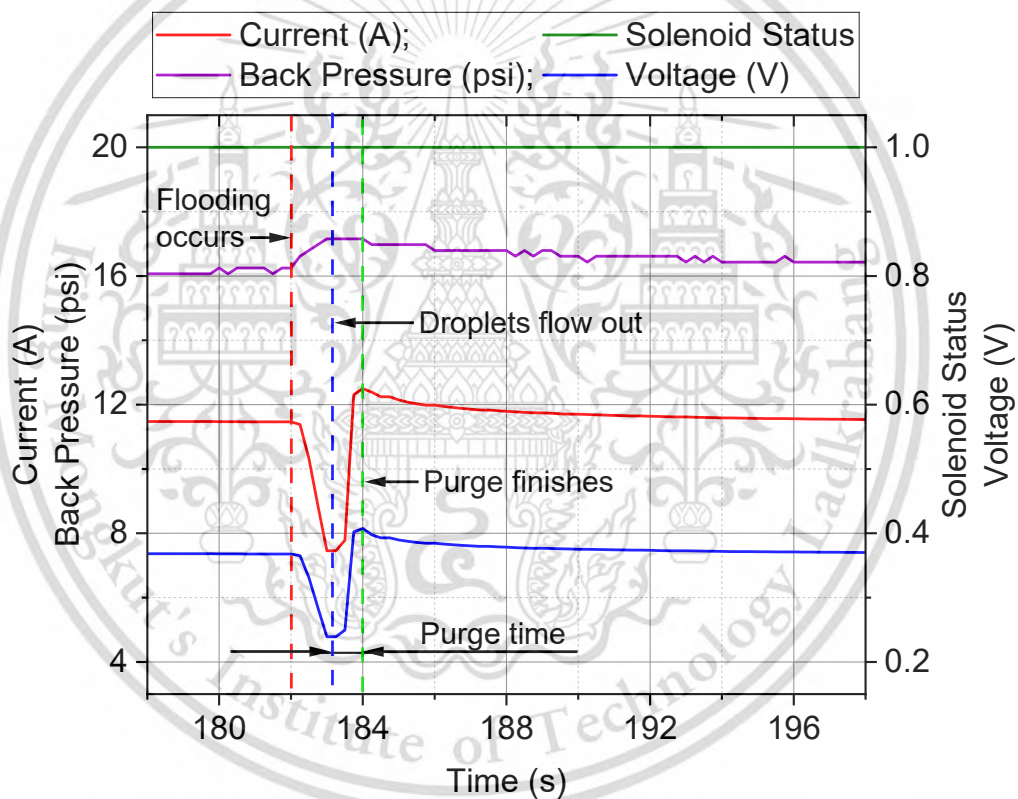


Figure 4.21 Diagram of flooding diagnosis under normal operation

As demonstrated in **Figure 4.21**, the cell can not supply 12.5 A load. When droplets accumulate enough to block the flow channels, a flood takes place. In the first second of a flood, back pressure slightly increases by 1 psi while the cell output voltage and current plummet by 0.1 V and 2 A, respectively. After that, voltage and

current soar higher than before flooding, current supply the 12.5 A load and voltage reach 0.4 V while back pressure remain 17 psi in one second.

4.4.2 Various purge strategies

In accordance with the interval time and purging time varying from 10, 20, 30 (seconds) and 0.25, 0.50, 0.75 (seconds), respectively, the plotting time and sampling rate were set to 100 and 250 (milliseconds) to fully acquire data from nine test cases. Throughout the droplet purge tests, the cell was working at the optimal condition of the Orthogonal test and applied 12.5 A load which is 0.5 A/cm^2 of current density.

When the cell working under purge operations, the typical cell outputs behave as demonstrated in Figure 4.21.

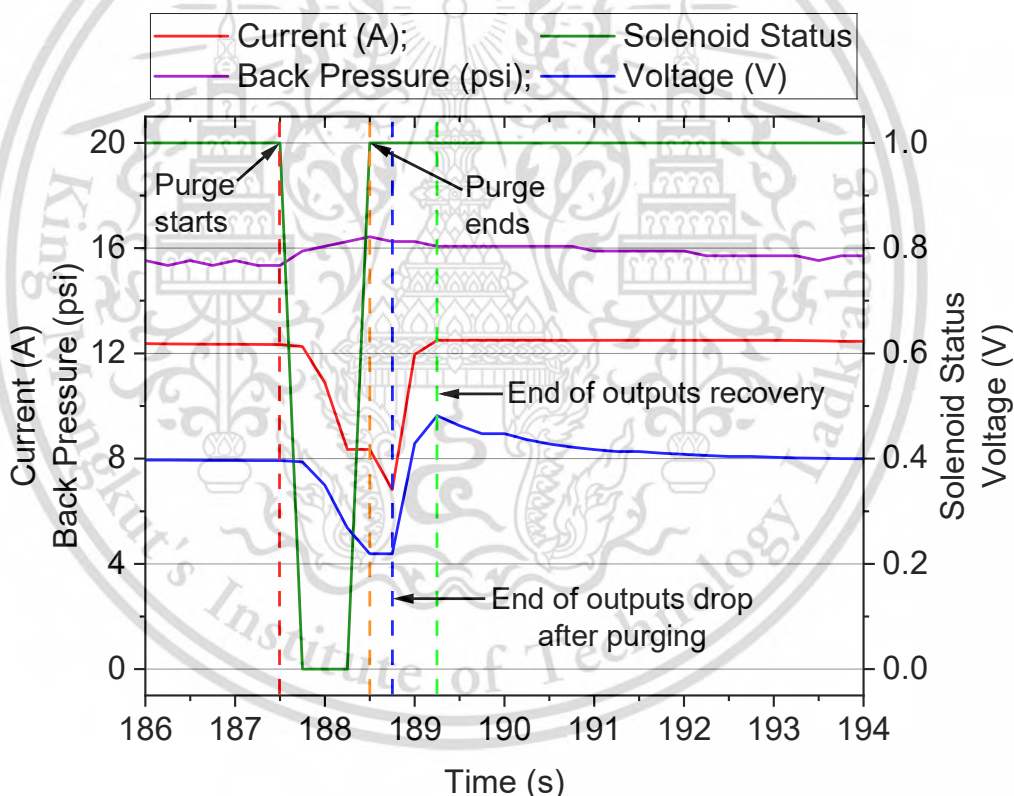


Figure 4.22 Diagram of PEMFC outputs diagnosis under purge operation of purge interval 10s and purge duration 0.75s

Figure 4.22 depicts the dynamic behavior of the cell's back pressure, current, and voltage upon the commencement of solenoid closure. Initially, back pressure experiences a rise together with the drops in voltage and current when the solenoid

closes. Back pressure ceases to rise once the solenoid opens, followed by a subsequent increase in current and voltage. This sequence leads to the modulation of troughs and peaks in the cell outputs' curves. The duration between the initiation of a purge and the subsequent drop in output is termed as the 'decrease time after purging' (s). Additionally, the period from the troughs to the peaks of the cell outputs following solenoid opening is referred to as the 'recovery times'.

4.4.2.1 Purge interval 10 seconds

During the 10-second purge interval, various purge durations were tested, and the statuses of the solenoid, back pressure, output voltage, and current were meticulously recorded, as depicted in **Figure 4.23**. The cell's output currents and voltages exhibited fluctuations across purge durations of 0.25s, 0.5s, and 0.75s, with discernible increases in their amplitudes.

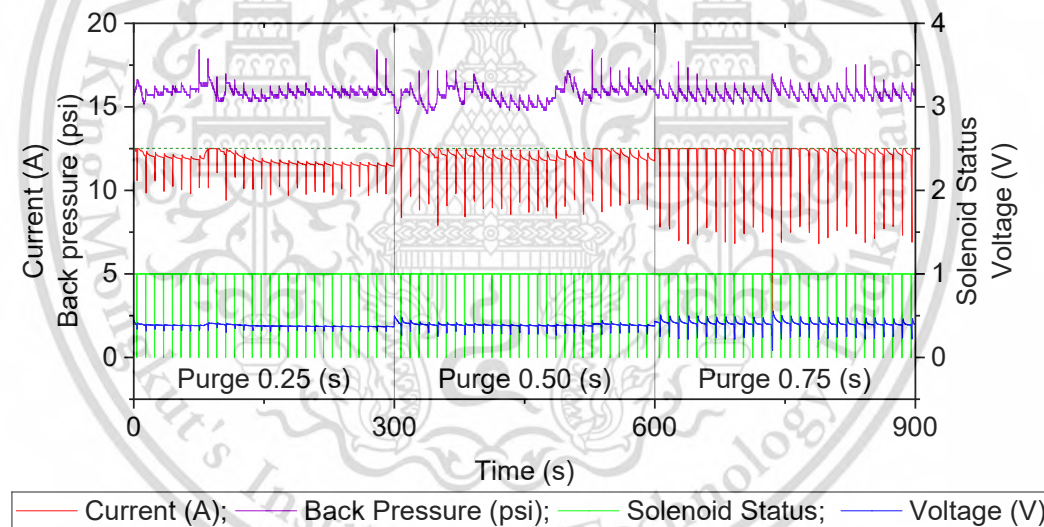


Figure 4.23 Various purge durations at purge interval 10s

At a 0.25s purge duration, the cell struggled to sustain a 12.5 A load, resulting in a conspicuous gap between the red line and the dashed dark green line. Conversely, the 0.5s purge duration displayed an improved output current, with peaks nearly reaching the desired 12.5 A load. Remarkably, the 0.75s purge duration not only facilitated the achievement of a 12.5 A output current but also maintained it for an extended period post-purging, indicative of enhanced cell performance. Detailed insights into the 10-second purge interval strategies are provided in **Table 4.8**, revealing

that increasing the purge duration correlated positively with the average output voltage and current. However, this increase also corresponded to elevated standard deviations (STDEV) in cell outputs.

Table 4.8 Current and voltage characteristics under 10s purge interval operation

Purge duration (s)		0.25	0.5	0.75
Current	Before purging (A)	11.74851	11.91919	12.28858
	Trough (A)	10.05045	8.98171	7.20420
	Peak (A)	11.98014	12.41559	12.49938
	Decrease time after purging (s)	0.57500	0.73276	0.97414
	Recovery time (s)	0.55000	0.57759	0.61207
	Mean	11.75673	11.93691	12.09502
	STDEV	0.45965	0.69481	1.13910
Voltage	Before purging (V)	0.37751	0.38296	0.39659
	Trough (V)	0.32291	0.28834	0.23145
	Peak (V)	0.38647	0.40941	0.48442
	Decrease time after purging (s)	0.57500	0.74138	0.97414
	Recovery time (s)	0.55000	0.56897	0.62069
	Mean	0.37804	0.38556	0.40308
	STDEV	0.01571	0.02611	0.04679

The impact of increasing purge duration from 0.25s to 0.5s, and 0.75s is evident in the following observations:

Firstly, the average current increased from 11.75673 A to 11.93691 A, and 12.09502 A, while the mean voltage rose from 0.37804 V to 0.38556 V, and 0.40308 V, respectively. Noticeably, the highest outputs and their respective STDEV were recorded at the 0.75s purge duration, with values of $0.40308 \pm 0.04679V$ and $12.09502 \pm 1.13910A$.

Secondly, the average oscillation amplitudes of outputs increased from 1.92969 A to 3.43388 A, and 5.29018 A for current, while they rose from 0.06356 V to 0.12107 V and 0.25297 V for voltage.

Thirdly, the pre-purging outputs were sustained for longer durations with increasing purge durations, specifically from 11.74851 A to 11.91919 A, and 12.28858 A for current, and from 0.37751 V to 0.38296 V, and 0.39659 V for voltage.

Fourthly, the decrease time after purging increased from 0.57500 s to 0.73276 s, and 0.97414 s for current, and for voltage from 0.57500 s to 0.74138 s, and 0.97414 s.

Fifthly, the recovery time of current increased from 0.55000 s to 0.57759 s, and 0.61207 s, while for voltage, it rose from 0.55000 s to 0.56897s, and 0.62069 s.

In summary, the augmentation of purge durations within the 10-second interval exhibited improvements in cell outputs alongside their respective standard deviations.

4.4.2.2 Purge interval 20 seconds

Similar to the 10-second purge interval, various purge durations (0.25, 0.5, and 0.75 seconds) were tested at a 20-second interval, with details in **Table 4.9**. **Figure 4.24** again illustrates the effects on solenoid status, back pressure, and cell output voltage and current.

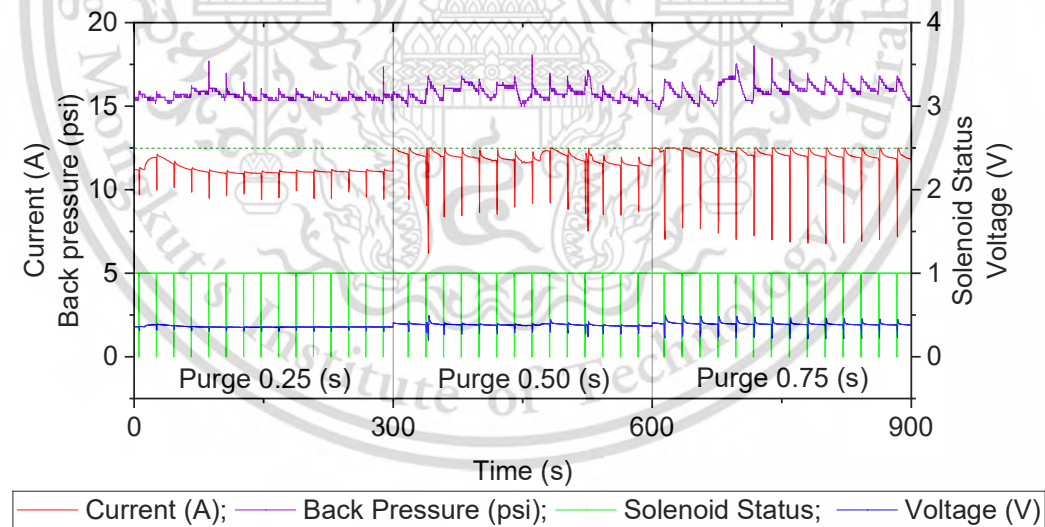


Figure 4.24 Various purge durations at purge interval 20s

Cell performance improved with increasing purge durations but to a lesser extent compared to the 10-second purge interval. While a 0.25-second purge duration resulted in a significant blank area (indicating inability to meet the 12.5 A load) between the red line and the dashed dark green line shown in **Figure 4.24**, a 0.5-second purge

at 20 seconds could reach the load briefly. Moreover, a 0.75-second purge could only achieve the load after recovery, unlike the sustained performance observed at a 10-second purge interval.

Table 4.9 shows a slight increase in average output voltage and current with increasing purge duration at 20 seconds, accompanied by a rise in STDEV. The highest recorded outputs (0.39088 ± 0.02981 V and 12.04872 ± 0.78483 A) occurred at 0.75 seconds.

Table 4.9 Current and voltage characteristics under 20s purge interval operation

Purge duration (s)		0.25	0.5	0.75
Current	Before purging (A)	11.11557	11.79906	12.03258
	Trough (A)	9.67785	8.77524	7.10697
	Peak (A)	11.30236	12.31525	12.49939
	Decrease time after purging (s)	0.51667	0.78571	0.94643
	Recovery time (s)	0.61667	0.55357	0.58929
	Mean	11.14744	11.81693	12.04872
	STDEV	0.32927	0.60989	0.78483
Voltage	Before purging (V)	0.35747	0.37919	0.38659
	Trough (V)	0.31113	0.28210	0.22835
	Peak (V)	0.36337	0.40283	0.47013
	Decrease time after purging (s)	0.51667	0.78571	0.94643
	Recovery time (s)	0.61667	0.51786	0.60714
	Mean	0.35838	0.38039	0.39088
	STDEV	0.01061	0.02047	0.02981

The impact of increasing purge duration from 0.25s to 0.5s and 0.75s can be observed through the following reactions of the cell:

Firstly, the average current increased from 11.147442 A to 11.81693 A, and 12.04872 A, while the mean voltage rose from 0.35838 V to 0.38039 V, and 0.39088 V, respectively. Markedly, at a 0.75s purge duration, the highest outputs and their respective STDEV were recorded as 0.39088 ± 0.02981 V and 12.04872 ± 0.78483 A.

Secondly, the average oscillation amplitudes of outputs increased from 1.62451 A to 3.54001 A, and 5.39242 A for the current, while they rose from 0.05224 V to 0.12073 V, and 0.24178 V for the voltage, respectively.

Thirdly, pre-purging outputs no longer remained consistent with increasing purge durations, transitioning from 11.11557 A to 11.79906 A, and 12.03258 A for the current, and from 0.35747 V to 0.37919 V, and 0.38659 V for the voltage.

Fourthly, the decrease time after purging increased from 0.51667 s to 0.78571 s, and 0.94643 s for current, and for voltage from 0.51667 s to 0.78571 s, and 0.94643 s.

Finally, the recovery time of current increased from 0.61667 s to 0.55357s, and 0.58929 s, while for voltage, it rose from 0.61667s to 0.51786s, and 0.60714 s. Noticeably, the fastest recovery times of cell outputs were achieved with a purge duration of 0.5s.

In conclusion, increasing the purge durations within the 20-second purge interval led to improvements in cell outputs alongside higher STDEV. While the decrease time after purging of cell outputs increased with longer purge durations, the fastest recovery times were recorded at a 0.5s purge duration.

4.4.2.3 Purge interval 30 seconds

This section examines the effects of purge duration on cell performance at a 30-second purge interval. Solenoid status, back pressure, and cell output voltage and current were monitored during various purge durations (0.25, 0.5, and 0.75 seconds) as shown in **Figure 4.25**. The cell's output currents and voltages displayed variations across purge durations of 0.25s, 0.5s, and 0.75s, with observable increases in their amplitudes.

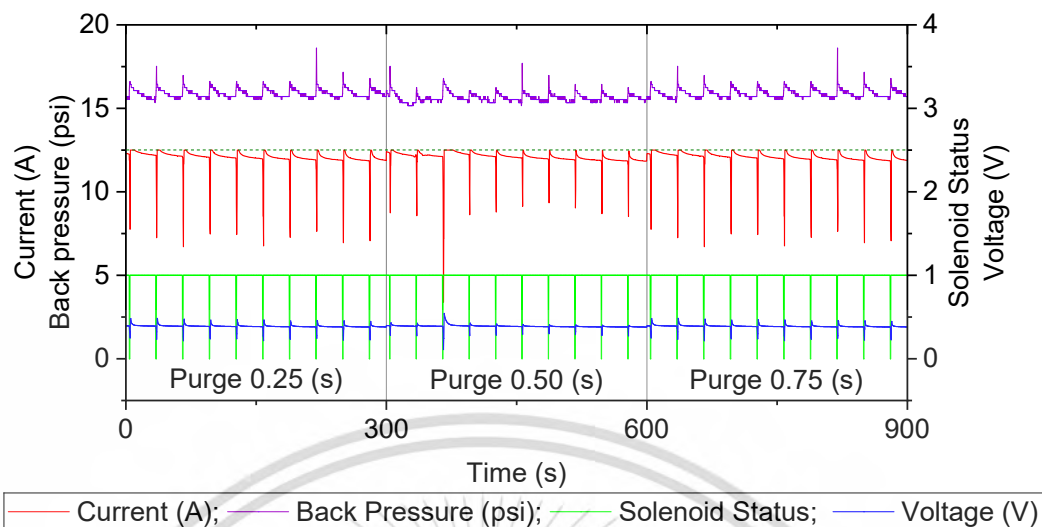


Figure 4.25 Various purge durations at purge interval 30s

Although the cell managed to reach a 12.5 A applied load after purging at all purge durations, it struggled to maintain this level for an extended duration. Particularly, the current stability at the 0.5s purge duration appeared superior to that observed at 0.25s or 0.75s, whereas the voltages across the three purge durations exhibited minimal differences. Details of the results are presented in **Table 4.10**.

Table 4.10 Current and voltage characteristics under 30s purge interval operation

Purge duration (s)		0.25	0.5	0.75
Current	Before purging (A)	11.69030	12.03368	11.95724
	Trough (A)	9.83204	8.28132	7.23068
	Peak (A)	11.97760	12.49235	12.49940
	Decrease time after purging (s)	0.52778	0.80000	0.95000
	Recovery time (s)	0.61111	0.60000	0.60000
	Mean	11.76092	12.05722	12.02670
	STDEV	0.23969	0.52193	0.65643
Voltage	Before purging (V)	0.37537	0.38634	0.38384
	Trough (V)	0.31570	0.26590	0.23211
	Peak (V)	0.38458	0.42732	0.46569
	Decrease time after purging (s)	0.52778	0.80000	0.95000

	Recovery time (s)	0.61111	0.57500	0.62500
	Mean	0.37763	0.38864	0.38798
	STDEV	0.00770	0.02023	0.02426

Analysis from **Table 4.10** reveals that increasing the purge duration from 0.25s to 0.5s, and 0.75s elicited the following responses from the cell:

Firstly, the average current changed from 11.76092 A to 15.63261 A, and 12.02670 A, while the mean voltage increased from 0.37763 V to 0.38864 V, and 0.38798 V, respectively. Notably, at the 0.5s purge duration, the highest outputs and a moderate STDEV were recorded, with values of $0.38864 \pm 0.02023\text{V}$ and $15.63261 \pm 0.52193\text{A}$.

Secondly, the average oscillation amplitudes of outputs increased from 2.14556 A to 4.21103 A, and 5.26872 A for the current, while they rose from 0.06888 V to 0.16142 V, and 0.23358 V for the voltage, respectively.

Thirdly, the values of outputs before purging ranged from 11.69030 A to 12.03368 A, and 11.95724 A for the current, and from 0.37537 V to 0.38634 V, and 0.38384 V for the voltage. Notably, the outputs after purging remained longest at the 0.5s purge duration.

Fourthly, the decrease time after purging increased from 0.52778 s to 0.80000 s and 0.95000 s for current, and for the voltage from 0.52778 s to 0.80000 s and 0.95000 s.

Finally, the recovery time of current decreased from 0.61111 s to 0.60000 s, and remained at that value for the 0.75s purge duration, while for voltage, it decreased from 0.61111s to 0.57500 s, then increased to 0.62500 s. Notably, the fastest recovery times of cell outputs were achieved with a purge duration of 0.5s.

Overall, the optimal purge strategy in this test set was the 0.5s purge duration, characterized by the highest outputs, consistent values before purging, shortest recovery time, and moderate STDEV. Therefore, increasing the purge durations to 0.75s or beyond within the 30s purge interval resulted in decreased cell outputs or failed to significantly improve them. While the decrease time after purging of cell outputs increased with longer purge durations, the fastest recovery times were consistently recorded at the 0.5s purge duration.

4.4.3 Effect of purge strategies on PEMFC power density

In assessing the performance of the cell, power density is a critical factor, taking into consideration both output voltage and current. **Figure 4.26** illustrates nine purge strategies along with their respective average power densities and standard deviations (STDEVs).

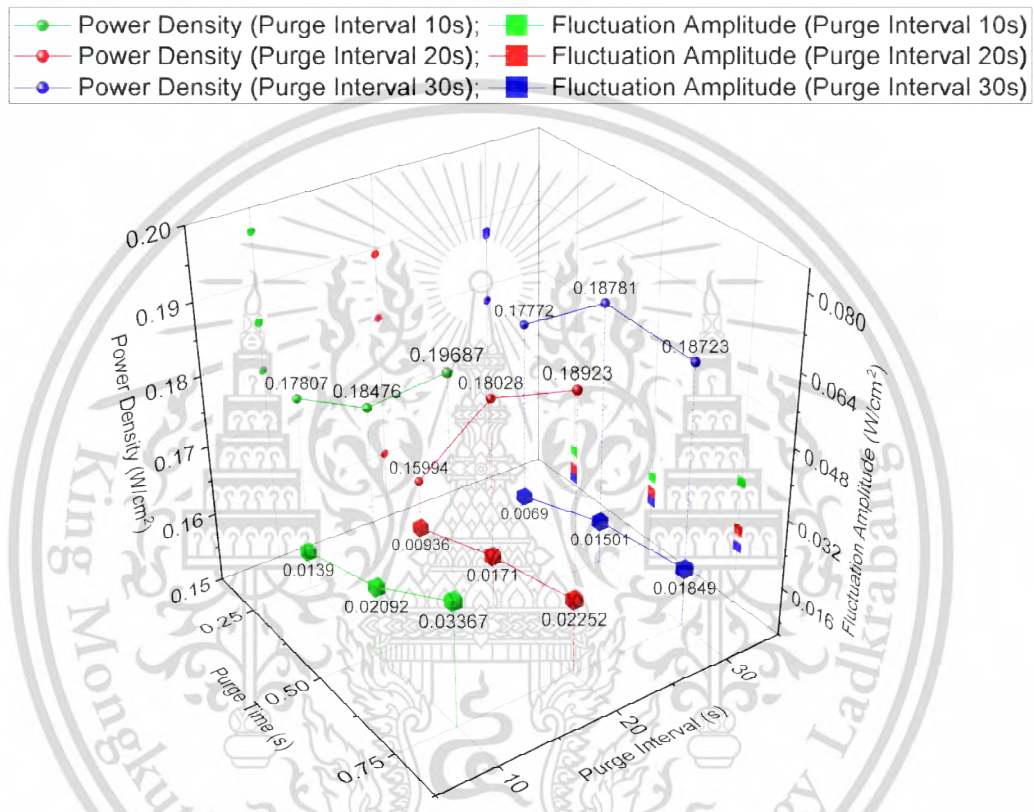


Figure 4.26 Power density and stability of various purge strategies

Conspicuously, increasing purge durations were observed to correlate with higher power density, while increasing purge intervals contributed to greater output stability. For instance, at a 10-second purge interval, a purge duration of 0.75 seconds emerged as the optimal condition for enhancing power density, resulting in a notable increase of 3.75% (STDEV 50.504%) and 10.558% (STDEV 60.946%) when compared to purge durations of 0.25s and 0.5s, respectively.

Similarly, at a 20s purge interval, significant power density improvements of 12.717% (STDEV 82.692%) and 18.313% (STDEV 140.598%) were achieved by extending

the purge duration from 0.25s to 0.5s, and 0.25s to 0.75s, respectively, thus affirming the efficacy of a 0.75s purge duration.

At a 30s purge interval, power density increased by 5.677% (STDEV 117.536%) and 5.351% (STDEV 167.971%) with purge duration increments from 0.25s to 0.5s, and 0.25s to 0.75s, respectively. Remarkably, a 0.5s purge duration exhibited the best power density and lowest STDEV in this group.

Table 4.11 Comparisons of purge strategies and the optimal condition from orthogonal tests (0.15939 W/cm², STDEV = 0.01380 W/cm²)

Test	Power Density Enhancement (%)	STDEV increasing (%)
1	11.718	0.693
2	15.919	51.588
3	23.518	143.982
4	0.345	-32.169
5	13.109	23.941
6	18.723	63.179
7	11.503	-50.024
8	17.828	8.730
9	17.468	34.005

In summary, increasing purge duration (from 0.25s to 0.75s) and reducing purge interval (from 30s to 10s) contributes to power density improvement of PEMFC but they also reduce the stability of cell outputs. The optimal purge strategy for achieving the highest power density involves a 10s purge interval and a 0.75s purge duration with 23.515% power density enhancement (STDEV increasing 143.986%) from the optimal condition of the orthogonal test. However, for a balance of power density and stability, the 30s purge interval with a 0.5s purge duration emerges as the preferred condition (power density improved 17.830% and STDEV increasing 8.768%), as indicated in **Table 4.11**.

CHAPTER 5

DISCUSSIONS

The 2-parameter test results reveal a complex interaction between operating temperature (OT), relative humidity (RH), and current density on cell performance. Unlike individual parameter analysis, which might suggest independent trends, the optimal conditions for cell output shift across the current density range. At low and medium current densities, a combination of 60°C OT and 70% RH proves favorable. This is because less water vapor is supplied at this condition, minimizing water production within the cell. The higher RH helps maintain membrane hydration, promoting its proton conductivity [65]. However, at high current densities, the trend reverses. Cell outputs increase with both rising OT and RH. This can be attributed to two factors. First, higher temperatures (around 80°C) reduce the activation energy required in the catalyst layer, leading to a faster reaction rate and improved PEMFC performance [66, 67]. Second, excessively high temperatures can dehydrate the membrane, reducing its conductivity. Therefore, increasing RH alongside OT becomes crucial to maintaining membrane hydration and optimal performance [23]. Interestingly, at 60-70°C OT, a decrease in RH with increasing current density maintains good performance. Conversely, at 80°C OT, 70% RH is necessary for optimal operation. This can be explained by the enhanced proton conductivity at 70°C OT due to increased water content in the membrane and reduced transmission impedance with higher RH [49, 67]. These findings highlight the limitations of analyzing individual parameters and emphasize the importance of considering their combined effects. Notably, the optimal OT identified here (70°C at high current density) deviates from individual parameter studies suggesting varying optimal OTs based on RH. This underscores the need for a comprehensive analysis of all operating parameters for effective PEMFC optimization.

The four-parameter test results show that the maximum performance over current density was recorded at test 5 from 0-0.25 A/cm², test 1 from 0.25-0.37 A/cm², and test 7 from 0.37-0.45 A/cm². Group 1 exhibited the highest cell output voltages across the entire current density range, followed by group 2 and then group 3. Commonalities between group 1 and group 2 include low RH (50%), high COP (22 psi),

and low OT (60 °C). Where low RH (50%), high COP (22 psi), and low OT (60 °C) appear frequently in groups 1 and 2, suggesting these parameters promote favorable performance at low to medium current densities (0-0.3 A/cm²). In comparison with the two-parameters test results, the OT 60 °C still is the favorable condition. Conversely, group 2 and group 3 shared high RH at 70%, medium COP at 15 psi, and high ASR at 3.0. Where RH 70% presented two times in group 3 while bolt COP 15 psi and ASR 3.0 appeared twice in group 2, indicating these conditions hinder performance at high current densities (0.3-0.45 A/cm²). In comparison with two-parameters test results, RH 70% showed better cell outputs at low current density but reduce cell output at high current density. These differences might caused by two different membranes used for the two-parameter test and the four-parameter test. Another reason might be caused by the effects of COP and ASR. Therefore, it again states that is crucial to study the combined effects of all operating parameters on PEMFC performance instead of individual effect, especially in the case of optimization of operating parameter over the raise of current density. Despite Test 3 in **Table 4.4** containing two favorable conditions (COP 22 psi and OT 60°C) and two unfavorable conditions (RH 70% and ASR 3.0), its voltage significantly plummeted to 0.364 V at high current density. Opposite, Test 4, which had only one favorable condition (RH 50%) amidst two adverse conditions (COP 15 psi and ASR 3.0), still generated a relatively good voltage. These inconsistencies clearly state that at high current density, the effect of RH and ASR are higher than COP and OT, in which, RH has a bigger impact than ASR. They are confirmed to be true when looking at the influence degree of parameters on PEMFC performance at a high current density range, showed in **Figure 4.15**.

Evaluations of individual parameter effects based on the optimal conditions from the orthogonal test again ensure the orthogonal results are correct, where the optimal conditions of orthogonal are still the best PEMFC performance in individual tests. Therefore, literature [10, 31, 33] support for this method that is efficient and suitable for defining optimal parameters of PEMFC and maximizing its performance.

Increasing OT has a positive effect on PEMFC performance because higher temperatures facilitate faster kinetics of electrochemical reactions, allowing more efficient utilization of the catalysts on both electrodes. On the other hand, the membrane plays a crucial role in facilitating proton conduction. This conductivity is

highly dependent on the membrane's water content. Therefore, when evaluating the influence of temperature on membrane conductivity, it's essential to consider the relative humidity (RH) or water content within the membrane itself [23]. In practice, the experimental result of individual OT effect on PEMFC performance showed that the increase of OT is nonlinear to the rise of cell outputs. Exceptionally, the cell output dropped then rose when accelerating OT from 60°C to 70°C and then 80°C while other parameters were kept unchanged (RH 50%, COP 22psi, and ASR 2.4). At low temperatures (60°C), water management in the PEMFC can be delicate. As the temperature rose to 70°C, some of the generated water might initially evaporate from the membrane, reducing its proton conductivity and contributing to a decrease in cell outputs. As the temperature reaches 80°C, the dominant effect becomes the improvement in reaction kinetics. Higher temperature increases the mobility of reactant molecules and improves the efficiency of the electrochemical reactions at both anode and cathode. This leads to a rise in cell voltage and overall power output as demonstrated in **Figure 4.16**.

Increasing COP in this study has a positive effect on PEMFC performance which can be deduced from **Equation 1.5**. Nevertheless, COP increase may lead to the internal passing of electrons through the electrolyte rather than through the external circuit, even though the membrane is practically impermeable to electrons [11]. Furthermore, the higher COP would consume more electricity of the air compressor and reduce the total efficiency of FCEVs.

Low ASR is not good for PEMFC performance due to insufficient oxygen supply. Particularly, PEMFCs require oxygen from the air to complete the electrochemical reaction with hydrogen at the cathode. If the air stoichiometry ratio is too low, there will not be enough oxygen available to fully react with the hydrogen. This leads to incomplete oxidation and reduces the cell's performance. Besides that, high ASR is not ideal for PEMFCs. Considering that PEMFCs require a specific amount of oxygen to efficiently react with hydrogen at the cathode. When the air stoichiometry ratio is too high, there is an excess of air relative to the amount needed for the complete oxidation of hydrogen. This excess air dilutes the reactants (hydrogen cation, electron, and oxygen), reducing their concentrations at the cathode side within the fuel cell. As a result, the rate of electrochemical reactions can decrease because not all active sites

on the catalyst are utilized effectively. In this study, ASR is defined as optimal at 2.4 which is near ASR 2.5 of Shixiang Xia [10] and Dengcheng Liu [33].

Generally, the individual effect of four operating parameters are matched with the orthogonal test result. It is worth saying that the lower RH and higher COP lead to higher cell performance. However, the increases of OT and ASR are not proportional to the rise of cell outputs. In this study, the optimal conditions of OT and ASR are 80 °C and 2.4, respectively. Other studies examined the effect of parameters at a specific current density and conducted the optimal condition [10, 33] while this research found that the optimal conditions change over current density ranges which is essential in the case of optimization parameters. Additionally, the influence degrees of four parameters were calculated at all the current density ranges of PEMFC, which addresses which parameter should be given the priority at a specific current density when optimizing the operating parameters. In which, the trendlines of OT and RH impact on PEMFC look similar but the effect of RH started to be significant and higher than OT earlier in the four-parameter test. Especially, in the four-parameter test, the impact of RH after switching to OT became the biggest compared to OT, COP, and ASR showed in **Figure 4.15**. Therefore, water management is important and focused in the next part of this research. In this study, **Table 3.4** demonstrates that the two-parameter test and four-parameter test utilized different MEAs. The Nafion 112 in the two-parameter test exhibited poorer condition compared to the brand-new PFSA S30-R ePTFE Reinforced PEM in the four-parameter test, leading to distinct OCVs: approximately 0.75V for the two-parameter test and approximately 0.92V for the four-parameter test. Moreover, the variations in testing cell configurations can explain differing degrees of influence from operational parameters in this research compared to others. Specifically, RH exerted a dominant impact compared to ASR, unlike studies by Shixiang Xia et al. [10] and Dengcheng Liu et al. [33], who reported that ASR had a greater influence than RH at 0.5 A/cm².

Different purge intervals and purge durations were tested to optimize the droplet purge process of the cathode. The purpose of optimization is to obtain a purge duration and a purge interval at which improved and stable power density of PEMFC is achieved. The investigation into different purge intervals (10s, 20s, and 30s) and durations (0.25, 0.5, and 0.75 seconds) yielded valuable insights into their impact on

PEMFC performance. The primary focus was to understand how these factors influence aspects such as back pressure, output voltage, current, and power density aligning with the objective of improving PEMFC power density by 20%. Key findings will be discussed as follows.

Higher purge durations generally led to increased average cell outputs (voltage and current) across all purge intervals. However, this was accompanied by a rise in the standard deviation (STDEV) of the outputs, indicating greater fluctuations. It can be explained that the purge duration is controlled by closing the solenoid valve, increasing the close time causes the back pressure to rise hence the COP increase. The longer the purge duration, the higher COP obtained and the longer decreasing time of cell outputs. As a result, droplets are formed faster and bigger blocking the flow field and covering the reaction surface of CL with reactants, which make the cell outputs plummet significantly. When the valve is open, droplets are pushed out due to the difference of pressure inside and outside the cell. The higher the pressure difference, the faster and cleaner droplet flow out. On one hand, the cell output would soar after a purge is complete. Current would reach the applied load (12.5A) and voltage would reach the peak higher than before purging then gradually decreasing according to more accumulated water inside the cell over time. At 20 and 30 seconds, the fastest recovery times of the cell's outputs were observed at 0.5-second purge durations. Therefore, increasing the purge duration seems good for performance but causes higher output fluctuation. Conversely, the abrupt change in COP results in inconsistent ASR, impacting the rate of electrochemical reactions in PEMFCs and the operational reliability of FCEVs. This phenomenon requires validation in real-world scenarios. Therefore, future research should examine the effects of cathode droplet purging on FCEVs, focusing on reliability and system complexity.

A shorter purge interval led to best-maintained pre-purge output levels because the purge repeated faster and droplets were pushed out more regularly, which could enhance the PEMFC performance overall. However, it also results in more purge processes in a period and increases the output STDEV in total.

Table 4.11 illustrates that employing the cathode droplet purge method can significantly enhance PEMFC performance at a current density of 0.5 A/cm^2 . Compared to the optimal condition determined by the orthogonal test, Test 3 demonstrated a 23.518% increase in power density, equivalent to a 143.982 STDEV increase, while

Test 7 showed an 11.503% enhancement in power density along with a 50.024% reduction in STDEV. It is crucial, however, to acknowledge the trade-off between improving performance and managing output fluctuations. By considering specific standards or requirements for cell output and allowable fluctuation ranges, the most suitable purge strategy can be selected for optimal control. Nevertheless, it is worth noting that recent PEMFCs typically operate at current densities of 2.67 A/cm² or higher [68], which exceed the current outputs studied in this research. Therefore, further efforts are necessary to increase the power density of PEMFCs, thereby making them more practical and applicable to FCEVs.

Existing literature supports the findings that purge duration impacts dead-end anode cell performance [38, 41, 63, 69]. The initial hypothesis was that a solenoid valve-controlled purge could extend the high power density range of PEMFC by managing water removal. The results partially support this. While longer purge durations increased average outputs at all intervals, the trade-off with higher STDEV indicates potential stability issues. Besides that, the optimal purge strategy likely depends on specific cell designs and operating conditions.

A limitation of this study is focusing on the cathode side only (COP and droplets purge) and the small test size (limited number of purge durations and intervals tested). Further research will consider the anode side also for a comprehensive analysis of PEMFC operation and investigate a wider range of purge durations and intervals to refine the optimal strategies and explore the influence of purge strategies on cell performance at different current densities. Besides that, further research with a focus both on power density and efficiency of PEMFC that are needed to refine our the real operating current density range of PEMFC, and develop tailored strategies for enhancing PEMFC performance in real-world applications. Even the optimal conditions over current density could be defined by the orthogonal method, it's necessary to consider the transition times of each parameter if they are too long or fast. Because in real FCEVs, OT is controlled by a cooling system or heating system, RH is controlled by a humidification system (Hyundai), ASR and COP are controlled by a compressor, all of which require energy and time to respond to a specific value.

The droplet purge study at the cathode side of PEMFC provides new insights into the interplay between purge duration, purge interval, and PEMFC performance

metrics like average voltage, current, power density, STDEV, and recovery times. The observed variations in the optimal purge duration depending on the purge interval highlight the importance of considering both factors for effective purge control strategies. Also, it proposed a way to improve PEMFC performance by 23.515% at its highest power density by controlling back pressure to purge droplets out.



CHAPTER 6

CONCLUSION

This research investigates the influence of operating parameters and droplet purge strategies on the proton exchange membrane fuel cell performance, aiming for a 20% power density improvement. The study addresses the following key questions:

- How do operating parameters affect PEMFC performance across various current density ranges?
- What is the relative impact of each parameter on cell performance?
- How can optimal operating conditions be defined for a single 25 cm² PEMFC?
- How do cathode-side droplet purge strategies influence PEMFC power density and stability?
- How can a 20% power density enhancement be achieved in PEMFCs?

A custom-designed test system was developed for evaluating and optimizing various operating parameters (OT, RH, COP, and ASR) and droplet purge strategies (duration and interval) in small PEMFCs.

The effect of operating parameters varied over current density, test objectives, and cell configurations. Cell performance increased proportionally with an increase in COP and a decrease in RH while exhibiting a disproportionate relationship with increases in OT and ASR. The highest PEMFC performance was recorded at (OT 70°C, RH 60%, COP 22psi, and ASR 1.8) from 0-0.25 A/cm², (OT 60°C, RH 50%, COP 8psi, and ASR 1.8) from 0.25-0.37 A/cm², and (OT 80°C, RH 50%, COP 22psi, and ASR 2.4) from 0.37-0.45 A/cm². In the four-parameter results, the comparison of individual parameter effects aligned with the orthogonal result, where the optimal condition remained the best performance across all tests. A new finding for a more comprehensive parameter study is that it is crucial to study the effects of all operating parameters on PEMFC performance instead of individual effects.

Range analysis identified the dominant operating parameters at different current density ranges: OT (0-0.04 A/cm²), COP (0.04-0.15 A/cm²), and RH (0.15-0.45 A/cm²). This information provides valuable guidance for prioritizing parameters during optimization for specific current density targets. Since this research focused on

improving power density typically achieved at high current densities, the role of RH was also investigated for droplet purge optimization.

A novel droplet purge method for flow-through cathode PEMFCs was proposed. The experimental results demonstrated that both purge duration and interval significantly affect PEMFC performance and stability. Notably, increasing purge duration (0.25s to 0.75s) and decreasing purge interval (30s to 10s) led to improvements in both power density and performance fluctuation. This finding underscores the trade-off between maximizing power density and maintaining stability during purge process optimization.

The study identified the optimal purge strategy for power density enhancement as 0.75s duration and 10s interval, achieving a 23.515% increase in power density (with a corresponding 143.986% increase in STDEV) compared to the optimal condition from the orthogonal test at its extended power density peak. However, considering both power density and stability, a more balanced approach was identified: a purge strategy with 0.5s duration and 30s interval offered a 17.830% power density increase with a modest STDEV increase of 8.768%.

Future research works should attempt to enhance the power density of PEMFC and explore the combined optimization of PEMFC efficiency and power density to define the practical current density operating range, typically situated between the efficiency and power density peaks. Additionally, a broader range of test cases could be conducted to identify strategies that deliver the best power density within acceptable STDEV limits. These advancements would significantly contribute to enhancing PEMFC performance for real-world applications in fuel cell electric vehicles.

REFERENCES

1. Zhu Liu, Z.D., Steve Davis & Philippe Ciais, *Monitoring global carbon emissions in 2022*. Nature Reviews Earth & Environment, 2023. **4**(4): p. 205-206.
2. IEA, *World Energy Outlook 2022*, IEA, Editor. 2022: Paris.
3. *Chronicling the climate of 2023*. Nature Reviews Earth & Environment, 2024. **5**(4): p. 227-228.
4. Fleck, A., *Cars Cause Biggest Share of Transportation CO₂ Emissions*, in <https://www.statista.com/chart/30890/estimated-share-of-co2-emissions-in-the-transportation-sector/>. 2023, Statista.
5. Nations, U., *Paris Agreement*. 2015, United Nations
6. Subramanian, V., *How automaker decarbonization efforts can reach Paris Agreement targets*. 2023, S&P Global Mobility.
7. IEA, *World Energy Outlook 2023*, IEA, Editor. 2023: Paris.
8. Yun Wang, K.S.C., Jeffrey Mishler, Sung Chan Cho, Xavier Cordobes Adroher, *A review of polymer electrolyte membrane fuel cells: Technology, applications, and needs on fundamental research*. Applied Energy, 2011. **88**: p. 981–1007.
9. Sharaf, O.Z. and M.F. Orhan, *An overview of fuel cell technology: Fundamentals and applications*. Renewable and Sustainable Energy Reviews, 2014. **32**: p. 810-853.
10. Shixiang Xia, R.L., Xin Cui, & Jing Shan, *The application of orthogonal test method in the parameters optimization of PEMFC under steady working condition*. International Journal of Hydrogen Energy, 2016. **41**(26): p. 11380-11390.
11. Omar Z. Sharaf, M.F.O., *An overview of fuel cell technology: Fundamentals and applications*. Renewable and Sustainable Energy Reviews, 2014. **32**: p. 810–853.
12. Song, C., *Fuel processing for low-temperature and high-temperature fuel cells. Challenges, and opportunities for sustainable development in the 21st century*. Catalysis Today, 2002. **77**: p. 17–49.
13. Kocha, S.S., *Polymer Electrolyte Membrane (PEM) Fuel Cells: Automotive Applications*, in *Fuel Cells and Hydrogen Production*. 2019. p. 135-171.

14. Zhan Xu , N.Z., Stuart Hillmansen, Clive Roberts, & Yan Yan, *Techno-Economic Analysis of Hydrogen Storage Technologies for Railway Engineering: A Review*. *Energies*, 2022. **15**(17).
15. Safiye Nur Ozdemir, I.T., Emin Okumus, Fatma Gül Boyacı San, Fehmi Akgün, *Experimental investigation on performance evaluation of PEM electrolysis cell by using a Taguchi method*. *Fuel*, 2023. **344**.
16. Ruirong Chen, Q.L., Xianglong Luo, Yingzong Liang, Jianyong Chen, Zhi Yang, Chao Wang, Ying Chen, *Design and operation optimization of an on-site hydrogen production and purification integration system for PEMFC*. *Fuel*, 2024. **370**.
17. Nur Adiera Hanna Rosli, K.S.L., Wai Yin Wong, Rozan Mohamad Yunus, Tian Khoon Lee, Azizan Ahmad, Seng Tong Chong, *Review of Chitosan-Based Polymers as Proton Exchange Membranes and Roles of Chitosan-Supported Ionic Liquids*. *International Journal of Molecular Sciences*, 2020. **21**(2).
18. Ryan O'Hayre, S.-W.C., Whitney Colella, Fritz B. Prinz, *Fuel Cell Fundamentals*. Third Edition ed. 2016: John Wiley & Sons.
19. EG&G Technical Services, I., *Fuel Cell Handbook*. Seventh Edition ed. 2004. 427.
20. Haile, S.M., *Fuel cell materials and components*. *Acta Materialia* 2003. **51**: p. 5981–6000.
21. S.J. Peighambaroust, S.R., M. Amjadi, *Review of the proton exchange membranes for fuel cell applications*. *International Journal of Hydrogen Energy*, 2010. **35**: p. 9349-9384.
22. Luis Blanco-Cocom 1, S.B.-R., Luis Carlos Ordoñez, & Sergio Iwan Valdez, *A Self-Validating Method via the Unification of Multiple Models for Consistent Parameter Identification in PEM Fuel Cells*. *Energies*, 2022. **15**(3).
23. Jianlu Zhang, H.Z., Jinfeng Wu, & Jiujun Zhang, *Pem Fuel Cell Testing and Diagnosis*. 2013: Elsevier.
24. Ming Fang, J.Z., Cong Yin & Yating Song, *Prediction and parametric analysis of bubble humidifier performance in a polymer electrolyte membrane fuel cell test system by response surface methodology*. *Energy Sources, Part A: Recovery, Utilization, and Environmental Effects*, 2022. **44**(2): p. 3497-3508.

25. Buck, A.L., *New Equations for Computing Vapor Pressure and Enhancement Factor*. Journal of Applied Meteorology, 1981.
26. Buck Research Instruments, L., *Buck Research Manual*. 2010.
27. Jianlu Zhang, H.L., JiuJun Zhang, *Effect of Operating Backpressure on PEM Fuel Cell Performance*. ECS Transactions, 2009. **19**(31): p. 65-76.
28. Jung, A., et al., *An experimental study on the hydrogen crossover in polymer electrolyte membrane fuel cells for various current densities*. Applied Energy, 2016. **175**: p. 212-217.
29. Yuzhen Xia, H.L., Xiaojun Wu, Guilin Hu, Hao Pan, & Baizeng Fang, *Design of New Test System for Proton Exchange Membrane Fuel Cell*. Energies, 2023. **16**(2).
30. Amir Hossein AhmadiTaba, E.A.S.A., *An experimental study on the bubble humidification method of polymer electrolyte membrane fuel cells*. Energy Sources, Part A: Recovery, Utilization, and Environmental Effects, 2018.
31. Bohan Wang, R.L., Dengcheng Liu, Ji Xu, & Bowen Feng, *Investigation of the effect of humidity at both electrode on the performance of PEMFC using orthogonal test method*. International Journal of Hydrogen Energy, 2019. **44**(26): p. 13737-13743.
32. Shen, J., Z. Tu, and S.H. Chan, *Effect of gas purging on the performance of a proton exchange membrane fuel cell with dead-ended anode and cathode*. International Journal of Energy Research, 2021. **45**(10): p. 14813-14823.
33. Dengcheng Liu, S.X., Houwen Tang, Di Zhong, Bohan Wang, Xin Cai, & Rui Lin, *Parameter optimization of PEMFC stack under steady working condition using orthogonal experimental design*. Wiley Energy Research, 2018. **43**(7): p. 2571-2582.
34. Yiming Xu, G.C., Jienan Zhang, Yuyang Li, & Sichuan Xu, *Investigation of Inlet Gas Relative Humidity on Performance Characteristics of PEMFC Operating at Elevated Temperature*. World Electric Vehicle Journal, 2021. **12**(110).
35. Chen, H., et al., *Experimental investigation on PEM fuel cell flooding mitigation under heavy loading condition*. Applied Energy, 2023. **349**.
36. Gong, K., et al., *Experimental investigation on the open cathode air-cooled proton exchange membrane fuel cells: Optimum operating parameters and*

- control strategies*. International Journal of Hydrogen Energy, 2024. **60**: p. 1134-1146.
37. Shao, H., et al., *Modeling and analysis of water droplet dynamics in the dead-ended anode gas channel for proton exchange membrane fuel cells*. Renewable Energy, 2019. **138**: p. 842-851.
38. Jian, Q., et al., *Experimental study on the purge process of a proton exchange membrane fuel cell stack with a dead-end anode*. Applied Thermal Engineering, 2018. **142**: p. 203-214.
39. Kahveci, E.E. and I. Taymaz, *Hydrogen PEMFC stack performance analysis through experimental study of operating parameters by using response surface methodology (RSM)*. International Journal of Hydrogen Energy, 2022. **47**(24): p. 12293-12303.
40. Yang, Y., et al., *Overall and local effects of operating parameters on water management and performance of open-cathode PEM fuel cells*. Applied Energy, 2022. **315**.
41. Yao, J., et al., *High-stability dead-end anode proton exchange membrane fuel cells by purge optimization*. Journal of Power Sources, 2024. **595**.
42. Mengist, W., T. Soromessa, and G. Legese, *Method for conducting systematic literature review and meta-analysis for environmental science research*. MethodsX, 2020. **7**: p. 100777.
43. Le, P.T., et al., *Taxonomy of risks in PPP transportation projects: a systematic literature review*. International Journal of Construction Management, 2019. **22**(2): p. 166-181.
44. Wasterlain, S., et al., *Study of temperature, air dew point temperature and reactant flow effects on proton exchange membrane fuel cell performances using electrochemical spectroscopy and voltammetry techniques*. Journal of Power Sources, 2010. **195**(4): p. 984-993.
45. Costa, S., et al., *Design of experiments, a powerful tool for method development in forensic toxicology: application to the optimization of urinary morphine 3-glucuronide acid hydrolysis*. Analytical and Bioanalytical Chemistry, 2010. **396**(7): p. 2533-2542.

46. B. H. WANG, Y.J., and Y. G. LUO, *PARAMETRIC OPTIMIZATION OF EQ6110HEV HYBRID ELECTRIC BUS BASED ON ORTHOGONAL EXPERIMENT DESIGN*. International Journal of Automotive Technology, 2010. **11**(1): p. 119–125.
47. Tian, P., et al., *The Research of Test Case Generation and Its Optimization Methods Based on Orthogonal Test Method and Greedy Algorithm*, in *2009 International Conference on Intelligent Human-Machine Systems and Cybernetics*. 2009. p. 474-477.
48. Yuan, W., et al., *Dominance evaluation of structural factors in a passive air-breathing direct methanol fuel cell based on orthogonal array analysis*. Applied Energy, 2011. **88**(5): p. 1671-1680.
49. Junjie Zhao, Z.T., & Siew Hwa Chan, *In-situ measurement of humidity distribution and its effect on the performance of a proton exchange membrane fuel cell*. Energy, 2022. **239**.
50. Liu, R., et al., *Performance optimization of ultra-low platinum loading membrane electrode assembly prepared by electrostatic spraying*. International Journal of Hydrogen Energy, 2021. **46**(17): p. 10457-10467.
51. Boni, M., C.S. Manikanta, and V. Velisala, *Experimental evaluation of proton exchange membrane fuel cell performance with sinusoidal flow channel designs*. International Journal of Hydrogen Energy, 2024. **53**: p. 1233-1241.
52. Zhu, X., et al., *Effects of operating conditions on the performance uniformity of the proton-exchange membrane fuel cell stack*. Energy Conversion and Management, 2023. **281**.
53. Kim, H., et al., *Mass diffusion characteristics on performance of polymer electrolyte membrane fuel cells with serpentine channels of different width*. International Journal of Heat and Mass Transfer, 2022. **183**.
54. *Economical Temperature Controller C-MTCTRST Instruction Manual*, MiSUMi, Editor.
55. Inc, F.C.T., *HUMIDITY BOTTLES*.
56. *OPERATING MANUAL Aalborg® DPC Precision Digital Mass Flow Controllers*, A.I. Controls, Editor. 2018.
57. *Integral Bonnet Needle Valves NV & SV Series* H.-L. Corporation, Editor. 2017.
58. *Instruction Manual Compact Pressure Sensor*, S. Corporation, Editor.

59. AirTAC, *PRODUCTS CATALOG*. 2023.
60. ELECTRONICS, I., *IT8800 High Power DC Electronic Load*.
61. GAO Xiangsheng, Z.Y., ZHANG Hongwei, & WU Qiong, *Effects of Machine Tool Configuration on Its Dynamics Based on Orthogonal Experiment Method*. Chinese Journal of Aeronautics, 2012. **25**(2): p. 285-291.
62. Jinyong Peng, F.D., Qiwei Xu, Youwei Xu, Yan Qi, Xu Han, Lina Xu, Guorong Fan, Kexin Liu *Orthogonal test design for optimization of supercritical fluid extraction of daphnoretin, 7-methoxy-daphnoretin and 1,5-diphenyl-1-pentanone from Stelleria chamaejasme L. and subsequent isolation by high-speed counter-current chromatography*. Journal of Chromatography A, 2006. **1135**(2): p. 151-157.
63. Niu, T., et al., *Purge strategy analysis of proton exchange membrane fuel cells based on experiments and comprehensive evaluation method*. Fuel, 2024. **363**.
64. P D Thao, V.T.C., N H Khan, S Mek, S Hirai, and L Visarn, *Study of Variable Operating Parameters Effect on PEMFC Performance*, in *The 13th TSME International Conference on Mechanical Engineering*. 2023, Department of Mechanical Engineering, Faculty of Engineering, Chiang Mai University: Chiang Mai, Thailand. p. 151-161.
65. Young Sang Kim, D.K.K., Kook Young Ahn, & Min Soo Kim*, *Parametric study on the local current distribution of polymer electrolyte membrane fuel cell with counter flow channel under pressurized condition*. Journal of Mechanical Science and Technology 2020. **34**(5): p. 2189-2198.
66. Prem Kumar Thiyagarajan, K.J., & Manoj Kumar P, *Combination studies of operating cell, inlet-line, and humidification temperatures on performance of proton exchange membrane fuel cell*. Fuel Cells, 2022. **22**(3): p. 71-84.
67. Tien-Fu Yang, B.-H.S., Mohammad Ghalambaz, Wei-Mon Yan, *Effects of operating parameters and load mode on dynamic cell performance of proton exchange membrane fuel cell*. International Journal of Energy Research, 2020. **45**(2): p. 2474-2487.
68. Kui Jiao, J.X., Qing Du, Zhiming Bao, Biao Xie, Bowen Wang, Yan Zhao, Linhao Fan, Huizhi Wang, Zhongjun Hou, Sen Huo, Nigel P. Brandon, Yan Yin, and

Michael D. Guiver, *Designing the next generation of proton-exchange membrane fuel cells*. *Nature*, 2021. **595**(7867): p. 361-369.

69. Dashti, I., et al., *Optimization of the performance, operation conditions and purge rate for a dead-ended anode proton exchange membrane fuel cell using an analytical model*. *Energy*, 2019. **179**: p. 173-185.



Appendix A

CALIBRATION CERTIFICATES

A-1. Hydrogen mass flow controller

CALIBRATION CERTIFICATE

Calibration No.: 200729533273-1_000.dat

Page 1 of 1 This report shall not be reproduced except in full, without the written approval of the laboratory.

Customer : A.M.H. (THAILAND) CO., LTD.	NONTHABURI, THAILAND
Customer Po : PO2007102	Calibration Date : Jul 29 2020

DEVICE UNDER TEST-DUT: New	TEST CONFIGURATION : As Left	
DUT Model : DPC17	Calibration Fluid : Hydrogen	
DUT Serial Number : 533273-1	Calibration Pressure/ Temp.: 101.3 kPa_abs 21.1 C	
Flow Sensor : Thermal	Correlation Factor (if applies) : N/A	
Flow Sensor Serial Number : N/A	Reference Standard :	Calibrator
Flow Range : 0.0 to 500.0 sccm@70.0F*	Manufacturer :	Fluke 2056
Output Range : 4.000 to 20.000 mA	Model Number :	molbox1/ A700
DUT Tolerance : 0.2 %Span + 0.5 %Rdg	Serial Number :	2056
Operating Fluid : Hydrogen	Calibration due Date :	Mar 12 2021
Operating Pressure : 14.69 psi_abs	Tolerance :	0.2 %Rdg
Operating Temperature : 70.0 F	DUT Set Point (if applies) / Test :	4-20 mA DIRMAN5dig_3
Flow Attitude : Horizontal	Notes :	RS232

Calibration Lab Ambient Conditions: Pressure: 14.68 psi_abs, Temperature: 73.2 F, Relative Humidity does not exceed 70%.

This DUT is calibrated against Manufacturing Procedures according to Quality System Manual 04-001 rev. 10, which conforms to ISO9001-2015 and ANSI/ISO17025. Calibration is performed by passing calibrated flow through the calibrated DUT. The Reference Standards used in the calibration are traceable to NIST. The collective uncertainty of Reference Standards used in this calibration does not exceed 25% of the DUT accuracy.

NOTE: Calibration results relate only to the calibrated DUT and to conditions at the time of this test. Calibration lab does not provide the specific calibration due date unless requested by the customer however it is recommended by manufacturer to re-calibrate the DUT no later than after 6 months of frequent operation.

DUT Flow*	DUT Output	Reference Flow*	Deviation*	+/-Deviation Limits*	Status
0.057 sccm@70.0F	4.002 mA	0.044 sccm@70.0F	0.013	1.000	Pass
500.036 sccm@70.0F	20.001 mA	499.633 sccm@70.0F	0.403	3.500	Pass
400.025 sccm@70.0F	16.801 mA	400.128 sccm@70.0F	-0.103	3.000	Pass
299.975 sccm@70.0F	13.599 mA	300.545 sccm@70.0F	-0.570	2.500	Pass
199.979 sccm@70.0F	10.399 mA	200.611 sccm@70.0F	-0.632	2.000	Pass
100.007 sccm@70.0F	7.200 mA	100.452 sccm@70.0F	-0.445	1.500	Pass

Minor Adjustment
Test result: Pass

%FS Error vs. DUT Flow
(Fit Order: 1)

Technician: D.Tzop Approved by: 1279 Cal Due Date: (SEE NOTE)

* Customer Flow Units are represented by primary SI Flow Units, which are consistent with the International System of Units - CGPM, Sevres 1960. See the NIST publication no. 811 - 1995 edition. (Typically mL/min=ccm@70F)

AALBORG INSTRUMENTS AND CONTROLS, INC.
 20 Corporate Drive, Orangeburg, New York 10962 USA
 http://www.aalborg.com, Phone: +1 (845) 770-3000, toll-free (US/CAN) (800) 866-3837, Fax: +1 (845) 770-3010
 Issue Date: 29 Jul 2020

This material is reserved for educational use only, not allowed for commercial use.

Forbidden to modify the content, and cite the document when use.

A-2. Air massflow controller

CALIBRATION CERTIFICATE

Calibration No.: 200729533274-1_000.dat

Page 1 of 1 This report shall not be reproduced except in full, without the written approval of the laboratory.

Customer : A.M.H. (THAILAND) CO., LTD.	NONTHABURI, THAILAND
Customer Po : PO2007102	Calibration Date : Jul 29 2020

DEVICE UNDER TEST-DUT: New	TEST CONFIGURATION : As Left		
DUT Model : DPC 17	Calibration Fluid : Air	Calibration Pressure/ Temp.: 101.3 kPa_abs 21.1 C	
DUT Serial Number : 533274-1	Correlation Factor (if applies) : N/A		
Flow Sensor : Thermal	Reference Standard :	Calibrator	Multimeter
Flow Sensor Serial Number : N/A	Manufacturer :	DH Instruments	Fluke
Flow Range : 0.0 to 2.0 slm@70.0F *	Model Number :	molbox1+/ A700	8809a
Output Range : 4.000 to 20.000 mA	Serial Number :	1070	1271006
DUT Tolerance : 0.2 %FS + 0.5 %Rdg	Calibration due Date :	Mar 12 2021	APRIL 8, 2022
Operating Fluid : AIR	Tolerance :	0.2 %Rdg	0.065%Range
Operating Pressure : 14.69 psi_abs.	DUT Set Point (if applies) / Test :	4-20 mA	DIRMAN5dig_4
Operating Temperature : 70.0 F	Notes :	RS232	
Flow Attitude : Horizontal	Calibration Lab Ambient Conditions: Pressure 14.65 psi_abs., Temperature 73.1 F, Relative Humidity does not exceed 70%.		

This DUT is calibrated against Manufacturing Procedures according to Quality System Manual 04-001 rev. 10, which conforms to ISO9001-2015 and ANSI/ISO17025. Calibration is performed by passing calibrated flow through the calibrated DUT. The Reference Standards used in the calibration are traceable to NIST. The collective uncertainty of Reference Standards used in this calibration does not exceed 25% of the DUT accuracy.

NOTE: Calibration results relate only to the calibrated DUT and to conditions at the time of this test. Calibration lab does not provide the specific calibration due date unless requested by the customer however it is recommended by manufacturer to re-calibrate the DUT no later than after 6 months of frequent operation.

DUT Flow*	DUT Output	Reference Flow*	Deviation*	+/-Deviation Limits*	Status
0.000 slm@70.0F	4.000 mA	0.002 slm@70.0F	-0.002	0.004	Pass
2.000 slm@70.0F	20.000 mA	2.001 slm@70.0F	-0.001	0.014	Pass
1.800 slm@70.0F	16.800 mA	1.800 slm@70.0F	0.000	0.012	Pass
1.200 slm@70.0F	13.600 mA	1.200 slm@70.0F	0.000	0.010	Pass
0.800 slm@70.0F	10.400 mA	0.800 slm@70.0F	0.000	0.008	Pass
0.400 slm@70.0F	7.200 mA	0.400 slm@70.0F	0.000	0.006	Pass

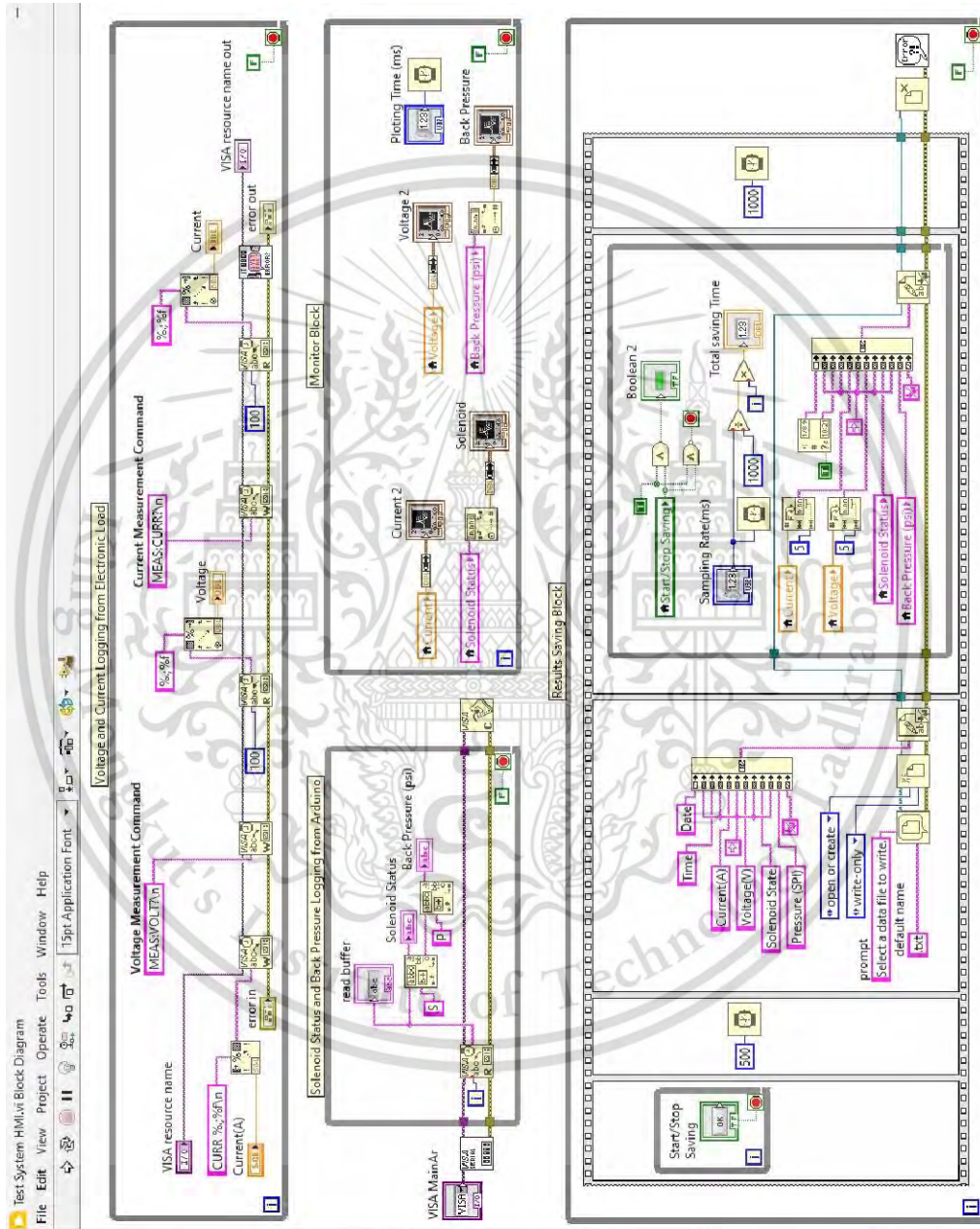
Minor Adjustment
Test result: Pass

Technician: D.Trzop Approved by: [Signature] Cal Due Date: (SEE NOTE)

* Customer Flow Units are represented by primary SI Flow Units, which are consistent with the International System of Units - CGPM, Sevres 1960. See the NIST publication no. 811 - 1995 edition. (Typically smL/min=ccm@70F)

AALBORG INSTRUMENTS AND CONTROLS, INC.
 20 Corporate Drive, Orangeburg, New York 10962 USA
 http://www.aalborg.com, Phone: +1 (845) 770-3000, toll-free (US/CAN) (800) 866-3837, Fax: +1 (845) 770-3010
 Issue Date: 29 Jul 2020

Appendix B HMI LABVIEW BLOCK DIAGRAM



Appendix C

ARDUINO CODES

C-1. Pressure sensor calibration

```
int sensorPin = A1;
int sensorValue = 0;
const float OffSet = 1;
unsigned long previousMillis = 0;
const long interval = 60000; // 1 minute in milliseconds
int readingsCount = 0;
long totalSensorValue = 0;

void setup()
{
  Serial.begin(9600);
}

void loop()
{
  unsigned long currentMillis = millis();
  if (currentMillis - previousMillis >= interval)
  {
    // Calculate and print the average
    float averagePressure = totalSensorValue / (float)readingsCount;
    Serial.print("Average Pressure xxxxxxxx: ");
    Serial.println(averagePressure);
    // Reset variables for the next interval
    previousMillis = currentMillis;
    readingsCount = 0;
    totalSensorValue = 0;
  }
  // Read sensor value
  sensorValue = analogRead(sensorPin);
  float pressure = (sensorValue * (5.0 / 1023.0) - OffSet) * 14.5037738
/ 0.4; // Calculate pressure
  // Accumulate readings for average calculation
  totalSensorValue += sensorValue;
  readingsCount++;
  // Print individual sensor reading
  Serial.print("Read ");
  Serial.println(sensorValue);

  delay(100); // Delay between individual readings
}
```

This material is reserved for educational use only, not allowed for commercial use.

Forbidden to modify the content, and cite the document when use.

C-2. Purge valve control

```
const int solenoidPin = 10;
unsigned long previousMillis = 0;
const long intervalOn = 30000; // Adjust Purge Interval (ms)
const long intervalOff = 750; // Adjust Purge duration (ms)
boolean solenoidState = false;

void setup()
{
  Serial.begin(9600);
  pinMode(solenoidPin, OUTPUT);
}

void loop()
{
  unsigned long currentMillis = millis();
  if (solenoidState == false)
  {
    if (currentMillis - previousMillis >= intervalOff)
    {
      previousMillis = currentMillis;
      Serial.print("1S");
    }
  }
  else
  {
    if (currentMillis - previousMillis >= intervalOn)
    {
      solenoidState = false;
      previousMillis = currentMillis;
    }
    Serial.print("0S");
  }
  digitalWrite(solenoidPin, solenoidState);
}
```

This material is reserved for educational use only, not allowed for commercial use.

Forbidden to modify the content, and cite the document when use.

C-3. Solenoid status and back pressure logging

```
const int SolenoidPin = 6;

void setup()
{
  Serial.begin(9600);
  pinMode(SolenoidPin, INPUT);
}

void loop()
{
  if (digitalRead(SolenoidPin) == HIGH)
  {
    Serial.print("1S");
  }
  else
  {
    Serial.print("0S");
  }
  float sensorValue = analogRead(A0);
  float pressure = (sensorValue - 195.31)*14.5037738/80.052;
  Serial.print(pressure,5);
  Serial.println("P");
}
```

This material is reserved for educational use only, not allowed for commercial use.

Forbidden to modify the content, and cite the document when use.

Appendix D

CONFERENCE PARTICIPATION

The 13th TSME International Conference on Mechanical Engineering
12th – 15th December 2023
Chiang Mai, Thailand



AME0005

Study of Variable Operating Parameters Effect on PEMFC Performance

P D Thao¹, V T Chau², N H Khan¹, S Mek¹, S Hirai³, and L Visarn^{4,*}

¹Department of Mechanical Engineering, School of Engineering, King Mongkut's Institute of Technology Ladkrabang, 1 Chalong Krung 1 Alley, Lat Krabang, Khet Lat Krabang, Krung Thep Maha Nakhon 10520, Thailand

²Faculty of Automotive Engineering Technology, Industrial University of Ho Chi Minh City, Go Vap District, Ho Chi Minh City, 727900, Vietnam

³School of Engineering, Tokyo Institute of Technology, Meguro City, Tokyo, 152-8550, Japan

⁴National Energy Technology Center (BNETC), National Science and Technology Development Agency, Pathum Thani, Bangkok, 12120, Thailand

* Corresponding Author: visarn.lil@entec.or.th

Abstract. The Proton Exchange Membrane Fuel Cell (PEMFC) is considered as the main fuel cell candidate technology for light-duty and heavy-duty transportation applications with high power densities generating. Studies in improving PEMFC performance help reduce the powertrain size and weight of fuel cell electric vehicles (FCEVs). Relative humidity (RH) and operating temperature (OT) are the key operating parameters contributing to PEMFC characteristics. In this study, the effects of RH and OT on the PEMFC performance were investigated by varying RH from 50% to 70% and OT from 60°C to 80°C. The experiments were conducted on a single PEMFC cell with an active area of 25 cm². Polarization curves and power graphs were used to study the effects of OT and RH on PEMFC performance. The impacts of OT and RH were examined based on the range analysis method. The experiment results show that, the OT has more influence on PEMFC performance than RH. Besides that, individual effects of OT and RH changed when taking both parameters into study the combined effects. Furthermore, the group of appropriate combined operating parameters of the fuel cell was defined to maximize the PEMFC performance.

Keywords: PEMFC, Performance, Temperature, Humidity.

1. Introduction

The soaring reliance on fossil fuels for the automotive industry and their environmental impacts have attracted researchers to explore alternative solutions for internal combustion engine vehicles (ICEVs). Fuel cell electric vehicles and battery electric vehicles (BEVs) are the main candidates to be successors [1]. Among them, FCEVs provide a longer range, shorter refueling time within two minutes, better tolerance of cold weather, and lighter weight compared to BEVs in light-duty transportation applications [2]. The PEMFC is usually used for FCVEs due to its wide range of power density (1×10³~250 kW), high efficiency at the energy conversion and its friendly user operating conditions [1-3]. In comparison

AUTHOR BIOGRAPHY

Name Mr. Pham Dinh Thao
Date of Birth August 16, 2000, in Viet Nam
Address: 9/16 Moo 17, Phahonyothin road, Khlong Nueng, Khlong Luang,
Pathum Thani 12120.

Educational Background:

2024: Master of Engineering in Automotive and Advanced
Transportation Engineering
School of Engineering, King Mongkut's Institute of Technology
Ladkrabang, Thailand
2022: Bachelor of Engineering in Automotive Engineering Technology
Faculty of Automotive Engineering Technology, Industrial
University of Ho Chi Minh City, Vietnam

Conference Participation Publications:

- [1] P D Thao, V T Chau, N H Khan, S Mek, S Hirai, and L Visarn, Study of Variable Operating Parameters Effect on PEMFC Performance, in The 13th TSME International Conference on Mechanical Engineering. 2023, Department of Mechanical Engineering, Faculty of Engineering, Chiang Mai University: Chiang Mai, Thailand. p. 151-161.
- [2] K H Nguyen, M Masomtob, B Kerdsup, S Karukanan, P Champa, T D Pham, S Hirai, C T Vo, P Kumool, and C Charoenphonphanich. Efficiency evaluation on cooling behavior of water-cooling jacket for synchronous reluctance motor. Journal of Research and Application in Mechanical Engineering (2024) Vol. 12, No. 1.